Model for the RE-TC thalamic circuit with application to childhood absence epilepsy

by

Jennie Newman

A thesis
presented to the University of Waterloo
in fulfillment of the
thesis requirement for the degree of
Master of Mathematics
in
Applied Mathematics

Waterloo, Ontario, Canada, 2019

© Jennie Newman 2019

I hereby declare that I am the sole author of this thesis. This is a true copy of the thesis, including any required final revisions, as accepted by my examiners.

I understand that my thesis may be made electronically available to the public.

Abstract

Childhood absence epilepsy (CAE) is an idiopathic neurological disorder affecting roughly 2-8 children per 100,000 children worldwide. It is characterized by absence seizures, or short lapses in consciousness, and the appearance of slow wave discharge (SWD) patterns on an electroencephalogram (EEG). With the cause of onset and recovery still unknown, much research has been conducted in order to determine the set of genes responsible for this disorder. Experimental animal models and mathematical models of neural networks have so far suggested the thalamocortical network as the site of seizure initiation, and the *CACNA1H* gene as a promoter of SWD patterns in the brain. In this thesis, we develop a mathematical model of part of the thalamocortical network, comprised of thalamic reticular (RE) and thalamocortical (TC) neurons. We then use this model to study the effects of previously suggested CAE factors, such as the *CACNA1H* gene mutation, $GABA_A$ synapse conductance and T-type Ca^{2+} channel conductance, on the formation of SWD patterns in the network. We find a link between a decreased $GABA_A$ conductance and increased SWD activity in our network, as well as the dependence of SWD activity on the interactions between the multiple factors of our study. Our results imply that CAE and SWD activity may have a multifactorial cause, and that the thalamus may not be solely responsible for the generation and propagation of SWDs in the thalamocortical network.

Acknowledgements

I would first like to thank my wonderful supervisor, Dr. Sue Ann Campbell, for everything she has done for me these past two years. From all of her time, explanations, advice, guidance and inspiration she's given me, I couldn't have had a better experience here at Waterloo.

I would also like to thank my committee members, again Dr. Sue Ann Campbell, Dr. Brian Ingalls and Dr. Marek Stastna. Your time and help with this thesis is greatly appreciated.

To my family, thank you for all of your support and encouragement throughout my life, and especially throughout these past two years. I wouldn't have been able to make it this far without each of you.

And to Kai, thank you for always being there for me, and for listening to all my ramblings and ideas throughout the development of this thesis.

Dedication

This thesis is dedicated to my lovely family; Cheryl, Pat, Sarah, Joy and my dearest Gracie.

Table of Contents

List of Tables

List of Figures

Chapter 1

Introduction

Childhood absence epilepsy (CAE) is a neurological condition affecting roughly 2-8 children per 100,000 children, worldwide. It is characterized by absence seizures, or short lapses in consciousness, and the appearance of slow wave discharge (SWD) patterns on an electroencephalogram (EEG). CAE typically appears in individuals around the ages of 3 to 8 years old, and has a spontaneous recovery rate of about 70% [13]. With the cause of onset and recovery still unknown, much research has been conducted in order to determine the set of genes responsible for this disorder. Experimental animal models and mathematical models of neural networks have so far suggested a particular subnetwork of the brain, called the thalamocortical network, as the site of seizure initiation [67], and the *CACNA1H* gene as a promoter of SWD patterns in the brain [13]. Here, we aim to develop a basic mathematical model of part of the thalamocortical network, based on Destexhe's 1994 [22] and 1996 models [21], and consider the effects of suggested CAE factors, such as the *CACNA1H* gene defect, $GABA_A$ synapse conductance, and T-Type Ca^{2+} channel conductance, on the model.

1.1 Outline of Thesis

In Chapter 2 we look at the biological background necessary to study childhood absence epilepsy and mathematical models of neural networks. This starts with a review of the basic structure and electrophysiology of neurons, and then moves into the roles of various neurons and regions of the brain. From there, we review general information on epilepsies, and then discuss childhood absence epilepsy in more detail. We focus on the slow wave

discharges that characterize the disorder, as well as the causes and genes of the disorder, and the GAERS model that is often used to study it. In Chapter 3 we focus on the mathematical modelling used to study childhood absence epilepsy. We discuss how the electrical component of neurons is used to develop mathematical models, with a focus on the well-known Hodgkin-Huxley model. We also give a literature review for three papers related to modelling genetic defects in absence epilepsies, and describe two modelling programs specifically used for biological systems. Chapter 4 looks at the development of the RE and TC models, first as individual cell models and then as a paired network. We discuss the currents and synapses involved, as well as perform tests to ensure our modelled cells demonstrate the typical behaviour of real cells. In Chapter 5 we test for the effects of the *CACNA1H* gene mutation, $GABA_A$ synapse and T-type Ca^{2+} channel conductance on slow wave discharge formation in our network model. Chapter 6 summarizes the results of this thesis, and discusses its limitations and directions for future work.

Chapter 2

Biological Background

At the base of all human neurological disorders is the activity between the billions of neurons in the brain [36]. How these neurons interact with each other shapes how we act as humans, and it is the intricacy of the neural components that impacts the brain as a whole. Here, we review the basic cellular architecture and general information regarding neurons and the brain, and then discuss the biology of different types of epilepsy, focusing on childhood absence epilepsy.

2.1 Neurons

Neurons are a type of eukaryotic cell, and so contain a specific set of cellular structures. Like other eukaryotic cells, a neuron contains a cellular membrane, comprised of hydrophobic fatty molecules, which separates the cell's interior components from its surrounding environment. Situated within this membrane are embedded proteins, which are responsible for a number of cellular activities such as transporting molecules into and out of the cell, and transmitting signals to and from nearby cells. Within the cell are a number of internal structures called organelles, which each perform various cellular functions. As typically the largest of these organelles, the nucleus holds most of the cellular DNA.

At the next level of neuron architecture are the four basic regions that make up the neuron, which include the cell body, the dendrites, the axon and the axon terminals. The cell body is the control centre of the neuron, as it contains the nucleus and is the location of synthesis for the majority of the proteins in the cell. The dendrites, which protrude

from the cell body, are responsible for receiving chemical signals from surrounding neurons and then converting them into electrical impulses which are carried into the cell. These electrical impulses, if large enough, can create an action potential, or a sudden change in voltage caused by ions moving across the cell membrane. These impulses would then be carried down the axon towards the axon terminals [57, Chapter 21]. The axon, tube-like in shape, can range in length from a few millimetres to more than a metre in humans [72, Chapter 1], and can transport an action potential through to the terminals in just a few milliseconds [57, Chapter 21]. It is the axon terminals at the end of the axon that form the connections, or synapses, with other cells, allowing for signalling to and from neighbouring cells [57, Chapter 21]. Figure 2.1 shows an illustration of a neuron.

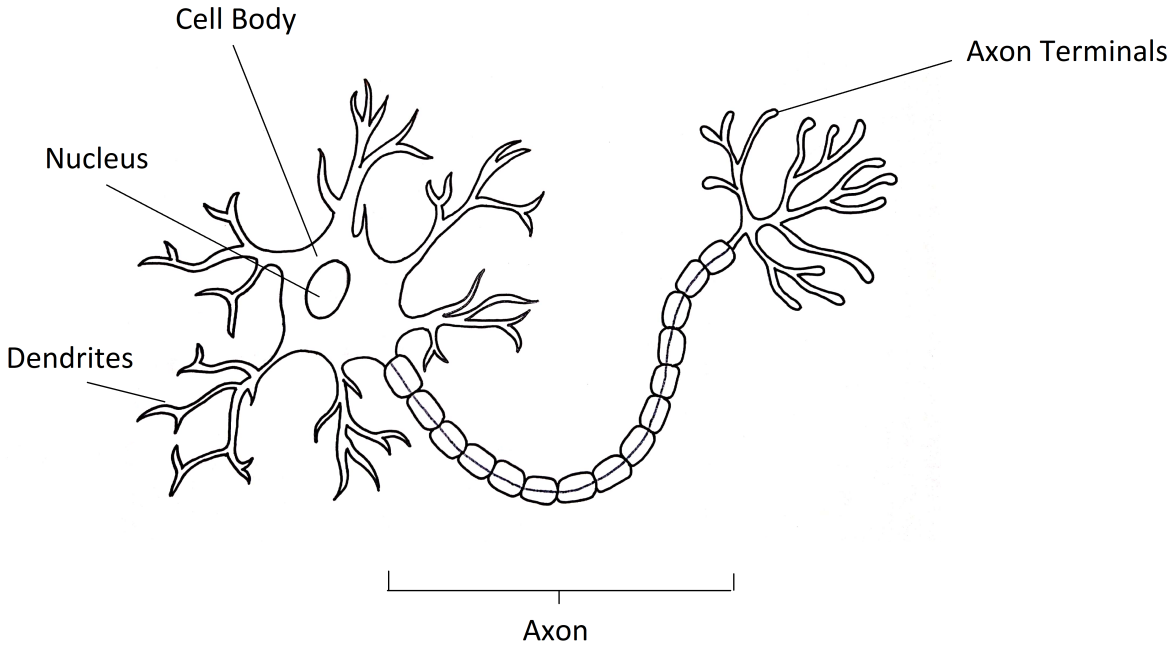

Figure 2.1: Illustration of a neuron.

As mentioned, action potentials, also known as spikes, are the mechanism by which neurons transmit signals from one neighbouring cell to another, and as such, they are a fundamental aspect of neurons. They rely on the electrical activity in neurons, which itself is dependent on the opening and closing of ion channels, the membrane-embedded transport proteins, within the cell. Specifically, it is the successive opening and closing of sodium (Na^+) and then potassium (K^+) channels that generate and propagate an action

potential down the axon of a neuron [57, Chapter 21].

Much of our research here relies on the generation of action potentials and tracking the change in voltage across the cell. Before discussing the electrophysiology of action potentials, we first look at the basics mechanisms behind the phenomenon; ion channels and synapses.

2.1.1 Channels

Within and around the cell are a variety of ions, primarily sodium (Na^+), potassium (K^+) and chloride (Cl^-). The dynamic difference in ion concentration between the inside and the outside of the cell is referred to as the concentration gradient, which causes the ions to flow from an area of high concentration to an area of low concentration. As the ions are charged, either positively or negatively, there is an additional force which affects the movement of the ions. When both of these factors are balanced, an equilibrium is achieved. The ion channels within the cell membrane allow for this equilibrium to be reached, as they allow for the various ions to enter and exit the cell [33, Chapter 1].

In terms of their basic properties, ion channels can come in two forms; gated and nongated. Nongated channels are never closed and allow ions to pass through them freely, whereas gated channels typically only allow one type of ion to move through and can open and close by different means [33, Chapter 1]. Voltage-gated channels are responsible for action potential dynamics, and are activated by the voltage of the membrane. Ligand-gated and signal-gated channels, on the other hand, respond to molecular signals that bind to the channel proteins, and are often involved in the transmission of signals between cells [57, Chapter 21].

For the voltage-dependent gates, typically there are activation and inactivation gates which open and close at different rates and in different scenarios. For example, in the fast Na^+ channel, at resting membrane potential the activation gate is closed and the inactivation gate is open. When the cell becomes depolarized enough, the activation gate opens, and when the cell becomes more depolarized, the inactivation gate closes. This is an important aspect of generating action potentials, as when both gates are open due to the first depolarization, Na^+ ions flow into the cell, and when the cell becomes more depolarized, the inactivation gate closes and the channel no longer allows Na^+ ions to flow through it. However, not all channels have two gates. The delayed rectifier K^+ channel only has one gate for activation, for example.

Oftentimes it is the particular ion that is allowed to pass through that classifies the channel. And, as the flow of ions is referred to as a current, many of these channels cor-

respond to different currents, which each affect the cell in a different way. For example, the specific K^+ and Na^+ ion channels that are responsible for action potential dynamics, correspond to the fast transient sodium current and the delayed rectifier potassium current. Many types of channels and related currents exist, with a few other examples being the potassium leak current, the low-threshold calcium current and the calcium-dependent potassium current [33, Chapter 1]. Each of these currents, and more, will be described in Chapter 4, where we detail the currents included in our mathematical models.

2.1.2 Synapses

Synaptic dynamics are what allows individual neurons to communicate and connect with neighbouring cells. The basic idea is that chemical signals are passed through the synapse, or space, between two neurons from a presynaptic cell to a postsynaptic cell, which then elicits a response in the receiving cell. These dynamics rely on a number of intracellular factors, and can generate very different responses in a cell depending on these factors.

Specifically, the process of signal transmission starts when an action potential travels through a neuron and reaches the terminating regions of the axon called the synaptic terminals. Within these regions are calcium channels, which release calcium as they become depolarized from the action potential. Specific calcium binding proteins are then activated by this release of calcium, and then bind to vesicles containing molecules called neurotransmitters. This binding enables the vesicles to release the neurotransmitters into the synaptic cleft. Once released, the transmitter, or chemical signals, travels through the synapse between the cells and binds to receptors on the receiving cell. This binding then opens channels in the postsynaptic cell. Depending on the specific transmitter that is sent, it can elicit an excitatory (promoting action potential formation) or inhibitory (impeding action potential formation) response in the postsynaptic cell [33, Chapter 7].

Of course, this is only a generalized description of the synaptic dynamics. The dynamics of this process can become more intricate. For example, presynaptic stimulation can lead to more vesicles of transmitter occurring at synaptic terminals, which can cause more transmitter release on successive presynaptic spikes. This event is called facilitation, or potentiation. In a similar way, if a presynaptic neuron has had multiple spikes, it can lead to a decrease in the amount of transmitter released on successive spikes, which may require time to recover from. This event is called depression. As such, it is difficult to accurately predict how much transmitter is released and received by the postsynaptic neuron in each spike [33, Chapter 7].

In terms of specific transmitters that are sent between neurons, two of the main trans-

mitters are glutamate and gamma-aminobutyric acid (GABA). Glutamate transmitters activate AMPA/kainate receptors and NMDA receptors, which lead to excitation in postsynaptic cells. In particular, the AMPA/kainate receptors are very fast and can show strong depression, whereas the NMDA receptors are associated with long-term potentiation of synapses. The GABA transmitters are the principal inhibitory neurotransmitter in the cortex, and these activate $\mathrm{GABA_A}$ and $\mathrm{GABA_B}$ receptors in postsynaptic cells. $\mathrm{GABA_A}$ synapses are associated with fast inhibition, whereas $\mathrm{GABA_B}$ synapses have responses that are often slow to activate and long-lasting. This is due to the indirect binding of transmitter to the $\mathrm{GABA_B}$ receptors. In this case, the transmitter instead binds to a receptor protein, which then activates an intracellular protein complex called a G-protein. This G-protein then activates a potassium channel, which hyperpolarizes the postsynaptic cell [33, Chapter 7].

The AMPA/kainate, NMDA, $\mathrm{GABA_A}$ and $\mathrm{GABA_B}$ synapses represent different types of chemical connections between neurons, however non-chemical connections exist as well. These are called gap, or electrical, junctions. These junctions differ from the chemical synapses in that they don't require an action potential in order to communicate with other cells. Regardless of the cells' behaviour, the gap junctions keep the cells in direct communication with other neurons [33, Chapter 7].

In order to represent these synaptic dynamics, kinetic activation schemes are often used. The AMPA/kainate, NMDA and $\mathrm{GABA_A}$ synaptic dynamics can be represented as the following first-order activation scheme,

$$C + T \underset{\beta}{\overset{\alpha}{\rightleftharpoons}} O \tag{2.1}$$

Here, C and O represent the closed and open states of the channel, T represents the transmitter that binds to the channel receptors, and α and β are the forward and backward rate constants.

The $\mathrm{GABA_B}$ dynamics can be represented by the following kinetic scheme,

$$R_0 + T \rightleftharpoons R \tag{2.2}$$

$$R + G_0 \rightleftharpoons RG \rightarrow R + G \tag{2.3}$$

$$G \rightarrow G_0 \tag{2.4}$$

$$C + 4G \rightleftharpoons O \tag{2.5}$$

Again, the process described here refers to the transmitter (T) binding to the receptor (R_0) and then activating it (R). The G-protein is catalyzed by R to transition from its inactive form (G_0) to its activated form (G). From here, G binds to and opens the potassium channel on four independent binding sites [21].

2.1.3 Electrophysiology

Having discussed the basic physiological features of neurons, we now look at the basic electrophysiological properties. To start, every neuron has a voltage associated with it, which is due to the imbalance of charge between the inside and the outside of the cell. The difference in voltage between the inside and the outside of the cell is referred to as the membrane potential. When the neuron is at rest, that is, the ions in and around the cell are at an equilibrium, the resulting membrane potential is referred to as the resting potential, which typically has a value of around $-70\,\mathrm{mV}$ in most neurons [33, Chapter 1].

There are many factors that affect a neuron's membrane potential, with the main one being the outward and inward currents to the cell. When a positive ion leaves the neuron, or a negative ion enters the cell, this creates an outward current, which causes the membrane potential to become more negative, hyperpolarizing the cell. In a similar way, a negative ion leaving the cell or a positive ion entering the cell creates an inward current which raises the membrane potential, depolarizing the cell [33, Chapter 1].

The electrical activity behind action potentials is caused by the opening and closing of certain sodium and potassium channels within the cell membrane. Specifically, when the neuron is at rest, most Na^+ channels are closed, meaning the membrane potential is mostly determined by the concentration of K^+ ions. When the neuron is stimulated in a way that depolarizes the cell, raising the membrane potential above some threshold, called the activation threshold, it opens the Na^+ channels. This allows an influx of Na^+ ions into the cell. This influx of positive ions depolarizes the cell further, causing more Na^+ channels to open, and therefore more Na^+ ions to enter the cell, and the process continues [33, Chapter 1].

As the Na^+ channels are transient and remain open for only a short time, they eventually close, stopping the influx of Na^+ ions into the cell. The depolarization of the cell, however, also causes K^+ channels to open, allowing K^+ ions to exit the cell. Once the Na^+ channels close, the efflux of K^+ ions hyperpolarizes the cell and lowers its membrane potential past the resting potential. When the K^+ channels finally close, the efflux of K^+ ions stops. From here, the membrane potential gradually rises and returns to its resting potential, as

the Na^+ and K^+ pumps push the ions back across the cellular membrane, allowing the cell to achieve its equilibrium. This process of opening and closing channels occurs along the axon of the neuron, and is how an action potential is "carried" along the axon and to the axon terminals [33, Chapter 1]. Figure 2.2 visualizes this process.

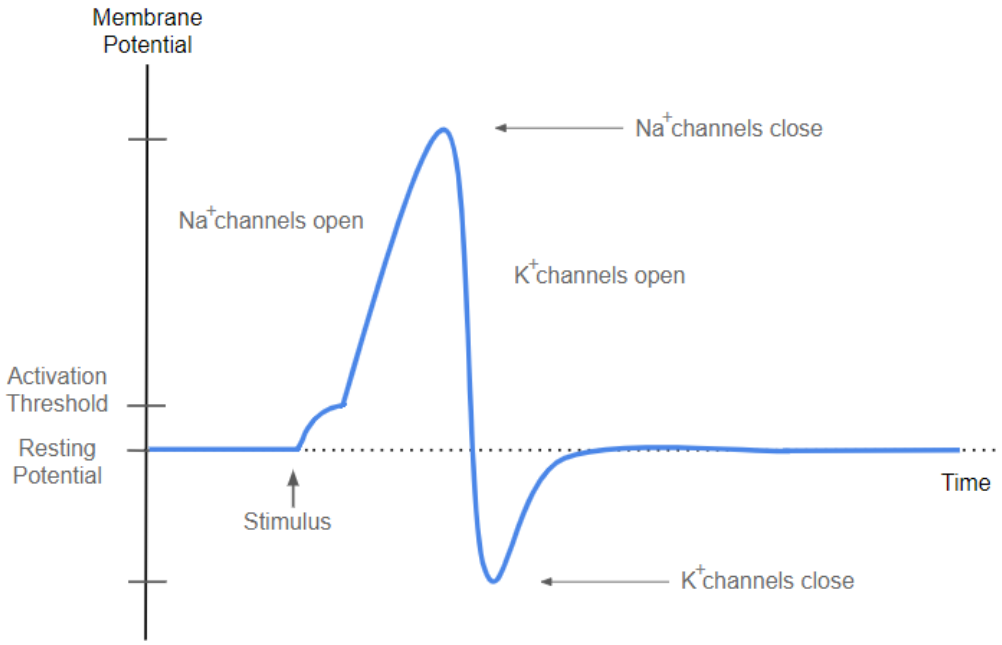

Figure 2.2: Schematic of an action potential.

2.1.4 Types of Neurons

Neurons, although structurally similar, can be classified into a number of groups based on their functions in the nervous system. As the role of a neuron is to transmit signals and communicate information, they can be divided up into groups based on how they transmit these signals and where they transmit the signals to [57, Chapter 21].

For example, three types of classifications of neurons include the following; sensory neurons, motor neurons and interneurons. Sensory neurons translate environmental stimuli, such as sound, odours, light, etc., into electrical signals, which are then translated into chemical signals and transmitted to nearby neurons. Interneurons translate these chemical signals into electrical signals again, and transmit them to neighbouring neurons. The neu-

rons that receive these signals can be motor neurons, which initiate a response in muscles, or other neurons, such as those that initiate a response in gland cells [57, Chapter 21].

In addition to these types of neurons, there are also inhibitory and excitatory labels that apply to neurons based on their chemical synapses. Neurons that secrete excitatory neurotransmitters at synapses, meaning they facilitate action potentials in their post-synaptic cells, are regarded as excitatory neurons. Similarly labelled, inhibitory neurons are those that secrete inhibitory neurotransmitters at synapses and impede the generation of action potentials in post-synaptic cells [57, Chapter 21]. In terms of the neurons we worked with for our part of the thalamocortical network, we considered the inhibitory thalamic reticular (RE) neuron, and the excitatory thalamocortical (TC) neuron.

2.1.5 Regions of the Brain

In order to understand the roles of neurons on a larger scale, we next look at the human brain and some of its structural components. Made up of billions of neurons [36], the brain is a very complex organ that is organized into various divisions, and comprised of a number of smaller substructures. Our research on childhood absence epilepsy focuses on the thalamocortical network between the thalamus and the cortex, and so here we discuss the relevant regions. Figure 2.3 shows a diagram of the brain and the locations of these relevant components.

To start, the brain is bilaterally arranged into two hemispheres; the right hemisphere and the left. The distinction between the two comes from a deep groove in the cortex (outer layer) that starts at the front of the head and runs all the way to the back. Each hemisphere of the brain is responsible for a specific set of functions, which can vary from person to person, and various nerve tracts connect the two sides [1, Chapter 2].

The cortex, as mentioned, is the outer layer of the brain and has many regional and physical divisions which are each responsible for a variety of functions. Regionally, the cortex is divided into the two hemispheres, which are then each divided in four lobes known as the frontal, parietal, temporal and occipital lobes. Within each of these regions, the cortex is physically organized into sections based on the bulges (gyri) and grooves (sulci) of the cortex, which again are each responsible for different functions. The precentral gyrus and the postcentral gyrus, for example, are the sites of the primary motor area and the primary somatosensory area, respectively. As such, they are responsible for conscious movement, as well as receiving sensory information from different parts of the body, respectively. Other divisions of the cortex are believed to hold a number of other responsibilities, such as those related to language, long-term memory, focus, visual functions and more [1, Chapter 2].

The thalamus, located at the centre of the brain and consisting of two oval masses, is responsible for sorting sensory information and relaying it to the cortex. The types of sensory information it receives comes from our hearing, sight, taste and touch, as well as sensations of pain, pressure and temperature. It is also responsible for relaying nerve impulses that initiate voluntary movement [1, Chapter 2].

The thalamocortical network is then a network that connects the thalamus and the cortex. It is comprised of neurons from the cerebral cortex, the dorsal thalamus and the reticular thalamus. The cortex and dorsal thalamus communicate via reciprocal excitatory projections that are responsible for managing activities such as motor control and sensory processing. The thalamic reticular nucleus (TRN) consists of only neurons with the inhibitory GABA transmitters, and shares in the information sent between the two regions. Specifically, it receives its sensory information indirectly, from the dorsal thalamic relay neurons, and then directs its output within the thalamus to dorsal neurons. As such, it can sense activity from the network, and then influence network behaviour through inhibition in the thalamus [41]. As mentioned, this network is believed to play a role in childhood absence epilepsy, and our research focuses on the thalamic part of this network. In the next section, we explore the topic of epilepsy and look at the biology of this disorder and specifically that of childhood absence epilepsy.

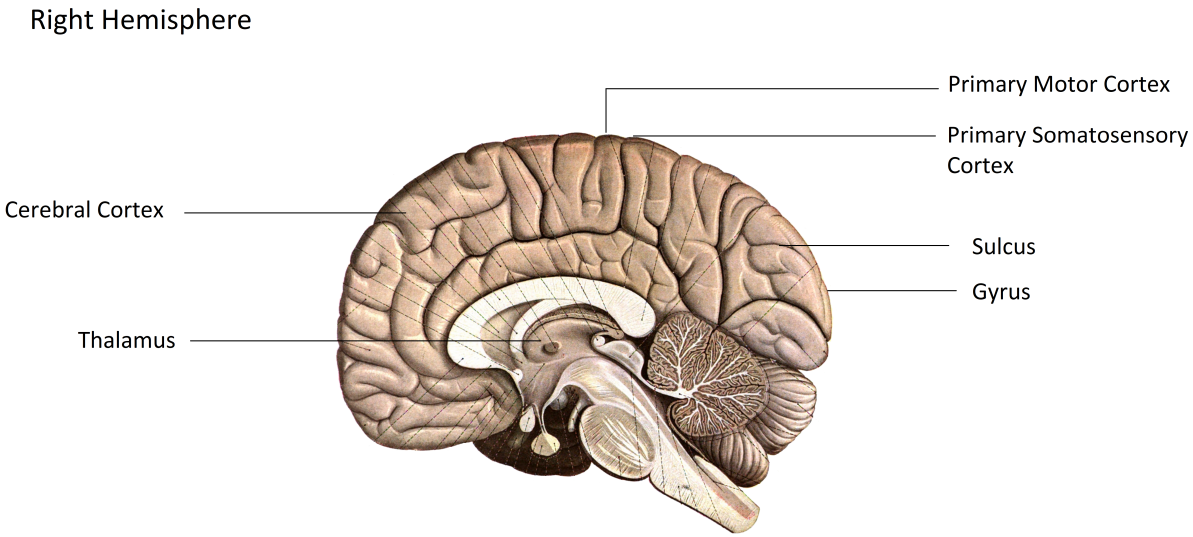

Figure 2.3: Diagram of the brain, modified from Dr. Johannes Sobotta's 1908 diagram, published in *Atlas and Text-book of Human Anatomy Volume III Vascular System, Lymphatic system, Nervous system and Sense Organs*, by W. B. Saunders company, Philadelphia, 1914 [75]. (Public Domain)

2.2 Epilepsy

Epilepsy is a neurological disorder affecting around 50 million people worldwide, or about 1% of the world's population. Generally speaking, it describes an increased predisposition to seizures in individuals, however due to the variety of causes and symptoms, it is better thought of as a collection of disorders rather than as a single disorder [88]. The International League Against Epilepsy (ILAE) and the International Bureau for Epilepsy (IBE) have defined epilepsy as,

> "A disorder of the brain characterized by an enduring predisposition to generate seizures and by the neurobiological, cognitive, psychological, and social consequences of this condition." [34]

For seizures, this was described by the organizations as,

> "A transient occurrence of signs and/or symptoms due to abnormal excessive or synchronous neural activity in the brain." [34]

2.2.1 General Information on Epilepsies

There are a number of different types of epilepsy, classified based on the cause and the type of seizure observed. To start, epileptic seizures can fall into one of two main categories; generalized or focal, with the difference being the location of origin of the seizure. Generalized seizures are believed to be caused by connected neural networks from both hemispheres of the brain, whereas focal seizures are thought to be caused by networks in only one hemisphere. From here, generalized seizures are then classified into myoclonic, atonic, tonic, tonic-clonic, and absence seizures [88]. Myoclonic seizures are characterized by short, sudden jerking movements, caused by muscular contractions [80], while atonic seizures involve a sudden, brief loss in muscle tone often causing falls [35]. Tonic seizures involve the stiffening of the body [35], and tonic-clonic seizures involve a succession of stiffening and then jerking of extremities [13]. Absence seizures on the other hand are characterized by a sudden, short impairment of consciousness [13]. The seizures can then be categorized as genetic, structural/metabolic or unknown, based on their principle cause. Oftentimes, the type of epilepsy may be determined in an individual based on characteristics such as the age of occurrence, the frequency and type of seizure activity and patterns recorded by an electroencephalogram (EEG), defined in Section 2.2.3 [88].

Remission and prognosis of the disorder depends heavily on the form of the epilepsy. For individuals with epilepsy, the disorder can either spontaneously dissipate or persist throughout their life. For cases where the epilepsy persists, often the seizures can be controlled with anti-epileptic drugs, however medication is not always effective. When seizures cannot be controlled with medication, surgical treatment can be used to help with the frequency and severity of the seizures. In many of these cases epilepsy can drastically affect the quality of one's life, and although symptoms can often be controlled with medication, the condition still has a high mortality rate [88].

Research has been conducted to attempt to determine the specific causes of different epilepsies, and to develop and improve available treatments for patients. This research includes studies on animal models as well as developing and testing computational and mathematical models.

2.2.2 Childhood Absence Epilepsy

Childhood absence epilepsy is a type of generalized epilepsy characterized by the presence of absence seizures. It is idiopathic, meaning it arises spontaneously in individuals with an unknown specified cause. It is believed to have a multifactorial genetic cause, however the specific genes responsible for inducing CAE are still unknown [13].

Although not as common as other forms of epilepsy, childhood absence epilepsy still affects a number of individuals. The incidence rate of CAE is around 2-8 children per 100,000 children under the age of 16, and it accounts for about 2-10% of all epilepsies in children. Typically, the seizures start around the ages of 3 to 8 years old and can occur multiple times a day, up to 200 incidents per day. Around 70% of individuals with CAE show spontaneous recovery, usually during adolescence, and so the disorder has a mostly benign prognosis [13].

In terms of the absence seizures, these are characterized by a distinct set of physical and electrophysiological symptoms. Physically, absence seizures are described as a sudden, short impairment of consciousness with no response to environmental stimuli or memory of events during the seizure. In many individuals this can be accompanied by twitching or other automatisms involving the eyes or limbs. For the electrophysiological symptoms, the disorder is characterized by spontaneous spike and slow-wave discharges (SWDs) recorded on an EEG. These SWDs typically have a frequency of 3 Hz, with a range of 2.5 to 4 Hz, and last for about 10 seconds, with a range of 4 to 20 seconds [13].

2.2.3 Slow Wave Discharges (SWDs)

To understand SWDs, it is important to first understand the tool that records this activity; the electroencephalogram. In 1994, Binnie and Prior described the EEG as,

> "A spatiotemporal average of synchronous postsynaptic potentials arising in radially oriented pyramidal cells in cortical gyri over the cerebral convexity." [5]

In other words, an EEG is a tool that measures the average electrical activity, or spiking activity, in the brain, coming mostly from the excitatory neurons (pyramidal cells) in the cortex and its connected networks.

A slow-wave discharge, or a spike wave discharge, is an oscillatory pattern observed on an EEG during an absence seizure, consisting of an alternation of spikes and slow waves [67]. The "spike" phase of a SWD occurs when the cells in the network spike at the same time and display mostly synchronous bursting, while the "wave" phase corresponds to a silence, or lack of neuronal activity in the cells [18]. SWDs are a network pattern, and are characterized by a frequency of 2.5-4 Hz [13].

It is believed that the thalamocortical network plays a role in the generation and propagation of these SWDs [67]. Figure 2.4 shows a hand-drawn illustration of the shape of a

typical SWD pattern that would be observed on an EEG. For an actual EEG recording showing a typical SWD pattern, we refer you to Figure 1 from Sinclair and Unwala's 2007 paper on childhood absence epilepsy [74].

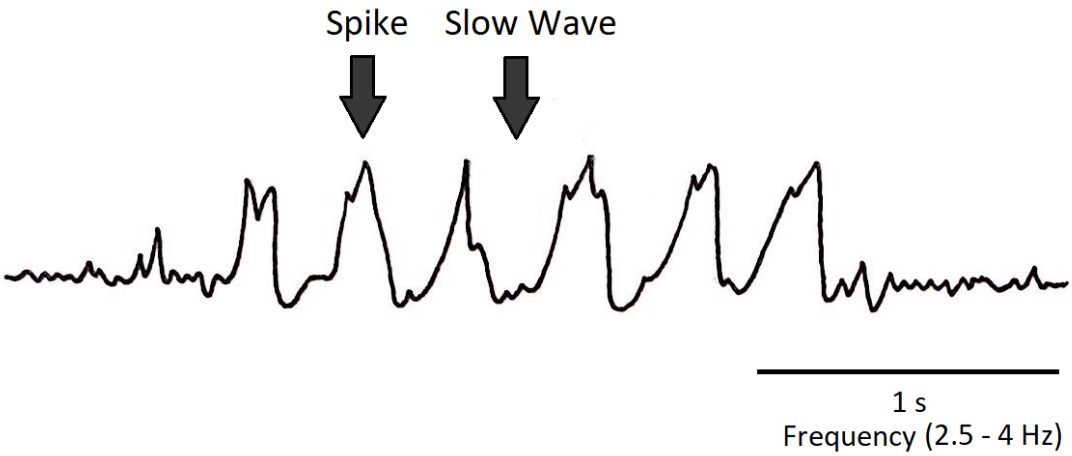

Figure 2.4: Hand-drawn illustration of a typical SWD pattern observed on an EEG during an absence seizure.

2.2.4 Causes and Genes Implicated in Childhood Absence Epilepsy

One of the reasons childhood absence epilepsy is believed to be a genetic disorder is that it is often prevalent in multiple members of the same family. It has previously been reported that it has a 16-45% positive family history rate, with 33% of first-degree relatives and 70-85% of monozygotic twins sharing this condition. In one family with a history of CAE, there may be a certain genetic mutation discovered that is believed to lead to the SWDs that are characteristic of CAE, yet this particular mutation may be absent in the DNA of another family with CAE [13]. As such, determining the specific set of genes and mutations responsible for the general case of CAE is difficult, and it is currently believed that a number of genetic mutations together may be responsible.

One example of a mutation linked to CAE is a single nucleotide polymorphism (SNP) mutation in the *GABRG2* gene, associated with the $GABA_A$ synapses. From experimental studies in 2001, Wallace et al. believed this mutation may increase the hyperexcitability of the thalamocortical network, by reducing the GABA-mediated inhibition between certain

neurons in the circuit. However, they found that this mutation was not present in all studied individuals with CAE, and therefore couldn't be classified as a sole cause to the disorder [13, 86]. Another example is a mutation in the *CACNA1A* gene. This mutation, associated with Ca^{2+} channel function, is believed to result in a 70-100% depletion in the evoked current [13]. However, due to studies by Jouvenceau et al in 2001, which associated this gene mutation with other neurological conditions such as ataxia, the *CACNA1A* mutation is believed to contribute to a unified phenotype of absence seizures and ataxia, and not solely CAE [47].

As such, the issue of determining the specific genes responsible for CAE persists, and research is still being conducted in order to solve this problem. In Section 3.2, we review a few other genes that are believed to be linked to CAE, such as the *NIPA2* gene, involved in magnesium transport, and the *CACNA1H* gene, associated with Ca^{2+} channels.

As for where the SWDs are initiated, much research has pointed to the thalamocortical loop, and specifically the somatosensory cortex, as the source of generation [15]. Early studies found patterns of increased activity in thalamocortical regions during absence seizures. Specifically, in 1995, patterns of thalamic hyperactivity were found in individuals with long-lasting CAE [71], and in 2001, hypermetabolism was found to occur in thalamic and cortical regions during seizure activity for children with CAE [44]. In 2002, experimental studies by Meeran et al. suggested the somatosensory cortex as the site of SWD initiation, with the thalamus aiding in propagating and amplifying the SWD activity [61]. Since then, further experiments on rat models of absence epilepsy, such as those by Karpova et al. in 2005 [48], Polack et al. in 2007 [68] and Polack et al. in 2009 [69], have also agreed with this cortical focus theory.

The types of neurons that initiate SWDs is still unclear, however it is currently believed that the deep-layer pyramidal neurons in the somatosensory cortex may be a root cause. Studies on GAERS (specific rat models of absence epilepsy) by Polack et al. in 2007 show that these neurons initiate the bursting of other neurons in the somatosensory cortex as well as in distant cortical areas, and that they display oscillations before and between seizure activity that convert to an epileptic pattern [68]. It was also shown in 2016 that these pyramidal neurons show an increased firing rate and a more sustained depolarization between seizure activity when compared with control neurons in GAERS, leading to an increased ability to form and lead seizure activity [87]. However, research is still being conducted in order to confirm the exact root of absence seizure initiation.

2.2.5 Genetic Absence Epilepsy Rats from Strasbourg

As neurological disorders can be difficult to ethically study on humans, animal models then become useful in order to study and better understand such disorders. As mentioned, epilepsy is one of these disorders that use animal models to carry out experimental studies. Here, we discuss the development and history of a specific type of animal model, the genetic absence epilepsy rats from Strasbourg (GAERS), which has produced a number of contributions to this field of research.

The development of absence epilepsy animal models started with species such as rodents, primates and cats, which were injected with chemical compounds such as penicillin and GABA agonists, in order to induce seizure activity. These models provided some insight into the neurological disorder, however the results were limited. Due to the forced induction of the seizures and resulting lack of recurrence in seizure activity, the animal models did not fit closely with the human condition. This then led to the development of the genetic absence epilepsy rats from Strasbourg, or GAERS, which today is still recognized as one of the most validated and predictive models for the disorder [16].

To give a bit of background on these rat models, the genetic absence epilepsy rats from Strasbourg were developed in Strasbourg, France, in 1982. The strain was created by interbreeding pairs of rats that were believed to have absence epilepsy, until a strain resulted where 100% of rats tested positive for the condition (after 3-4 generations). This strain displayed the characteristic features of absence epilepsies, with the slow wave discharges and behavioural arrests [16].

In contrast to the induced animal models, the genetic rat models displayed more similarities to the human condition. In terms of SWDs, the rats displayed a frequency of neuronal oscillations slightly higher than that observed in humans (3 Hz in humans vs 5-10 Hz in rats), however this was not considered a limitation as rats typically have different neuronal frequencies than primates [16]. Another useful feature of the GAERS model is that the level of vigilance was shown to affect the occurrence of absence seizures in the same way as humans. Specifically, the majority of SWDs occur in both species during quiet wakefulness (drowsiness) as well as in transitioning between wakefulness and slow wave sleep (deep sleep) and vice versa [53].

With these similarities to the human condition, and being a genetic model, GAERS have allowed researchers to better understand the mechanisms and genetics behind absence epilepsy and childhood absence epilepsy. Specifically, results have suggested that absence epilepsy has a dominant transmission, as the breeding between an epileptic and a non-epileptic rat, during the development of the GAERS strain, led to more than 95% of the

progeny showing SWDs after six months. They also found that the transmission of the disorder is autosomal, and not related to gender, nor is it related to a single gene, implying a multifactorial cause [16]. As will be further discussed in Section 3.2, recent studies on GAERS have suggested some specific gene mutations that may contribute to CAE, such as the *CACNA1H* mutation, associated with Ca^{2+} channels [70].

Currently, strains of GAERS are being kept in cities such as Grenoble, Paris, Melbourne, Istanbul and Cardiff in order to carry out further studies related to absence epilepsies [16].

Chapter 3

Mathematical Modelling

In this chapter we look at different topics regarding using mathematical models to represent neurons and networks in the brain. We start by discussing the basics of modelling neurons, and then review modelling literature related to childhood absence epilepsy. We finish the chapter with an overview of two modelling programs often used for biological systems.

3.1 General Modelling

Here, we look at the general method for representing neurons as mathematical models. We start by discussing the equivalent circuit, which describes the electrophysiology of neurons as a basic electric circuit, and then discuss how to model channels and synapses as mathematical equations. After this, we look at different methods of measuring the electrical properties of neurons, and review the well-known Hodgkin-Huxley model.

3.1.1 Equivalent Circuit

The activity in an electric circuit is often used to describe the electrophysiology of neurons. Specifically, it is the capacitance, the resistance and the battery in circuits that correspond to several components in neurons that affect their electrical activity. Here, we describe the similarities in the two systems [77, Chapter 10].

To start, capacitance describes the ability of an item to store and separate an electric charge. The capacitor of a circuit consists of two conducting regions of opposite charges,

separated by a material that is non-conductive. When an electric charge builds up in one region, creating an electric field, the capacitor induces a charge in the other region, creating a current in the process. In neurons, it is the cellular membrane that acts as a capacitor, as it is able to hold and separate a charge from the intracellular and extracellular solutions [14]. In both systems, the current created by the capacitor can be expressed mathematically as the following equation,

$$I = C\frac{dV}{dt} \tag{3.1}$$

Here, I represents the current, C represents the capacitance, and $\frac{dV}{dt}$ represents the change in voltage with respect to time [14].

In electrical circuits, the resistance describes the property to impede the flow of the current, and so resistors are the components that slow down the current flow. From Ohm's Law, which states that an electrical current is proportional to the voltage divided by the resistance, the quantity of current that passes through a resistor is expressed as,

$$I = \frac{V}{R} \tag{3.2}$$

With I again representing the current, R representing the resistance and V representing the voltage [14].

In terms of neurons, the ion channels act as resistors, as they control the passing of ions across the membrane. Conversely, one can use conductance, which is the reciprocal of resistance, to describe the ability and ease of a component to pass current through it. To put this into context, when more ion channels are open, more ions can pass through the membrane, meaning there is an increase in the conductance of the current, and a decrease in the resistance [14]. In many conductance-based models, the current from ion channels is represented as,

$$I = g(V - E_r) \tag{3.3}$$

Where, g represents the conductance of the channel, E_r is the reversal potential (discussed next) and $V - E_r$ is the driving force [33, Chapter 1].

In circuits, there is a difference in charge between the two sides of a battery, where one side is positive and the other is negative. This creates the voltage necessary for the flow

of the current [14]. In neurons, the concentration gradient, which describes the movement of ions from a region of high concentration to a region of low concentration, acts as the battery. E_r, or the reversal potential, is the potential created by the battery, and accounts for the difference between the intracellular and extracellular concentrations [33, Chapter 1]. A more detailed description of the reversal potential is given in Section 3.4.

Together, these three components; the capacitance, the resistance and the battery, describe the electrical properties and roles of the cellular membrane, the ion channels and the reversal potential in neurons. In the next section, we look in more detail at how to model these ion channels.

3.1.2 Modelling Channels

The basic conductance-based model for gated ion channels is given by the following,

$$I_j = \bar{g} m^q n^s (V - E_j) \tag{3.4}$$

Where I_j represents the respective current, $\bar{g}$ represents the maximum conductance of the channels, m and n are the gating variables, q and s are the number of independent components of the channels corresponding to the gating variables, V is the membrane potential and E_j is the reversal potential, or Nernst potential, for the specific ion [33, Chapter 1].

Gating Variables

The membrane-embedded proteins, representing the resistors of an electrical circuit, control the passage of ions across the cell membrane. As previously mentioned, many of these proteins have activation and inactivation gates that can open and close depending on the voltage of the cell. This opening and closing can be represented by the following kinetic scheme,

$$C \underset{\beta(V)}{\overset{\alpha(V)}{\rightleftharpoons}} O \tag{3.5}$$

C and O represent the closed and open states, respectively, while $\alpha(V)$ and $\beta(V)$ represent the rate constants at which the gates change from closed to open and vice versa, respectively [33, Chapter 1].

To represent this gating as a variable, the following equation is used,

$$\frac{dm}{dt} = \alpha(V)(1-m) - \beta(V)m \tag{3.6}$$

Where, m represents the fraction of open gates and so $1-m$ represents the fraction of closed gates. In many cases, this equation is rewritten as,

$$\frac{dm}{dt} = (m_\infty(V) - m)/\tau(V) \tag{3.7}$$

where,

$$m_\infty(V) = \frac{\alpha(V)}{\alpha(V)+\beta(V)} \qquad \text{and} \qquad \tau(V) = \frac{1}{\alpha(V)+\beta(V)} \tag{3.8}$$

For a fixed V, $m_\infty(V)$ is the steady state solution to Equation 3.7, and $\tau(V)$ is the time constant which determines the rate at which the solution approaches $m_\infty(V)$. $m_\infty(V)$ is sigmoidal in shape and is often represented by a Boltzmann function (Equation 3.9), however the shape of $\tau(V)$ is less standardized. The solution, $m(t)$, of Equation 3.7 remains between the values of 0 and 1. Experimental data can be used to fit either the $\alpha(V)$ and $\beta(V)$ or the $m_\infty(V)$ and $\tau(V)$ functions [33, Chapter 1]. For the Boltzmann sigmoid equation, given below, V_{50} represents half of the maximum voltage and k represents the slope factor.

$$I(V) = \frac{1}{1+\exp[\frac{-(V-V_{50})}{k}]} \tag{3.9}$$

The exponents on the gating variables, q and s in Equation 3.4, help to more accurately calculate the probability of a channel opening or closing. The value of these parameters correspond to the number of independent components of the channel. For example, the K^+ channel has four independent, identical components, and so the probability that the channel is open is expressed as m^4. The values for the expressions of many well-known currents have been determined by experimental data. Specifically, the values for the fast Na^+ and delayed rectifier K^+ channels were determined by Hodgkin and Huxley (see Section 3.1.5).

Reversal Potential

The reversal potential, or Nernst potential, of an ion describes the membrane potential at which this particular ion is at an equilibrium across the membrane, and the chemical and electrical forces are equal and opposite [33, Chapter 1]. As mentioned, it depends on the difference of the intracellular and extracellular concentrations of the particular ion, and can be calculated as follows,

$$E_j = -\frac{RT}{zF}\ln\frac{[\mathrm{j}]_{in}}{[\mathrm{j}]_{out}} \tag{3.10}$$

Here, E_j is the ion's Nernst Potential, R is the gas constant ($8.314\,\mathrm{Jmol^{-1}{}^{\circ}K^{-1}}$), T is the absolute temperature ($^{\circ}$K), z is the valence of the ion, F is Faraday's constant ($96\,485\,\mathrm{{}^{\circ}Cmol^{-1}}$), and $[\mathrm{j}]_{in}$ and $[\mathrm{j}]_{out}$ are the specific ion concentrations inside and outside of the cell. For many cells and ions, this value is well-known. The derivation of this formula can be found in Ermentrout and Terman's 2010 book [33, Chapter 1].

Maximal Conductance

The maximum conductance, $\bar{g}$, describes the ability of the channel to pass ions through itself, and is typically given in units of S or mS per unit area. To obtain a value for $\bar{g}$, typically experimental data is necessary in order to fit the parameter, however today there are currently many established values for channel conductance that are able to be used [33, Chapter 1].

Temperature Factor

A factor that is often considered when modelling ion channels is the temperature factor. Ion channels are sensitive to temperature, and so the higher the temperature an experiment is performed at, the faster the channels will switch between the open and closed states. In particular, the rate at which a channel switches states depends exponentially on temperature. To ensure consistency among experimental data that is collected at different temperatures, oftentimes an adjustment factor will be incorporated into the activation and inactivation equations of the channels.

The temperature factor is of the form,

$$\theta = Q_{10}^{(T-T_{exp})/10} \tag{3.11}$$

Here, $T - T_{exp}$ is the difference between the standard temperature of the model and the temperature that the experimental data was collected at. Q_{10} is the ratio of the rates for a 10 °C increase in temperature, and often has a value of 3. In Chapter 4, we incorporate a temperature factor into some of our modelled channels.

3.1.3 Modelling Synapses

In terms of modelling the synaptic currents, there are a number of ways to do this, depending on the type of synapse being modelled. The basic model however, is given as,

$$I_{syn} = g(t)(V_{post} - E_{syn}) \tag{3.12}$$

Where $g(t)$ represents the synaptic conductance, V_{post} represents the voltage of the post-synaptic cell and E_{syn} represents the reversal potential associated with the particular type of synapse [33, Chapter 1].

The conductance of synaptic currents depends on the voltage of the presynaptic cell, and therefore can be modelled in a variety of ways. One such method considers the conductance as a sum of specific functions that each depend on the spiking times of the presynaptic neuron, requiring the tracking of the spiking times of the cell, and defining the functions to sum [33, Chapter 1].

A simpler method considers the conductance as a product of a constant multiplied by a time-dependent function that represents the fraction of open channels. In this method, the conductance is then represented as,

$$g(t) = \bar{g}s(t) \tag{3.13}$$

Where the function of open channels, s(t), satisfies the following different equation,

$$\frac{ds}{dt} = a_r[T](1 - s) - a_d s \tag{3.14}$$

Here, s represents the fraction of open channels, a_r represents the rise rate of the synaptic conductance and a_d represents the decay. $[T]$ represents the concentration of

transmitter released by the presynaptic neuron, and is modelled by the following equation [33, Chapter 1],

$$[T](V_{pre}) = \frac{T_{max}}{1 + \exp[\frac{-(V_{pre} - V_T)}{K_p}]} \tag{3.15}$$

Here, V_{pre} is the voltage of the presynaptic neuron, T_{max} is the maximal concentration of transmitter in the synaptic cleft, V_T is the value for which the function is half-activated, and K_p gives the steepness of the function. From a paper published by Destexhe et al. in 1994, the suggested values for the equation are $T_{max} = 1\,\text{mM}$, $V_T = 2$, and $K_p = 5\,\text{mV}$ [26].

It is also possible to include a delay term in this version of the model to represent the time it takes for an action potential to pass through the presynaptic neuron and arrive at the receptors of the postsynaptic neuron. This delay can be modelled as $V_{pre}(t - t_{delay})$ which would replace $V_{pre}(t)$ in the above equation [33, Chapter 1].

This model for synaptic currents works for the AMPA/kainate, NMDA and GABA_A synapses described previously, however the GABA_B synapse requires a slightly different model due to the indirect binding of the transmitter to the receptors [33, Chapter 1]. The model for GABA_B synapses can be described by the following equations,

$$I_{GABA_B} = \bar{g}_{GABA_B} \frac{g^n}{K_d + g^n}(V - E_K) \tag{3.16}$$

$$\frac{dr}{dt} = a_r[T](1 - r) - b_r r \tag{3.17}$$

$$\frac{dg}{dt} = K_3 r - K_4 g \tag{3.18}$$

Here, $r(t)$ represents the receptor, $g(t)$ represents the concentration of activated G-protein, K_d is the dissociation constant of the binding of the G-protein to the potassium channels, and a_r, b_r, K_3 and K_4 are the rate constants [21]. The transmitter concentration, $[T]$, is modelled in the same way as the AMPA/kainate, NMDA and GABA_A synaptic currents.

3.1.4 Measurement Methods

In order to experimentally determine the electrical properties of neurons, there are two main methods that are used. Here we discuss the general details of the voltage-clamp and the patch-clamp techniques.

Voltage-Clamp Technique

The voltage-clamp technique was developed by Kenneth Cole and George Marmont in 1949, and involves measuring the flow of current through a specific area of the cell's membrane [39]. The basis of this technique involves holding the membrane potential of a neuron at a steady value by injecting a current of appropriate strength and direction into the axon of the cell [33, Chapter 1]. The membrane potential can then be changed in a stepwise way, and held at that potential after each step-change. This is typically done by inserting two electrodes into the axon, with one recording the membrane potential, and the other applying the current to change the potential [39]. This method can also be used with the space-clamp restriction, which uses a conductive wire inserted along the axon of the neuron to force the total current of the cell to be spatially uniform [33, Chapter 1]. Hodgkin and Huxley used a version of the voltage-clamp technique to develop their well-known model, described in Section 3.1.5 [39].

Patch-Clamp Technique

The patch-clamp technique was developed by Bert Sakmann and Erwin Neher (winners of the Nobel Prize in Physiology or Medicine in 1991) in 1976, and has since gone through many upgrades and modifications. The original method, however, involved using glass microelectrodes to isolate a patch of a cell's membrane from the extracellular solution, in order to measure the current flowing through that patch. Specifically, it is able to measure the current at the whole-cell or individual channel level. In order to obtain these measurements, the glass microelectrode is filled with a solution of electrolytes, and is pressed against the surface of the cell membrane. A high-resistance seal is then created by applying a small suction to the cell membrane, and the current measurements can then be taken [4].

3.1.5 The Hodgkin Huxley Model

In 1952, after a number of years of working together on various projects, Alan Hodgkin and Andrew Huxley published the first mathematical model of the currents involved in action potential generation, which is now known as the Hodgkin-Huxley Model. This model was not only the first quantitative description of action potential dynamics, but it laid the foundation for future electrophysiological research to come. Having had such a big impact on the scientific community, their research earned them the Nobel Prize in Physiology or Medicine in 1963, and has since led to other Nobel Prize-winning research, such as that by Erwin Neher and Bert Sakmann in 1991, concerning the functions of ion channels in cells [73].

The Hodkgin-Huxley Model itself is a conductance-based model, and was derived based on voltage-clamp data from the giant axon in squid. It models the membrane potential using three currents, and is comprised of only four differential equations. The model tracks the voltage of the cell with respect to time, and accounts for the membrane capacitance, as well as the conductance and activation kinetics of each of the channels. The model is represented by the following equations [33, Chapter 1],

$$c_M \frac{dV}{dt} = -\bar{g}_{Na} m^3 h (V - E_{Na}) - \bar{g}_K n^4 (V - E_K) - \bar{g}_L (V - E_L) \tag{3.19}$$

$$\frac{dn}{dt} = \alpha_n(V)(1 - n) - \beta_n(V) n \tag{3.20}$$

$$\frac{dm}{dt} = \alpha_m(V)(1 - m) - \beta_m(V) m \tag{3.21}$$

$$\frac{dh}{dt} = \alpha_h(V)(1 - h) - \beta_h(V) h \tag{3.22}$$

Here, c_M represents the specific membrane capacitance, which is the capacitance per square centimeter of the membrane, and is approximately $1\,\mu\text{F/cm}^2$ in most cells. The three terms represent each of the sodium, potassium and leak currents in that order, and are modelled in the same way as described in Section 3.1.2 [33, Chapter 1].

In terms of finding specific parameters and expressions in this model, Hodgkin and Huxley used a version of the voltage-clamp technique on the squid giant axon to obtain data which allowed them to derive expressions and values for their model. Specifically, they found the exponents for the gating variable parameters in this way, along with the following parameter values and equations [33, Chapter 1],

Parameters: $\bar{g}_{Na} = 120\,\text{mS/cm}^3$, $\bar{g}_K = 36\,\text{mS/cm}^3$, $\bar{g}_L = 0.3\,\text{mS/cm}^3$, $E_{Na} = 50\,\text{mV}$, $E_K = -77\,\text{mV}$, $E_L = -54.4\,\text{mV}$.

$$\alpha_n(V) = 0.01(V + 55)/(1 - \exp(-(V + 55)/10)) \tag{3.23}$$

$$\beta_n(V) = 0.125 \exp(-(V + 65)/80) \tag{3.24}$$

$$\alpha_m(V) = 0.1(V + 40)/(1 - \exp(-(V + 40)/10)) \tag{3.25}$$

$$\beta_m(V) = 4 \exp(-(V + 65)/18) \tag{3.26}$$

$$\alpha_h(V) = 0.07 \exp(-(V + 65)/20) \tag{3.27}$$

$$\beta_h(V) = 1/(1 + \exp(-(V + 35)/10)) \tag{3.28}$$

As mentioned, the Hodgkin-Huxley model is one of the most ground-breaking and well-known models describing neuron dynamics. Many known models use these dynamics, including our own described in this thesis.

3.2 Modelling Literature

As childhood absence epilepsy is a neurological disorder with an intricate, unknown set of causes, much research has been conducted in order to determine the set of factors responsible. Recently, with the advancement of technology, many mathematical models are being combined with experimental approaches in order to better understand this disorder. Here, we look at three papers related to modelling genetic defects in relation to CAE. First, we look at the work of Knox et al. in 2018 [50], who studied the paired effects of T-type Ca^{2+} channels and $GABA_A$ synapses on the thalamocortical network. We then look at the work of Vitko et al. in 2005 [85], who used experimental and computational approaches to test the effects of multiple mutations in the *CACNA1H* gene on firing patterns in CAE. Finally, we look at research by Xie et al. in 2014, who also used a combination of experimental and computational methods to analyze the effects of a mutation in a magnesium transporter gene, *NIPA2*, on CAE.

3.2.1 'Modeling Pathogenesis and Treatment Response in Childhood Absence Epilepsy,' Knox et al. (2018)

In 2018, Knox et al. published the results of their studies which looked at how T-type Ca^{2+} channels and cortical excitability affect the progression and treatment of childhood absence epilepsy. Specifically, they looked at the effects of paired changes of the T-type Ca^{2+} channels and the cortical $GABA_A$ synapses on the thalamocortical network, as well as predicted possible clinical implications of a T-type Ca^{2+} channel variant, P640L. In order to do this, they worked with a previously published computational model of the thalamocortical network, developed by Destexhe in 1998 [18]. Knox et al. chose to work with this model as it was developed to study the effects of $GABA_B$ receptors on spike and wave oscillations, and it contained detailed T-type Ca^{2+} channel modelling, which fit their interests.

The model itself is a conductance-based model, comprised of four different types of cells; cortical pyramidal neurons (PY), cortical inhibitory neurons (IN), thalamic relay neurons (TC) and thalamic reticular nucleus neurons (RE). Each cell was modelled as a single

compartment model and was comprised of three to five intrinsic currents, depending on the cell type, which were modelled in the typical Hodgkin-Huxley fashion. Each of the cell types contained the leak current (I_{Leak}) as well as the fast sodium and potassium currents (I_{Na}, I_K). The PY neuron contained an extra cortical M current (I_M), whereas the RE neuron contained the low-threshold Ca^{2+} current (I_T), and the TC neuron contained the I_T current plus the hyperpolarization-activated current (I_H).

In terms of the layout of the network, the model was set up as four one-dimensional layers of 100 cells, with each layer corresponding to one of the four cell types. For connections between the cortex and thalamus, each cell connected to 20 other cells that were adjacent to the equivalent neuron in the other layer, whereas within the thalamic and cortical layers, each cell connected to 10 adjacent cells. The AMPA and $GABA_A$ synapses were modelled as a 2-state kinetic scheme (Equation 2.1), and the $GABA_B$ synapses were modelled as a nonlinear scheme where G proteins are activated and modulate potassium channel currents (Equations 2.2 to 2.5). This is similar to the standard methods of modelling these synapses, described in Section 3.1.3 (Equations 3.12 and 3.16 to 3.18, respectively). The parameters chosen for the network were based on previous fittings to experimental voltage clamp data, which are described in more detail in their paper.

As mentioned, Knox et al. were interested in the effects of changes in the T-type Ca^{2+} channels paired with changes in cortical excitability on the thalamocortical network. To model an increased cortical excitability, they decreased the conductance of the inhibitory $GABA_A$ currents in the PY neurons, and to model changes in the T-type Ca^{2+} channels, they altered the conductance, steady state voltage shift and inactivation time for the I_T current of the RE neurons. Specifically, for a range of values of cortical $GABA_A$ conductance (0-100% of their original value), they held two of the I_T parameters at their original values and then increased and decreased the third parameter incrementally for roughly 15-20 simulations. With this, they found that spontaneous oscillations occurred every 30-40 seconds, due to the spontaneous bursting in the TC neurons. To study this further, they then applied a 100 ms stimulus to the network, between the spontaneous oscillations and after the network had returned to rest, using various current pulses on different groups of cells (700 nA into 5 PY neurons and 20 PY neurons; -100 nA into 5 TC neurons and 20 TC neurons).

With this, they observed that the stimulation-activated oscillations were found to have either a spindle pattern (8-10 Hz), a spike and wave pattern (2-4 Hz), or a transitional pattern of the two (see Figure 4.1 for a diagram comparing the two patterns). Each of these patterns lasted only 2-3 seconds due to the I_H current in the TC cells. Their main result was that an increased I_T conductance and/or inactivation time, paired with an increased cortical excitability (i.e., decreased $GABA_A$ conductance), could cause spindle

oscillations in the network to transition to spike and wave discharges. They also found that for the upper extreme values of the I_T conductance and activation time (over 300% of the original parameter value), some disorganized patterns of spike and wave oscillations eventually ceased, and with the lower extremes for these values, oscillations could not occur in the network. Further, they found that spike and wave discharges did not occur for shifts in steady state voltage activation and inactivation curves, however they did occur in the network even when the I_T and $GABA_A$ currents were absent.

They then used these results to look at possible clinical implications of a P640L T-type channel variant, which was previously linked to a decreased response to ethosuximide, an antiepileptic drug, in CAE patients. Here, they found that their model coincided with these results. Specifically, when modelling the effects of ethosuximide, there was a larger parameter space where SWDs converted to spindle oscillations, for the original T-type Ca^{2+} channels, than for the P640L channel variants. This implied the P640L variant may cause a decreased response to the drug.

The results from Knox et al. are consistent with CAE having a multigenetic cause, linking changes in T-type Ca^{2+} and $GABA_A$ currents to SWDs. Further, that SWDs may also be caused by factors other than RE T-type channels (e.g., a large enough stimulation to the network). They suggest that their model and results serve as a good starting point for further research into the importance of ion channel electrophysiology in CAE.

3.2.2 'Functional Characterization and Neuronal Modelling of the Effects of Childhood Absence Epilepsy Variants of *CACNA1H*, a T-type Calcium Channel,' Vitko et al. (2005)

In 2005, Vitko et al. published a paper detailing the results of their experiments dealing with single nucleotide polymorphisms (SNPs) of the *CACNA1H* gene that were found in CAE patients. They worked with 12 of the *CACNA1H* SNPs, and introduced these mutations into the human $Ca_v3.2$ channel to observe their biophysical properties and to observe whether they affected channel gating. They then used this data in conjunction with computational modelling to predict the channel mutations' effects on neuron firing in the thalamic circuit.

In order to obtain the biophysical data, they used a mutated human $Ca_v3.2$ complementary DNA (cDNA) strand to transfect human embryonic kidney-293 cells, which were then used for whole-cell configuration of the patch-clamp technique. As for their computational

models, they used conductance-based models of neurons in the thalamic circuit (thalamic reticular (RE) and thalamocortical (TC) neurons), based on previously developed models by Destexhe et al. in 1996 [24] and in 1998 [28]. These models were chosen as they contained detailed modelling of T-channel functions. Vitko et al. used multi-compartment models for the cells, which are models that use multiple compartments which are electrically coupled to represent the spatial geometry of a cell [33, Chapter 2]. Their models use Hodgkin-Huxley-type equations, and Vitko et al. fit their data using well-known equations such as the Goldman-Hodgkin-Katz equation for the activation kinetics, and the Boltzmann equation for the steady-state inactivation kinetics. As for the model parameters, they used their experimental data from the mutated human $Ca_v3.2$ channel as the parameters for the T-channels in the RE and TC models.

For their model set-up, based on their corresponding online model published on ModelDB, it appears they used a number of variations of the 1998 RE cell model in order to represent each of the different SNPs associated with the $Ca_v3.2$ gene, as well as the original non-mutated gene [28]. In their online file, they specifically show the models for the C456S and R788C mutants. In each of these separate SNP variations of the RE model, they considered the cell as being comprised of one, three, eight and 80 compartments. Each cell contained the I_{Na}, I_K, and I_T currents, as well as a Ca^{2+} pump, and a mechanism for a single-electrode voltage-clamp.

From their experimental results, they found that five of the 12 *CACNA1H* SNPs affected the voltage dependence of channel activation kinetics, six of the SNPs affected the inactivation kinetics, and 11 affected the transitions between the open, closed and inactivated states of the channels. From their computational models, they found that seven of the SNPs were predicted to increase firing activity in neurons, with three of these SNPs predicted to induce oscillations at a similar frequency to those produced during absence seizures. On the other hand, they also found that three of the SNPs were predicted to decrease firing activity in the neurons. In terms of their RE-TC network model, they found that after implementing the SNPs into the RE cells, the ability of the network to create spindle oscillations was not affected by most of the SNP mutations. However, for the C456S SNP, this created spontaneous oscillations that led to more frequent and longer-lasting spindles.

From their findings, Vitko et al. suggest that since $Ca_v3.2$ SNPs can increase the firing patterns of cells, mutations in this channel gene may be a cause of the spike-and-wave discharges that occur in the thalamocortical network during absence seizures. However, because of the discrepancies in their findings, they believe that the *CACNA1H* gene may play only partial role in childhood absence epilepsy, and that other gene mutations may be responsible as well.

3.2.3 'Functional Study of *NIPA2* Mutations Identified from the Patients with Childhood Absence Epilepsy,' Xie et al. (2014)

As childhood absence epilepsy is believed to be a multifactorial genetic condition, with genes such as the *CACNA1H* mutation already addressed, Xie et al. decided to study the *NIPA2* gene mutation and its relation to the disorder. Their 2014 paper details their experimental and computational approaches to study the effects of the *NIPA2* mutation on intracellular Mg^{2+} concentrations, and how a decrease in this concentration may affect the hyperexcitability of the thalamocortical network. They used techniques such as immunofluorescence labeling, MTT metabolic rate detection, inductively coupled plasma-optical emission spectroscopy (ICP-OES) and computational modelling for their experiments.

In terms of the gene itself, they reference a previous study where three mutations in the *NIPA2* gene were found within a population of CAE patients [46]. *NIPA2* belongs to the *NIPA* family of proteins, which function as magnesium (Mg^{2+}) transporters. The *NIPA2* gene itself is specifically responsible for transferring extracellular Mg^{2+} into the cytoplasm of cells. Based on previous studies which found that *NIPA1* mutations may hinder the transport of the proteins within the cell to the extracellular membrane [6], Xie et al. hypothesized that mutations in the *NIPA2* gene may also have similar effects. Xie et al. predict that with less transport to the extracellular membrane, there may be an increase in the number of *NIPA2* proteins in the cell, leading to a decrease in the intracellular Mg^{2+} concentration.

In terms of childhood absence epilepsy, Xie et al. note that NMDA receptors are involved in excitatory synaptic transmissions within the thalamocortical network, and are affected by the Mg^{2+} concentrations of the cell. Specifically, the activation of the NDMA receptor channels is partially blocked by intracellular Mg^{2+}. As such, Xie et al. hypothesized that a decrease in the intracellular Mg^{2+} concentration may affect NMDA receptor function and therefore affect the hyperexcitability of the thalamocortical network.

For their experimental studies, they used neuron cultures from Sprague-Dawley rats (another type of experimental rat model), and transfected them to obtain the *NIPA2* mutation. They used immunofluorescence to study the localization of the *NIPA2* proteins, MTT metabolic rate detection to measure the viability of the mutated cells and the ICP-OES to measure the intracellular and extracellular Mg^{2+}.

As for the computational modelling, they modified a previously developed model of an NMDA receptor by Destexhe et al. in 1994 [25, 26], which presented a kinetic method

for modelling synaptic transmissions. As Destexhe's model accounted for the blocking of NMDA receptors by extracellular Mg^{2+}, Xie et al. implemented an additional term in the model to account for the blocking by intracellular Mg^{2+} as well. The model they used is a conductance-based model, assumed to be for general neurons in the thalamocortical network. Their model includes the NMDA synapse, a calcium pump, the fast sodium and potassium currents and possibly the high threshold Ca^{2+} current, although it is unclear whether the authors included this last current. It is also assumed that their simulations are of a two-cell network.

Their experimental studies showed that *NIPA2* mutations led to a decrease in the intracellular Mg^{2+} concentration of the cells, although the transfected neurons' viability were not affected. From their computational approach, they found that with a low intracellular Mg^{2+} concentration, representing the result of a *NIPA2* mutation, there was an increase in the amplitude of the post-synaptic potential during bursting, implying the mutation may increase the NMDA-related synaptic currents. In conclusion, they suggest that this study could give insights for further exploration of the pathogenesis and treatment development for childhood absence epilepsy.

3.3 Modelling Programs

Mathematical models are typically run and evaluated using different kinds of computer programs. As a variety of programs exist, the choice of program depends on what one wants to accomplish with their model, as well as individual preference. NEURON is used for many well-known models, including those by Destexhe et al. in 1994 [22] and in 1996 [21] that we based our model on, however we chose to use the program, XPPAUT. Here, we discuss these two programs.

3.3.1 NEURON

NEURON is a computer program designed to simulate models of neurons. Many computational neuroscience models are run using NEURON, including the model for the thalamic reticular network by Destexhe et al. in 1994 [22], and the model for the thalamocortical and thalamic reticular network also published by Destexhe et al. in 1996 [21]. NEURON was created by Michael Hines, Ted Carnevale and John W. Moore, where the latter, interestingly enough, along with Toshio Narahashi, discovered that tetrodotoxin, the lethal toxin found in pufferfish, is a blocker of sodium channels [64]. The program is coded in

the programming language, C, and has the useful features where one can specify neuron properties, as well as control the simulation and graph the results [38].

The basic idea behind NEURON is that it divides the cable equation, representing the cell or network of cells, into a set of connected sections. These connected sections, which can take the form of any kind of branched tree, together represent the total area of membrane that contains all channels and mechanisms relevant to determining the membrane potential of the cell, or cells, involved. The sections are then divided into subsections of equal length, where the area of each subsection is determined based on the placement of a node at the centre of each subsection, plus an additional node at the distal end of each section. NEURON is then able to calculate each section's circuit parameters based on the positions of these nodes. This differs from many other neuron simulation programs, where it is left to the user to not only decide how to divide the cable into a number of sections, but also how to calculate the parameters in each section [38].

In terms of computations, either the implicit Backward Euler method of integration, or an integration method similar to the Crank and Nicholson method can be selected to compute the membrane voltage [11]. For modelling specific membrane mechanisms, NEURON incorporates the high-level model description language, NMODL, which allows users to define the mechanism in a simple way [51]. For example, chemical reactions can be implemented using arrows to define the reactions between the components. This is unlike the program XPPAUT, described in the next section, which requires using standard mathematical equations to represent various processes. Along with chemical reactions, this system also allows for other membrane mechanisms such as kinetic schemes, the Hodgkin-Huxley equations, voltage clamp processes and more, to be easily defined by the user. The program also has the benefit of a unit checking feature.

3.3.2 XPPAUT

Often, one can model the processes present in a neuron using a system of ordinary differential equations. This usually starts with a principal equation representing the change in intracellular potential with respect to time, and follows with equations representing specific ion channels as well as their gating variables [59]. Other cellular mechanisms, such as intracellular calcium dynamics, receptor-mediated synapses and transmitter concentration can be represented by differential equations as well. Together, the system of ODEs should represent the properties of interest in the cell.

One can then use a numerical tool to simulate and solve the system of ODEs. For our models we chose the computer program, XPPAUT (or XPP), which was developed by

Bard Ermentrout. This program was based on the program, PHASEPLANE, developed by Ermentrout and John Rinzel. The program allows one to simulate, animate and analyze dynamical systems using a user-friendly interface. Not only does XPP feature a number of different solvers for a variety of systems (e.g., stiff and nonstiff systems, discrete systems, stochastic systems, etc.), but it also includes tools to perform a variety of other tasks as well. Some examples of these are stability analysis, computation of nullclines and vector fields, statistical analyses, computation of one-dimensional invariant manifolds and more. As its name suggests, XPP also has a linked feature to the bifurcation package, AUTO, written by Eusebius Doedel, where users can perform bifurcation analyses and compute fixed points, limit cycles, equilibria and other points of interest[31, 32].

For our neuron models, we mostly used XPPAUT to track the membrane potential and different currents of the cells with respect to time, and analyzed the resulting graphs and data points. For our simulations, we used a step size (Dt) of 0.01, and the Runge-Kutta method of integration.

Chapter 4

Cell Models

For this thesis, we aimed to develop a mathematical model of part of the thalamocortical network in order to study its role in childhood absence epilepsy. To do this, we modelled both an individual thalamic reticular (RE) and thalamocortical (TC) neuron, and then combined these to create the RE-TC thalamic network. We then altered certain components of the model, including synaptic and ionic current conductances, as well as inactivation rates for certain channels, in order to test their effects on the occurrence of slow-wave discharges. The development and results of our modelled network are presented in these next two chapters.

4.1 RE Cell Model

Thalamic reticular (RE) neurons are known to have oscillatory and intrinsic bursting properties, leading to spindle wave oscillations in networks. These spindle waves, which are often observed during the first stages of the sleep cycle, consist of alternating waxing and waning oscillations of about 7 to 14 Hz. Studies from 1945 by Morison and Bassett [62] and from 1987 by Steriade et al. [78] suggested the thalamus as the generator of these synchronized oscillations, and that clusters of RE neurons can generate spindle rhythmicity on their own. Similar to the SWD pattern, spindle oscillations describe a type of network activity and are illustrated in Figure 4.1, along with an illustration of a SWD pattern, for comparison. For an actual EEG recording showing a typical spindle pattern, we refer you to Figure 1 from Contreras et al.'s 1997 paper on spindle oscillations in the cortex and thalamus [9]. Figure 4.14 shows an illustration of waxing and waning oscillations.

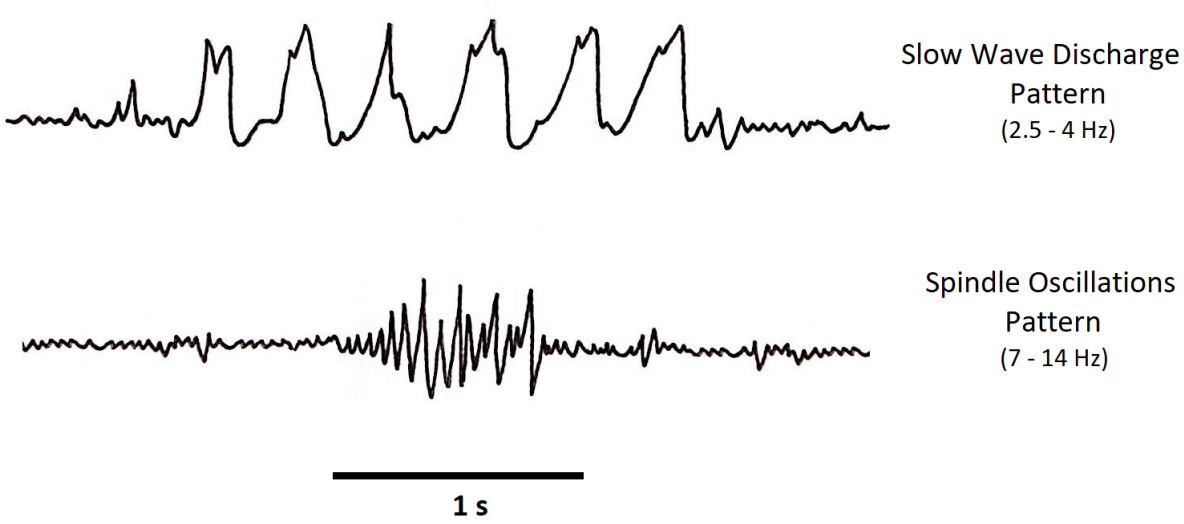

Figure 4.1: Hand-drawn illustrations of typical SWD and spindle oscillation patterns that would be observed on an EEG.

In order to study this rhythmicity of RE neurons, Destexhe et al. presented a model of the RE neuron in 1994 [22]. From this model, they found that the intrinsic bursting properties of the modelled RE cells are a result of two calcium-activated currents and a low-threshold calcium current, and that synchronized oscillations can result from the presence of many $GABA_A$ synapses between cells.

Our RE neuron model was largely based on this 1994 model by Destexhe et al., with some adjustments made according to another model presented by Destexhe et al. in 1996 [21]. The focus of the 1994 model was to study the oscillatory and intrinsic bursting properties of RE cells [22], while the 1996 model focused on synchronized oscillations and propagating waves in a RE-TC network [21]. An online version of the 1994 model is available in the online database for computational neuroscience models, ModelDB [22].

The Model

Destexhe et al. implemented their 1994 model using NEURON as a single compartment model with a surface area of $1000\,\mu m^2$, and the intrinsic currents were modelled using Hodgkin-Huxley kinetics. The equation for the membrane potential with respect to time is given as the following differential equation,

$$C_m\dot{V} = -I_L - I_T - I_{K[Ca]} - I_{CAN} - I_{Na} - I_K - I_{GABA_A} - I_{AMPA} - I_{GAP} \tag{4.1}$$

Where C_m represents the specific capacitance of the membrane ($1\,\mu F/cm^2$), V represents the membrane potential (mV), and t represents the time (ms). The intrinsic currents (mA/cm^2) are the leak current (I_L), the low-threshold Ca^{2+} current (I_T), the fast Na^+ and K^+ currents (I_{Na} and I_K), and the $GABA_A$ and AMPA synapses. It is noted that the $GABA_A$ and AMPA synapses are only considered when the RE cell is paired with another RE cell or TC cell, respectively, and the Gap junction is only considered in networks of RE cells.

Originally our model included a Ca^{2+}-dependent K^+ current ($I_{K[Ca]}$) and a Ca^{2+}-dependent nonspecific cation current (I_{CAN}), like the 1994 model, however we removed these to better fit the 1996 version of the RE model presented by Destexhe et al. [21]. Destexhe et al. note that although these currents have an effect on individual cell behaviour, they do not have significant influence on network behaviour, and so they removed them for simplicity. As such, we also removed these currents for simplicity in our network models. The equations for these currents, however, are still presented in this section. It is also noted that although there are other currents present in RE neurons, the intrinsic currents mentioned here should account for the main properties observed in RE neurons [22].

Unless otherwise specified, the equations were based on the model presented by Destexhe et al. in 1994, and kinetics were assumed to be at a temperature of 36 °C [22]. The $GABA_A$ and AMPA synapses were derived based on the model presented by Destexhe et al. in 1996 [21].

I_L: The Leak Current

The leak current accounts for the passive movement of ions across the cell membrane through nongated channels [33, Chapter 1]. It was modelled based on the formulation presented by Destexhe et al. in 1994, as given here.

Parameters: $g_L = 0.05\,mS/cm^2$, $EL = -78\,mV$

$$I_L = g_L(V - E_L) \tag{4.2}$$

I_T: The Low-threshold Ca^{2+} Current

The low-threshold Ca^{2+} current mediates the rebound burst response observed in RE neurons [22]. The current is described as "low-threshold", since its activation threshold is more negative than other thresholds. Typically, this threshold is around $-55\,\mathrm{mV}$, which is $15\,\mathrm{mV}$ lower than the threshold for Na^+ spikes [40]. The current was characterized by voltage-clamp methods in RE cells of rats obtained by Huguenard and Prince in 1992 [43]. The activation function and time constants were said to be obtained from experimental results, given by J. Huguenard via personal communication. It is also noted that the calcium reversal potential was calculated by the Nernst relation, however the RE model on ModelDB uses a value of $120\,\mathrm{mV}$, and so we used this value as well.

Parameters: $\bar{g}_{Car} = 1.75\,\mathrm{mS/cm^2}$, $E_{Ca} = 120\,\mathrm{mV}$

$$I_T = \bar{g}_{Car} m^2 h (V - E_{Ca}) \tag{4.3}$$

$$\dot{m} = -\frac{1}{\tau_m(V)}(m - m_\infty(V)) \tag{4.4}$$

$$\dot{h} = -\frac{1}{\tau_h(V)}(h - h_\infty(V)) \tag{4.5}$$

$$m_\infty(V) = \frac{1}{1 + \exp[\frac{-(V+52)}{7.4}]} \tag{4.6}$$

$$\tau_m(V) = 0.44 + \frac{0.15}{\exp[\frac{V+27}{10}] + \exp[\frac{-(V+102)}{15}]} \tag{4.7}$$

$$h_\infty(V) = \frac{1}{1 + \exp[\frac{V+80}{5}]} \tag{4.8}$$

$$\tau_h(V) = 22.7 + \frac{0.27}{\exp[\frac{V+48}{4}] + \exp[\frac{-(V+407)}{50}]} \tag{4.9}$$

I_{Na} and I_K: The Fast Na^+ and K^+ Currents

These currents, responsible for the generation of action potentials [33, Chapter 1], were modelled based on kinetics from a model of hippocampal pyramidal cells presented by Traub and Miles in 1991 [82]. A voltage shift of $-55\,\mathrm{mV}$ was used to account for the

different convention used by Traub and Miles, where they shifted their voltage variable so that the resting membrane potential was 0 mV [83].

Parameters: $\bar{g}_{Na} = 100\,\mathrm{mS/cm^2}$, $E_{Na} = 50\,\mathrm{mV}$, $\bar{g}_K = 10\,\mathrm{mS/cm^2}$, $E_K = -95\,\mathrm{mV}$, $V_{traub} = -55\,\mathrm{mV}$

$$I_{Na} = \bar{g}_{Na} m^3 h (V - E_{Na}) \tag{4.10}$$
$$I_K = \bar{g}_K n^4 (V - E_K) \tag{4.11}$$

$$\dot{m} = \alpha_m(V)(1 - m) - \beta_m m \tag{4.12}$$
$$\dot{h} = \alpha_h(V)(1 - h) - \beta_h h \tag{4.13}$$
$$\dot{n} = \alpha_n(V)(1 - n) - \beta_n n \tag{4.14}$$

$$\alpha_m = \frac{0.32(13 - (V - V_{traub}))}{\exp[\frac{13-(V-V_{traub})}{4}] - 1} \tag{4.15}$$
$$\beta_m = \frac{0.28((V - V_{traub}) - 40)}{\exp[\frac{(V-V_{traub})-40}{5}] - 1} \tag{4.16}$$

$$\alpha_h = 0.128 \exp[\frac{17 - (V - V_{traub})}{18}] \tag{4.17}$$
$$\beta_h = \frac{4}{\exp[\frac{40-(V-V_{traub})}{5}] + 1} \tag{4.18}$$

$$\alpha_n = \frac{0.32(15 - (V - V_{traub}))}{\exp[\frac{15-(V-V_{traub})}{5}] - 1} \tag{4.19}$$
$$\beta_n = 0.5 \exp[\frac{10 - (V - V_{traub})}{40}] \tag{4.20}$$

$I_{K[Ca]}$: The Ca^{2+}-Dependent K^+ Current

The slow Ca^{2+}-dependent K^+ current mediates an afterhyperpolarization (AHP) after each burst in RE cells [22]. The current was modelled based on the dynamics of channel opening via Ca^{2+} binding, and activation parameters were chosen to match data from in

vitro experiments on rats performed by Avanzini et al. in 1989 [2] and in vivo experiments on cats by Contreras et al. in 1993 [10] and Mulle et al. in 1986 [63]. The activation kinetics corresponded to a temperature of 22 °C, and so an adjustment factor was included.

Parameters: $\bar{g}_{K[Ca]} = 10\,\mathrm{mS/cm^2}$, $E_K = -95\,\mathrm{mV}$, $n = 2$, $\alpha = 48\,\mathrm{ms^{-1}mM^{-2}}$, $\beta = 0.03\,\mathrm{ms^{-1}}$, $t_{adj} = 3^{(36-22)/10} = 4.655$

$$I_{K[Ca]} = \bar{g}_{K[Ca]} m^2 (V - E_K) \tag{4.21}$$

$$\dot{m} = -\frac{1}{\tau_m([Ca]_i)}(m - m_\infty([Ca]_i))t_{adj} \tag{4.22}$$

$$m_\infty([Ca]_i) = \frac{\alpha[Ca]_i^n}{\alpha[Ca]_i^n + \beta} \tag{4.23}$$

$$\tau_m(V) = \frac{1}{\alpha[Ca]_i^n + \beta} \tag{4.24}$$

I_{CAN}: The Ca^{2+}-Dependent Nonspecific Cation Current

This current mediates afterdepolarizations (ADPs) in RE cells [22]. Destexhe et al. mention that no data for the voltage dependence of I_{CAN} was available when they were developing their model, and so the model assumed the same activation kinetics as $I_{K[Ca]}$, but slower. Here, m was determined by Equations 4.22 - 4.24, but with different values for α and β.

Parameters: $\bar{g}_{CAN} = 0.25\,\mathrm{mS/cm^2}$, $E_{CAN} = -20\,\mathrm{mV}$, $n = 2$, $\alpha = 20\,\mathrm{ms^{-1}mM^{-2}}$, $\beta = 0.002\,\mathrm{ms^{-1}}$, $t_{adj} = 3^{(36-22)/10} = 4.655$

$$I_{CAN} = \bar{g}_{CAN} m^2 (V - E_{CAN}) \tag{4.25}$$

I_{GABA_A}: The $GABA_A$ Synaptic Current

As described in more detail in Section 2.1.2, the synaptic currents regulate the transmission of signals between cells. Here, the $\mathrm{GABA_A}$ current represents the transmission of signals from one RE cell to another RE cell. The model for this current presented by Destexhe et al. in 1996 was developed based on whole cell recorded synaptic currents in

hippocampal neurons, from Otis and Mody in 1992 [66], Otis et al. in 1993 [65], and Xiang et al. in 1992 [89].

For modelling the transmitter concentration, Destexhe et al. used a model that required tracking the spiking times of the cells. In order to simplify our model we used the formulation given by Ermentrout and Terman [33, Chapter 1], which is also detailed in Section 2.1.2. In the 1996 paper, α was set to $20\,\mathrm{ms}^{-1}\mathrm{mM}^{-1}$, β to $0.16\,\mathrm{ms}^{-1}$ and E_{GABA} to $-85\,\mathrm{mV}$, however the model on ModelDB used the values presented below, which we also used in our model.

We also included a unit conversion factor, K_{RE}, to account for the difference in how NEURON and XPPAUT implement synapses. For example, the maximal synaptic conductances given in the NEURON model are in µS, whereas our XPPAUT model uses $\mathrm{mS/cm}^2$. This conversion factor was included in each of the synaptic currents in our models, and was calculated as Equation 4.28 for the RE cell using the surface area of the cell, $14\,300\,\mu\mathrm{m}^2$, from Destexhe's 1996 model [21].

Parameters: $K_{RE} = 6.993\,006\,\mathrm{mS/\mu Scm}^2$, $E_{GABA_A} = -80\,\mathrm{mV}$, $\alpha = 10.5\,\mathrm{ms}^{-1}\mathrm{mM}^{-1}$, $\beta = 0.166\,\mathrm{ms}^{-1}$, $C_{max} = 0.5\,\mathrm{mM}$, $V_{try} = 2$, $K_p = 5\,\mathrm{mV}$

$$I_{GABA_A} = rK_{RE}\bar{g}_{GABA_A}(V - E_{GABA_A}) \tag{4.26}$$

$$\dot{r} = \alpha \frac{C_{max}}{1 + \exp[\frac{-(V_{pre} - V_{try})}{K_p}]}(1 - r) - (\beta r) \tag{4.27}$$

$$K_{RE} = \frac{10^{-3}mS}{1\mu S} \cdot \frac{1}{1.43 \cdot 10^4 (10^{-4}cm)^2} = \frac{10mS}{1.43\mu Scm^2} = \frac{6.993006mS}{1\mu Scm^2} \tag{4.28}$$

The conductance, $\bar{g}_{GABA_A}$ (µS), varies depending on which cells are involved in the network, and will be discussed further in Sections 4.4 and 4.5.

I_{AMPA}: The AMPA Synaptic Current

Here, the AMPA current represents the transmission of signals from TC cells to RE cells. The AMPA synaptic current was modelled in the same way as the $\mathrm{GABA_A}$ synaptic currents, with many of the same parameters. The surface area conversion factor was also included here.

Parameters: $K_{RE} = 6.993\,006\,\mathrm{mS/\mu Scm^2}$, $E_{AMPA} = 0\,\mathrm{mV}$, $\alpha = 0.94\,\mathrm{ms^{-1}mM^{-1}}$, $\beta = 0.18\,\mathrm{ms^{-1}}$, $C_{max} = 0.5\,\mathrm{mM}$, $V_{try} = 2$, $K_p = 5\,\mathrm{mV}$

$$I_{AMPA} = rK_{RE}\bar{g}_{AMPA}(V - E_{AMPA}) \tag{4.29}$$

Similarly, $\bar{g}_{AMPA}$ (µS) varies depending on which cells are involved in the synaptic connections, and will be discussed more in Section 4.5.

I_{GAP}: The Gap Junctions

Gap junctions, representing the electrical synapses between cells, were only included in the RE networks. Although not presented in Destexhe et al.'s 1994 model, studies by Landisman et al. in 2002 [52], Lee et al. in 2014 [54] and Zolnik and Connors in 2016 [91] detail the existence of gap junctions between neurons in the thalamic reticular nucleus. As such, we included these junctions in our model. The gap junction was modelled as the sum of electrical inputs into the present cell, as presented here.

Parameters: $\bar{g}_{GAP} = 0.0005\,\mathrm{mS/cm^2}$, $n =$ the number of cells connecting to the present cell

$$I_{GAP} = \sum_{i=1}^{n} \bar{g}_{GAP}(V - V_i) \tag{4.30}$$

Intracellular Calcium Dynamics

The intracellular calcium dynamics were simply modelled as the combination of the entry of calcium into the cell via the I_T current, its removal by an active pump and an equilibrium term. The equilibrium term was not included in the 1994 paper by Destexhe et al., however it was included in the model on ModelDB.

The first term includes a unit conversion factor k, along with Faraday's constant F, and the depth of a shell around the membrane for which calcium enters into, d. This shell accounts for the region near the membrane where calcium interacts with the channels. The second term includes rate constants acquired from a Michaelis Menton approximation of the calcium pump, K_T and K_d, and the final term includes the steady state calcium value, Ca_{inf}, and the time constant for calcium removal, τ_r. The parameters were chosen to fit experimental data from voltage clamp techniques on rodent and cat thalamocortical neurons [59, 20].

Parameters: $k = 10\,\mu\text{A/cm}^2$, $d = 1\,\mu\text{m}$, $F = 96\,485.332\,^\circ\text{Cmol}^{-1}$, $K_T = 0.0001\,\text{mM/ms}^{-1}$, $K_d = 0.0001\,\text{mM}$, $Ca_{inf} = 0.000\,24\,\text{mM}$, $\tau_r = 100\,\text{ms}$

$$[\dot{Ca}]_i = -\frac{k}{2Fd} I_T - \frac{K_T [Ca]_i}{[Ca]_i + K_d} + \frac{Ca_{inf} - [Ca]_i}{\tau_r} \tag{4.31}$$

As mentioned, our RE neuron model does not include the $I_{K[Ca]}$ and I_{CAN} currents, and so in this version of the model the intracellular calcium dynamics are not used.

4.2 TC Cell Model

When paired with RE neurons, thalamocortical (TC) neurons are believed to aid in the generation, propagation and termination of spindle waves. Specifically, it is the intrinsic and synaptic properties of the cells, such as the level of membrane potential and the bursting properties of thalamic cells, that are believed to cause this [21].

In 1996, Destehe et al. developed a model to study the role of the RE-TC interactions in the generation of these spindles. From previous experimental results by Steriade et al. in 1993 [79] and Kim et al. in 1995 [49], Destexhe et al. proposed that spindle waves could be initiated by spontaneous spikes in either the TC or RE neuron, which would evoke either an AMPA-mediated excitatory response in RE cells or a GABA-mediated inhibitory response in TC cells, respectively. This would then evoke the appropriate response in the other cell and start a cycle. They also showed that along with the intrinsic and synaptic properties mentioned above, the hyperpolarization-activated current, I_H, plays a role in the generation and termination of these spindle waves [21].

We initially considered three different papers for our model, and developed one prior to the model presented here. The first model developed was based on a paper by McCormick and Huguenard in 1992 [59], which included additional currents such as the persistent depolarization-activated Na^+ current (I_{Nap}), the high-threshold Ca^{2+} current (I_L; note the same notation as our leak current), the Ca^{2+}-activated K^+ current (I_C), the transient and depolarization-activated K^+ current (I_A), the slowly inactivating and depolarization-activated K^+ current (I_{K2}), the Na^+ leak current (I_{Naleak}), and excluded the potassium current (I_K).

We initially chose this, as it appeared to have the most animal-consistent data, with the majority of the currents based on data from rats. However, there were many complications with this model and we could not get the model to function as expected. Specifically, when

implementing the equations given in their paper, we were not able to reproduce the results in their paper nor behaviour that is typical of TC neurons. As there was no published code to refer to, we decided to pursue other options. We then considered a model presented by Destexhe et al. in 1993 [20], yet there were far fewer currents incorporated than what we were looking for.

After these attempts, we decided to develop our model based on the model presented by Destexhe et al. in 1996 [21], with some adjustments made according to a model presented by Huguenard and McCormick in 1992 [42]. The alterations to this model were due to issues with modelling the hyperpolarization-activated current, I_H, and will be discussed later. An online version of the 1996 model by Destexhe et al. is presented on the website, ModelDB [21].

The Model

Destexhe et al. implemented their 1996 model using NEURON as a single compartment model with a surface area of approximately $29\,000\,\mu m^2$. The intrinsic currents were modelled using Hodgkin-Huxley kinetics. The equation for the membrane potential with respect to time is given as the following differential equation,

$$C_m\dot{V} = -I_L - I_T - I_H - I_{KL} - I_{Na} - I_K - I_{GABA_A} - I_{GABA_B} \tag{4.32}$$

Here, C_m represents the specific capacity of the membrane ($1\,\mu F/cm^2$), V represents the membrane potential (mV), and t represents the time (ms). The intrinsic currents (mA/cm^2) are the leak current (I_L), the low-threshold Ca^{2+} current (I_T), the hyperpolarization-activated current (I_H), the leak potassium current (I_{KL}), the fast Na^+ and K^+ currents (I_{Na} and I_K), and the $GABA_A$ and $GABA_B$ synapses, with the latter two currents only considered when the TC cell is paired with another RE cell.

It is noted that although a potassium A current (I_A) is observed in TC cells, Destexhe et al. did not incorporate the current in their model. Instead, they added a positive shift in action potential threshold, to mimic the delay in spike generation during bursting activity caused by the I_A current. In their paper, they have a positive shift of 20 mV, however we used a positive shift of 30 mV. This is accounted for in the Traub-convention shift parameter in the I_{Na} and I_K equations.

Destexhe et al. also note that their model was modified from previous models presented by Destexhe et al. in 1993 [20], Huguenard and McCormick in 1992 [42] and by McCormick and Huguenard in 1992 [59]. They also note that they only considered the currents believed

to be necessary for generating the spindle and bicuculline-induced synchronized oscillations [21].

Similar to the RE model, to account for the difference in how NEURON and XPPAUT implement synapses, we included a unit conversion factor for the synaptic currents. The TC surface area conversion factor was calculated as equation 4.33 using the surface area of the cell, 29 000 µm^2, from Destexhe's 1996 model [21].

$$K_{TC} = \frac{10^{-3}mS}{1\mu S} \cdot \frac{1}{2.9 \cdot 10^4 (10^{-4}cm)^2} = \frac{10mS}{2.9\mu S cm^2} = \frac{3.448275mS}{1\mu S cm^2} \tag{4.33}$$

Unless otherwise specified, the equations were based on the models presented by Destexhe et al. in 1996 [21] and in their online model [21], and kinetics are assumed to be at a temperature of 36 °C.

I_L: The Leak Current

The leak current is given as the following equation,

Parameters: $g_L = 0.01\,\mathrm{mS/cm^2}$, $E_L = -70\,\mathrm{mV}$

$$I_L = g_L(V - E_L) \tag{4.34}$$

I_T: The Low-threshold Ca^{2+} Current

The kinetics of the low-threshold Ca^{2+} current were developed based on the model presented by Huguenard and McCormick in 1992 [42], who based their model on data from voltage-clamp recordings of thalamic neurons in rats, collected by Huguenard and Prince in 1992 [43]. Unlike in the RE model, here the steady state value was used for the activation variable, m, rather than a first-order equation. The inactivation kinetics were fit to data collected at a temperature of 24 °C, and so a temperature adjustment factor was included. According to the ModelDB file, a shift of 2 was incorporated in the activation kinetics to account for a screening charge [21]. The reversal potential was calculated as shown below, where k is a unit conversion factor, T is the temperature, R is the universal gas constant, F is the Faraday constant and $[Ca]_o$ and $[Ca]_i$ are the Ca^{2+} concentrations outside and inside of the cell, respectively.

Parameters: $g_T = 2\,\mathrm{mS/cm^2}$, $t_{adj} = 3^{(36-24)/10} = 3.73719$, $k = 1000\,\mathrm{mV/V}$, $R = 8.314\,51$ $\mathrm{Jmol^{-1}{}^\circ K^{-1}}$, $T = 309.15\,^\circ\mathrm{K}$, $F = 96\,485.332\,^\circ\mathrm{Cmol^{-1}}$, $[Ca]_o = 0.000\,24\,\mathrm{mM}$, $[Ca]_i = 2\,\mathrm{mM}$

$$I_T = \bar{g}_T m_\infty(V)^2 h(V - E_{Ca}) \tag{4.35}$$

$$E_{Ca} = k\frac{RT}{2F}\log\frac{[Ca]_o}{[Ca]_i} \tag{4.36}$$

$$\dot{h} = \frac{1}{\tau_h(V)}(h_\infty(V) - h)t_{adj} \tag{4.37}$$

$$m_\infty(V) = \frac{1}{1 + \exp[\frac{-((V+2)+57)}{6.2}]} \tag{4.38}$$

$$h_\infty(V) = \frac{1}{1 + \exp[\frac{(V+2)+81}{4}]} \tag{4.39}$$

$$\tau_h(V) = 30.8 + \frac{211.4 + \exp[\frac{(V+2)+113.2}{5}]}{1 + \exp[\frac{(V+2)+84}{3.2}]} \tag{4.40}$$

I_H: The Hyperpolarization-Activated Cation Current

The hyperpolarization-activated cation current is dependent on the voltage and intracellular calcium in TC cells, and is believed to be responsible for the waning phase of spindle oscillations [21]. Destexhe et al. modelled this current using a single-variable kinetic scheme, where calcium influences the voltage dependence and conductance via the indirect binding of Ca^{2+} to a regulating protein.

For us, there were complications when attempting to model the current in this way. We were unable to understand how NEURON implemented its kinetic reactions into differential equations, and the 1996 paper gave only the kinetic schemes for the current and not the differential equations representing these schemes. Our implementation of the kinetic reactions into mathematical equations did not produce the desired results, and in many cases our model crashed when running the simulations.

As such, we modelled the I_H current based on the formulation presented by Huguenard and McCormick in 1992 [42], which used a standard Hodgkin-Huxley approach. In Huguenard and McCormick's 1992 paper, the I_H current was derived based on voltage-clamp recordings of in vitro guinea pig dorsal lateral geniculate relay neurons, obtained by McCormick and Pape in 1990 [60].

Parameters: $\bar{g}_H = 0.01\,\mathrm{mS/cm^2}$, $E_H = -40\,\mathrm{mV}$

$$I_H = \bar{g}_h m(V - E_h) \tag{4.41}$$

$$\dot{m} = \frac{1}{\tau_m(V)}(m_\infty(V) - m) \tag{4.42}$$

$$m_\infty(V) = \frac{1}{1 + \exp[\frac{V+75}{5.5}]} \tag{4.43}$$

$$\tau_m(V) = \frac{1}{\exp[-14.59 - (0.086V)] + \exp[-1.87 + 0.0701V]} \tag{4.44}$$

I_{KL}: The Potassium Leak Cation Current

The potassium leak current is responsible for the passive movement of potassium across the cell membrane. This current was developed to fit data from guinea pig thalamocortical relay neurons in vitro, as described by McCormick and Huguenard in 1992 [59]. Originally, Destexhe et al. used a conductance of 4 nS, however we converted the value to account for the cell's surface area by implementing our TC conversion factor, K_{TC}.

Parameters: $g_{KL} = 0.013\,793\,\mathrm{mS/cm^2}$, $E_{KL} = -100\,\mathrm{mV}$

$$I_{KL} = g_{KL}(V - E_{KL}) \tag{4.45}$$

I_{Na} and I_K: The Fast Na^+ and K^+ Currents

As with the RE cell, these currents were modelled based on the kinetic equations by Traub and Miles in 1991 [82]. A voltage shift of $-25\,\mathrm{mV}$ is used in the activation and time constant equations to account for both the different convention used by Traub and Miles, as well as the positive shift of 30 mV to mimic the absent I_A current.

Parameters: $g_{Na} = 90\,\mathrm{mS/cm^2}$, $E_{Na} = 50\,\mathrm{mV}$, $g_K = 10\,\mathrm{mS/cm^2}$, $E_K = -100\,\mathrm{mV}$, $V_{traub} = -25\,\mathrm{mV}$

$$I_{Na} = \bar{g}_{Na} m^3 h(V - E_{Na}) \tag{4.46}$$

$$I_K = \bar{g}_K n^4(V - E_K) \tag{4.47}$$

I_{GABA_A}: *The $GABA_A$ Synaptic Current*

The $GABA_A$ synaptic currents were modelled in the same way as the RE cell (Equations 4.26 and 4.27). Here, the $GABA_A$ current represents the transmission of signals from the RE cells to the TC cells. The only difference in the equations from the RE model is the surface area conversion factor, $K_{TC} = 3.448\,275\,\mathrm{mS/\mu Scm^2}$.

I_{GABA_B}: *The $GABA_B$ Synaptic Current*

Here, the $GABA_B$ currents represent the transmission of signals from the RE cells to the TC cells. These synaptic currents were also based on whole cell recorded synaptic currents in hippocampal neurons, from the references listed in the $GABA_A$ synaptic currents section in the RE cells. The details for the modelling of $GABA_B$ synapses are included in Section 2.1.2. The transmitter concentration was modelled in the same way as for the $GABA_A$ and AMPA synapses, based on Ermentrout and Terman [33, Chapter 1], and is included directly in the activated receptor equation, $\dot{R}$.

Parameters: $K_{TC} = 3.448\,275\,\mathrm{mS/\mu Scm^2}$, $E_{GABA_B} = -95\,\mathrm{mV}$, $K_d = 100\,\mu\mathrm{M}^4$, $K_1 = 0.5\,\mathrm{mM^{-1}ms^{-1}}$, $K_2 = 0.0012\,\mathrm{ms^{-1}}$, $K_3 = 0.18\,\mathrm{ms^{-1}}$, $K_4 = 0.034\,\mathrm{ms^{-1}}$, $C_{max} = 0.5\,\mathrm{mM}$, $V_{try} = 2$, $K_p = 5\,\mathrm{mV}$,

$$I_{GABA_B} = K_{TC}\bar{g}_{GABA_B}\frac{G^4}{G^4 + K_d}(V - E_{GABA_B}) \tag{4.48}$$

$$\dot{R} = K_1\frac{C_{max}}{1 + \exp[\frac{-(V_{pre} - V_{try})}{K_p}]}(1 - R) - K_2 R \tag{4.49}$$

$$\dot{G} = K_3 R - K_4 G \tag{4.50}$$

The conductance, $\bar{g}_{GABA_B}$ (µS), also varies depending on which cells are involved in the network, and will be discussed more in Section 4.5.

4.3 Individual Cell Tests

To ensure each of our models displayed the correct electrophysiological properties as the cells they represent, we ran a number of simulation-based tests using the program XPPAUT. These tests determined the resting potential as well as the response of the models

when injected with a current of varying strengths and polarizations. We also tested for the effects of each ionic current on the models, and tested the intrinsic bursting properties of the TC model. We also looked at the RE cell model's dynamics when arranged in a network of only RE cells.

4.3.1 RE Cell

Injected Current

We considered the response of an individual RE cell in the following situations: with no external stimuli; with a depolarizing current of $2\,\mu A/cm^2$ applied for 100 ms between 50 ms and 150 ms; and with a hyperpolarizing current of $-1\,\mu A/cm^2$ applied for 100 ms between 50 ms and 150 ms. We first considered the model without the $I_{K[Ca]}$ and I_{CAN} currents, referred to as the *reduced model*, and then considered the model which includes these two currents, referred to as the *full model*. The initial condition for the membrane potential was set to $-74\,mV$. Figure 4.2 gives a visual representation of the full and reduced RE cell models, and the intrinsic currents involved in each. Figures 4.3 and 4.4 illustrate the results of the tests, and Figures 4.5 and 4.6 display the traces for each of the currents in the models during these tests. As a note, we found that implementing a step size of 0.01 in our simulations (as mentioned in Section 3.3.2) was sufficient to resolve the spikes produced by our models.

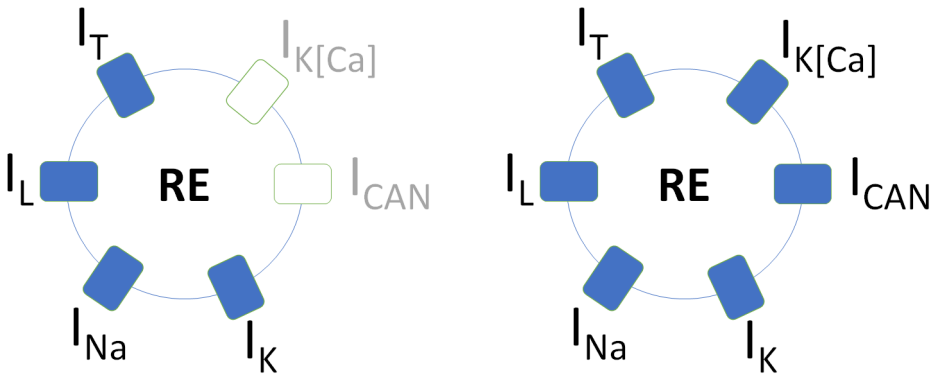

(a) (b)

Figure 4.2: Visual representations of the reduced and full RE cell models. (a): Reduced RE model. (b): Full RE model.

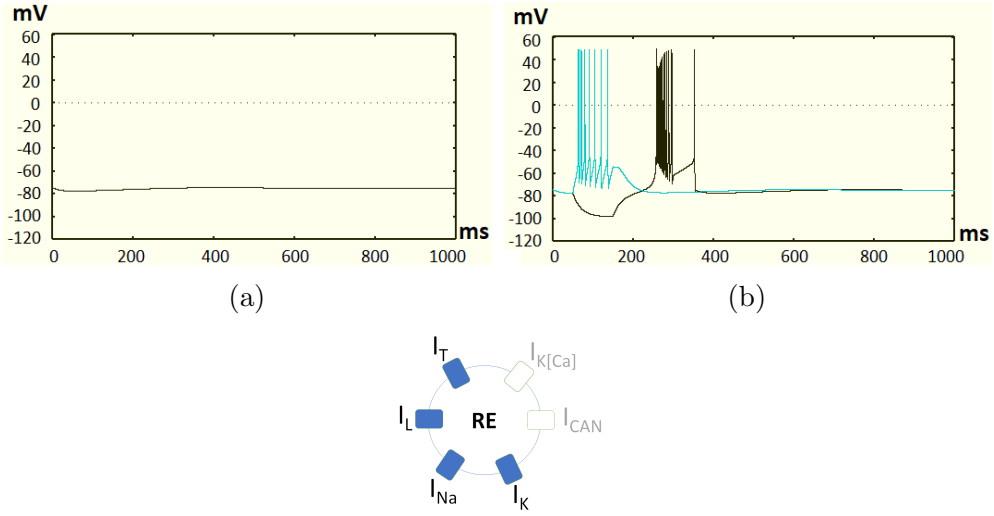

Figure 4.3: Individual RE cell (*reduced*) with external stimuli (mV vs ms). (a): With no input. (b): With $2\,\mu A/cm^2$ input (blue trace) and $-1\,\mu A/cm^2$ input (black trace).

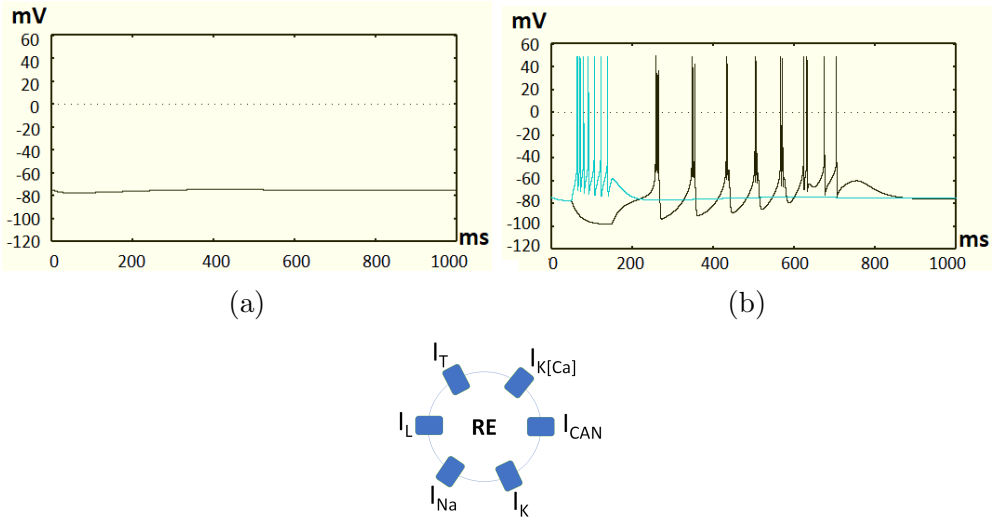

Figure 4.4: Individual RE cell (*full*) with external stimuli (mV vs ms). (a): With no input. (b): With $2\,\mu A/cm^2$ input (blue trace) and $-1\,\mu A/cm^2$ input (black trace).

For the most part, both the reduced and full models gave similar results. Without any external stimuli, the RE cells remained at resting potential around $-74\,\mathrm{mV}$. While applying the depolarizing input, the cells produced a series of spikes and then returned to resting potential when the current was removed. When the negative current was applied, the reduced model became hyperpolarized until the current was removed, and then produced a rebound burst followed by a single spike before returning to resting potential. The full model responded to the negative current by producing a rebound train of bursts, due to the extra activity from the $I_{K[Ca]}$ and I_{CAN} currents.

In both of these cases, the results correspond to typical RE cell behaviour, where bursts are only produced when cells are elicited with external stimuli and otherwise remain quiescent at around $-70\,\mathrm{mV}$ [22]. The low-threshold Ca^{2+} current (I_T), which is responsible for rebound burst responses in RE cells [22], is known to activate when the membrane potential becomes adequately hyperpolarized [7]. As such, the response of our model to the hyperpolarizing current also makes sense.

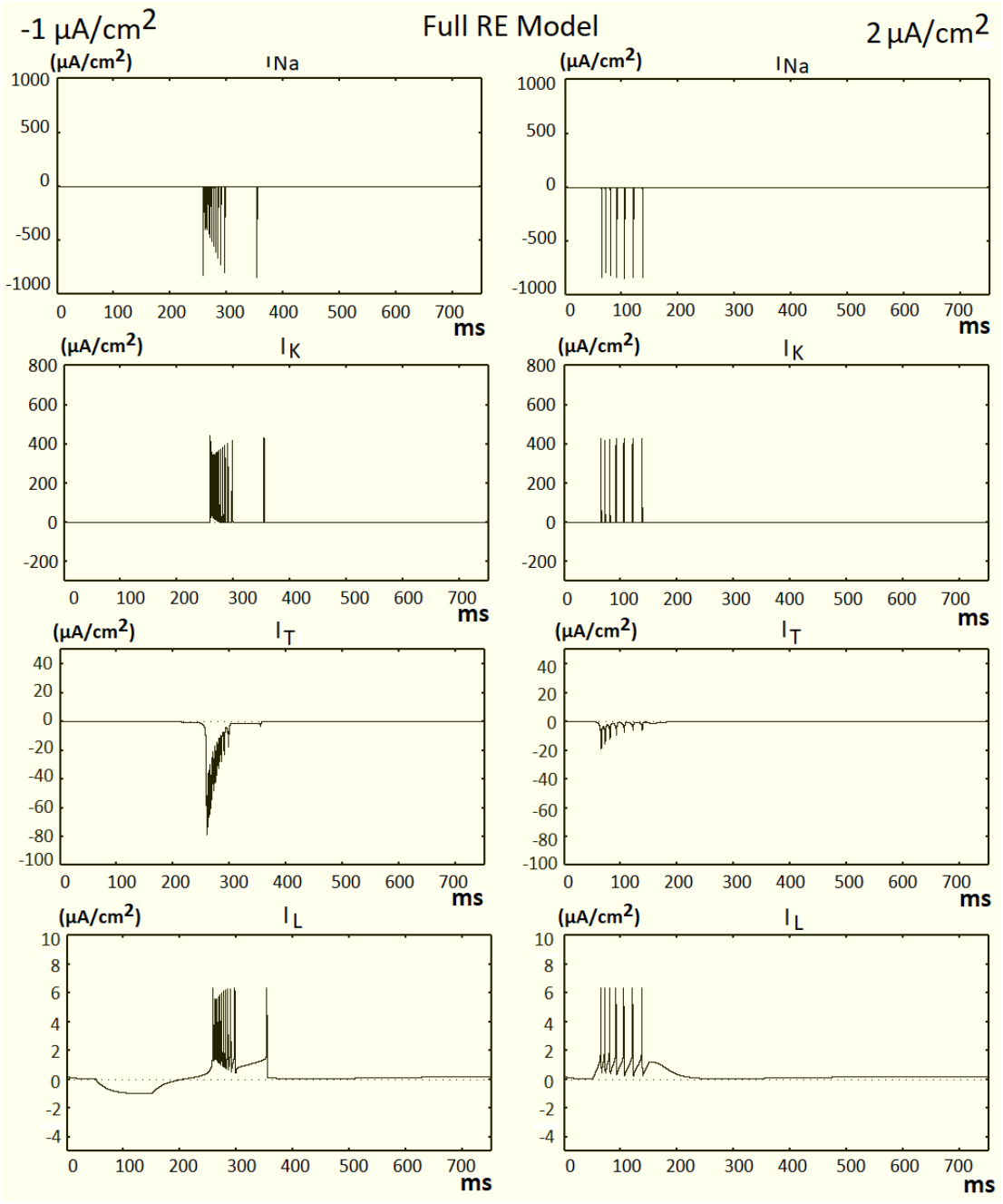

Figure 4.5: Current traces for the reduced RE cell (μA/cm^2 vs ms). *Note the change in scale of the vertical axis for each row of diagrams.*

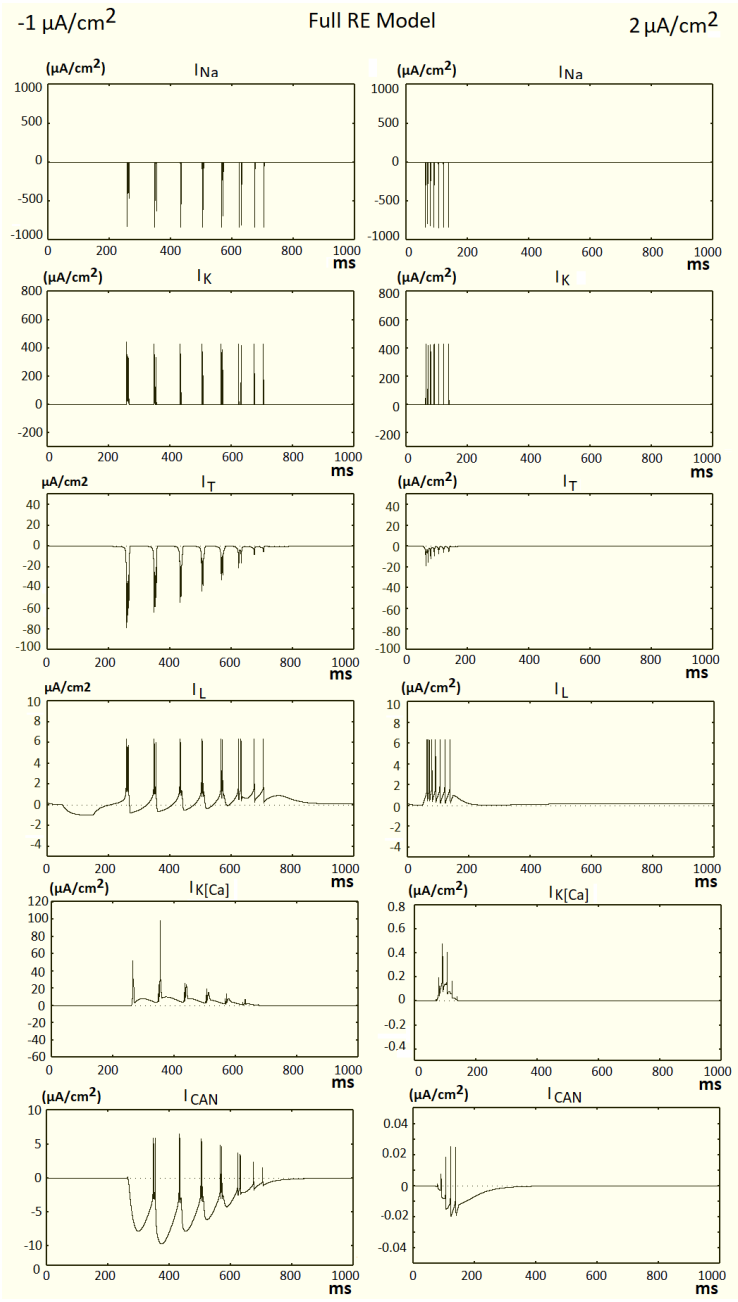

Figure 4.6: Current traces for the full RE cell (μA/cm^2 vs ms). *Note the change in scale of the vertical axis for each row of diagrams.*

Effect of Each Current

Next, we studied the effects of the intrinsic currents on the RE cell, by only considering certain currents in our model at a time. For each combination of currents considered, we tested the model in the same way as before, by applying the same temporary depolarizing and hyperpolarizing inputs. Specifically, we implemented currents of $2\,\mu A/cm^2$ and $-1\,\mu A/cm^2$, for 100 ms, applied between 50 ms and 150 ms in each case. Table 4.1 summarizes the results of these tests for each combination of currents considered. The following paragraphs give a more detailed description of the results of these tests, and Figures 4.7 to 4.10 illustrate the results. As a note, Table 4.1 includes a summary for the full and reduced models, however we exclude the details and figures of these results here, as they are presented under the *Injected Current* heading in Section 4.3.1.

Table 4.1: Summary of the Effects of Each Current on the RE Membrane Potential

Figure	**Currents**	**Positive Input**	**Negative Input**
Fig. 4.7	I_L	Passive rise, then rest	Passive fall, then rest
Fig. 4.8	I_L, I_{Na}, I_K	Spiking, then rest	Passive fall, then rest
Fig. 4.3	I_L, I_{Na}, I_K, I_T	Spiking, then rest	Passive fall, then rebound burst and rest
Fig. 4.9	I_L, I_{Na}, I_K, I_T, $I_{K[Ca]}$	Spiking, then rest	Passive fall, then rebound oscillating bursts
Fig. 4.10	I_L, I_{Na}, I_K, I_T, I_{CAN}	Spiking, then rest	Passive fall, then rebound tail of spikes that decrease in frequency, then rest
Fig. 4.4	I_L, I_{Na}, I_K, I_T, $I_{K[Ca]}$, I_{CAN}	Spiking, then rest	Passive fall, then rebound train of bursts and then rest

The model with only I_L showed typical results for a cell with only passive currents (Figure 4.7). Without external stimuli, the cell reached resting potential at a slightly lower value of $-78\,mV$, and with the depolarizing and hyperpolarizing inputs, the membrane potential increased and decreased respectively. When I_{Na} and I_K were added (Figure 4.8), the cell had a similar resting potential as the I_L model, and it responded to the

hyperpolarizing input in the same way. With the depolarizing input the cell produced a series of spikes before returning to resting potential. This coincides with the idea behind the Hodgkin-Huxley model (Section 3.1.5), implying that the I_{Na} and I_K currents are necessary in order to generate action potentials in our model.

When I_T and $I_{K[Ca]}$ were added (Figure 4.9), without external stimuli, the cell stayed at the typical RE resting membrane potential of $-74\,\text{mV}$. With the positive input, the cell responded with a train of spikes, and with the negative input, the cell responded with rebound oscillating bursts. The interactions between the two currents would explain this behaviour, as $I_{K[Ca]}$ is responsible for afterhyperpolarizations after each burst in RE cells, and I_T has a lower activation threshold and mediates the rebound burst response in the cells. Specifically, in response to the applied negative input, the I_T current evokes a rebound burst, while $I_{K[Ca]}$ then lowers the membrane potential in response to this burst, which again activates the I_T current and another burst is produced, and the cycle continues. As such, our results here appear to make sense, and coincide with the results presented in Figure 2 (a) of Destexhe et al.'s 1994 paper [22].

For the model with I_T and I_{CAN}, and without $I_{K[Ca]}$ (Figure 4.10), the response of the model at rest and with a positive input was similar to the previous model, however the response to the negative input was different. Instead of oscillating bursts, there is a tail of spikes which eventually decreases in frequency and then terminates as the cell returns to resting potential. Our results here are similar to those presented in Figure 2 (d) of Destexhe et al.'s 1994 paper [22]. Their results showed that when I_{CAN} was implemented with a larger conductance value, in order to make the current dominate, a tail of spikes occurred in response to a hyperpolarizing input, which also eventually decreased in spike frequency before terminating.

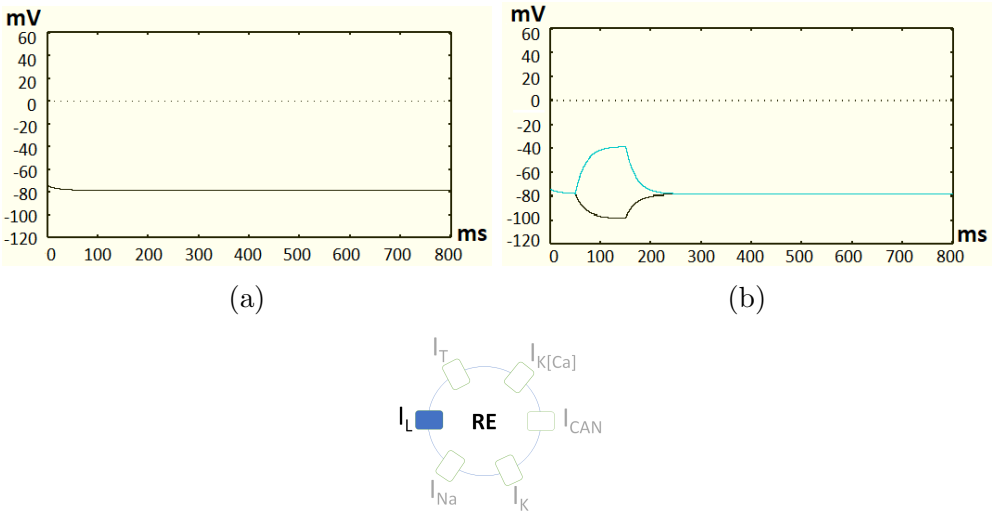

Figure 4.7: Individual RE cell, only I_L included (mV vs ms). (a): With no input. (b): With $2\,\mu A/cm^2$ input (blue trace) and $-1\,\mu A/cm^2$ input (black trace)

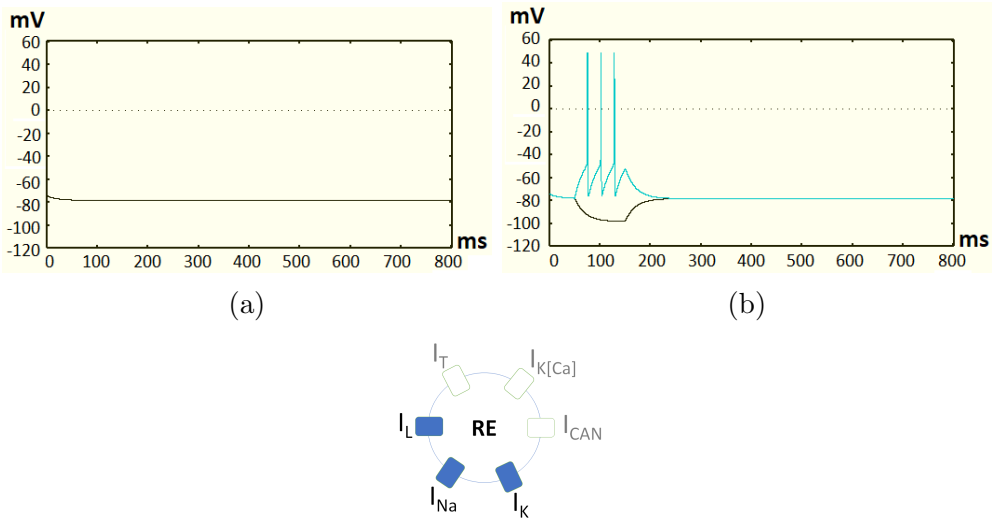

Figure 4.8: Individual RE cell, only I_L, I_{Na} and I_K included (mV vs ms). (a): With no input. (b): With $2\,\mu A/cm^2$ input (blue trace) and $-1\,\mu A/cm^2$ input (black trace)

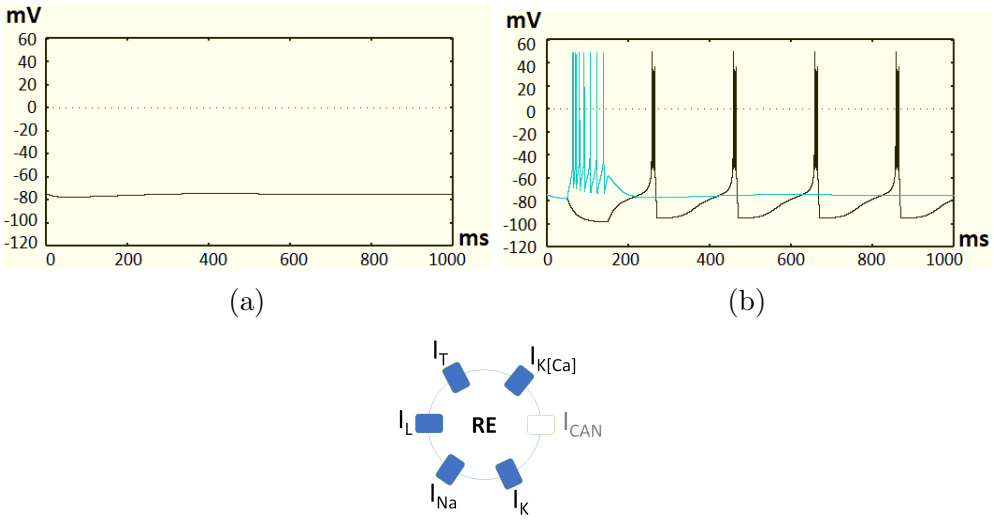

Figure 4.9: Individual RE cell, only I_L, I_{Na}, I_K, I_T and $I_{K[Ca]}$ included (mV vs ms). (a): With no input. (b): With $2\,\mu A/cm^2$ input (blue trace) and $-1\,\mu A/cm^2$ input (black trace)

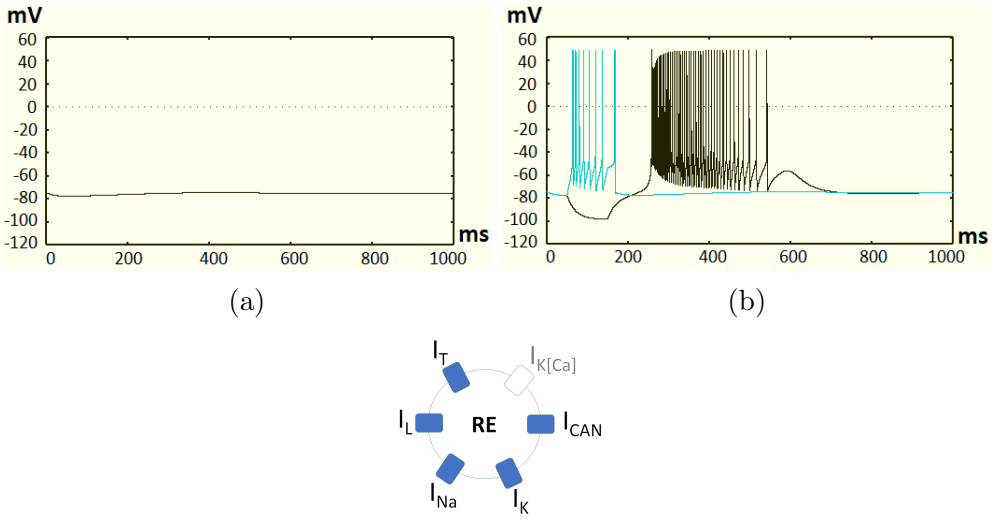

Figure 4.10: Individual RE cell, only I_L, I_{Na}, I_K, I_T and I_{CAN} included (mV vs ms). (a): With no input. (b): With $2\,\mu A/cm^2$ input (blue trace) and $-1\,\mu A/cm^2$ input (black trace)

4.3.2 TC Cell

Injected Current

Our TC model was tested in much the same way. We considered an individual TC neuron with no external stimuli, with a depolarizing current of $3\,\mu A/cm^2$, applied for 100 ms between 50 ms and 150 ms, and with a hyperpolarizing current of $-1\,\mu A/cm^2$, applied for 100 ms between 50 ms and 150 ms. Figure 4.11 gives a visual representation of the TC cell model, and the intrinsic currents involved. Figure 4.12 illustrates the results, and Figure 4.13 shows the traces for each of the currents in the model during the tests.

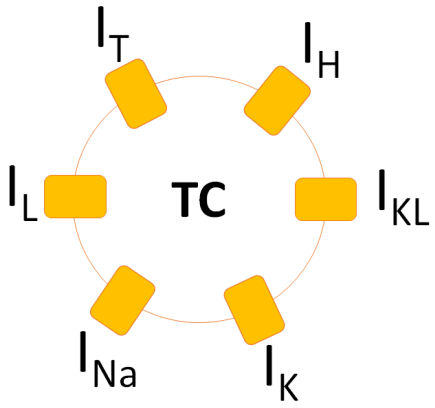

Figure 4.11: Visual representation of the TC cell model.

With no external stimuli, the cell displayed spontaneous bursting. While applying the depolarizing current, the cell produced a train of spikes and then returned to resting potential where it resumed spontaneous bursting. With the applied negative current, the cell became hyperpolarized and upon removal of the current produced a rebound burst before returning to spontaneous bursting.

Our model displayed many similar properties to typical TC cells. Destexhe et al. note in their 1996 paper [21] that due to the I_T and I_H currents, TC cells have the ability to generate either spontaneous oscillations, or produce rebound burst firing after a brief hyperpolarization. Both the spontaneous oscillations and the hyperpolarization-activated rebound burst firing properties are observed in our model. In addition, results from Deschenes et al. in 1984 [17] and Jahnsen and Llinás in 1984 [45], showed that guinea pig and rat TC neurons display trains of action potentials in response to depolarization, which is also displayed in our model.

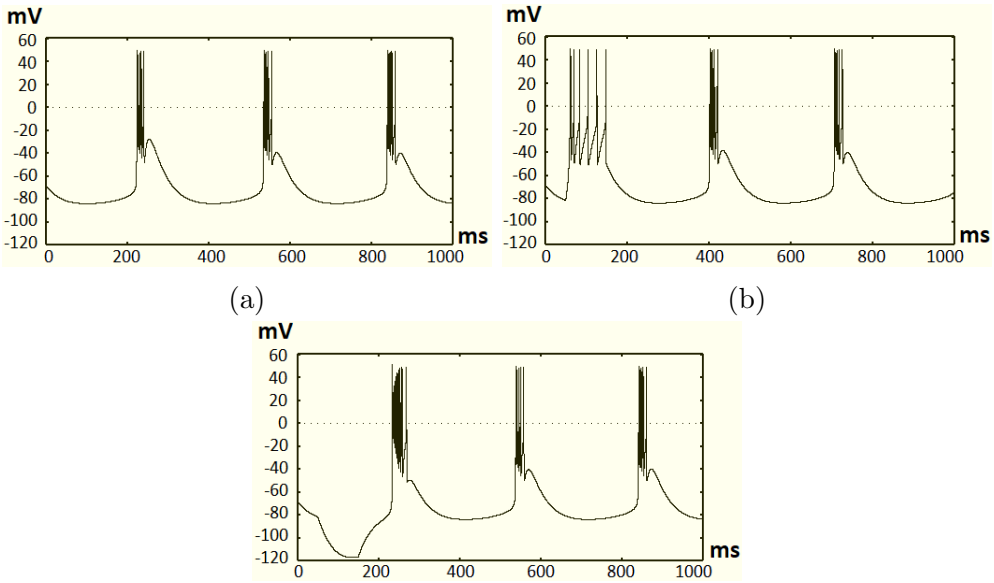

Figure 4.12: Individual TC cell with external stimuli (mV vs ms). (a): With no input. (b): With $3\,\mu A/cm^2$ input. (c): With $-1\,\mu A/cm^2$ input.

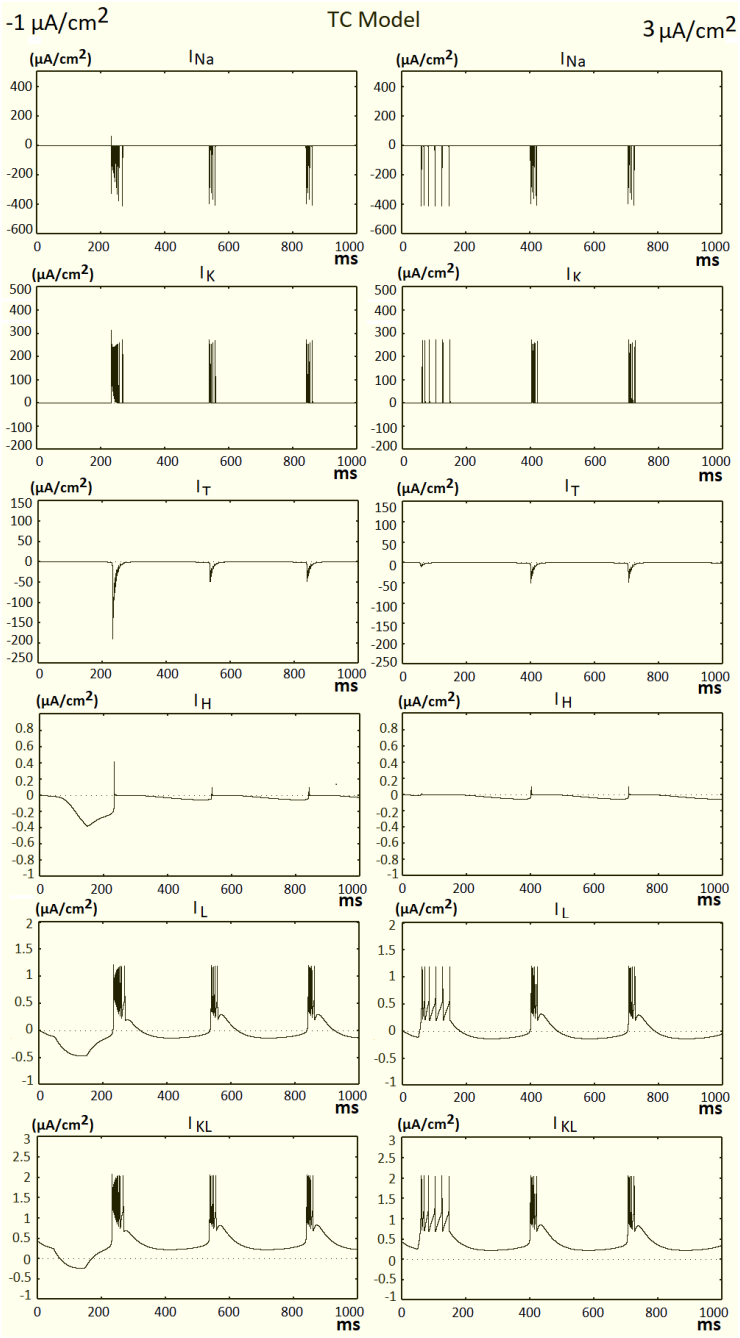

Figure 4.13: Current traces for the TC cell (μA/cm^2 vs ms). *Note the change in scale of the vertical axis for each row of diagrams.*

Intrinsic Bursting Property

Waxing and waning is a type of oscillatory bursting pattern, where cells exhibit periods of bursts, with the amplitude of the bursts oscillating throughout the period. Figure 4.14 shows an illustration of the shape of waxing and waning bursts, compared with the shape of regular continuous bursting. In Destexhe et al.'s 1996 model, the waxing and waning behaviour was the default model for their TC cells, however they found that their cells were also able to exhibit delta oscillations as well as a rest state [21].

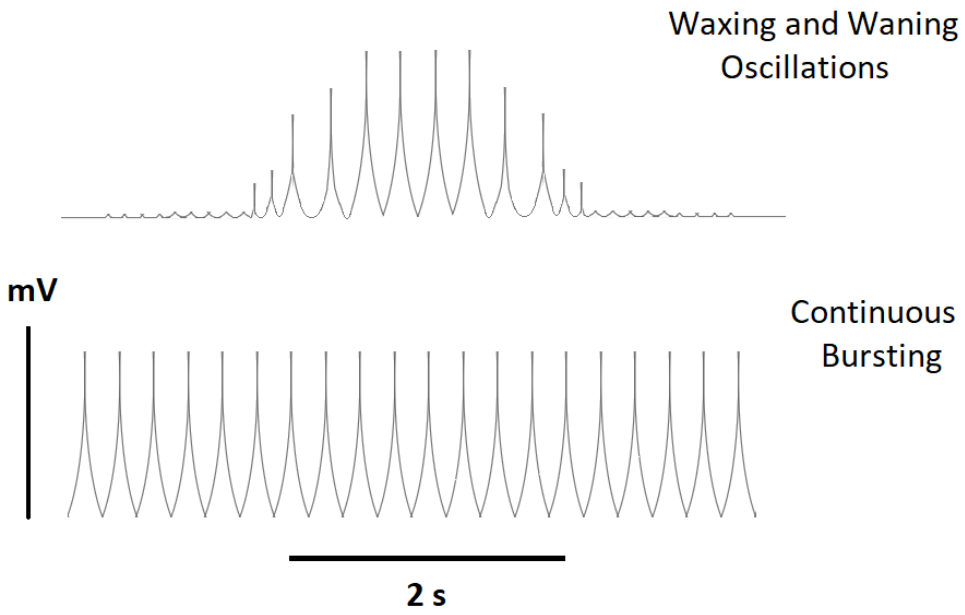

Figure 4.14: Waxing and waning oscillations vs continuous bursting.

Destexhe et al. mention that the mechanisms behind the waxing and waning property are due to the interactions between the I_T and I_H currents. Specifically, they note that when a TC cell repetitively bursts, the I_T current is activated and allows more calcium to enter the cell. I_H is enhanced by intracellular calcium, and depolarizes the cell when enhanced. With the increase in intracellular calcium due to the I_T current, the I_H current depolarizes the cell, and when depolarized enough, the cell ceases further rebound bursting activity and returns to rest. It is in this way that the waxing and waning behaviour is observed [21].

In their model, Destexhe et al. include calcium dynamics in their I_H current, however as mentioned in Section 4.2, there were complications with modelling our I_H current in

this way, and so we chose a non-calcium-dependent model for the current. As such, our model could not produce the waxing and waning oscillations, and instead we observed spontaneous oscillating bursts as our default mode.

However, Destexhe et al. found that the ability of the cell to switch between its waxing and waning, delta oscillations and rest states depended on the conductances of the I_T and I_H currents, and this was a property we wanted to test in our model. Specifically, they showed that with a fixed I_T conductance ($\bar{g}_T$), starting the I_H conductance ($\bar{g}_H$) at $0.005\,\mathrm{mS/cm^2}$ led to delta oscillations (a frequency of 1-4Hz) in the model, while increasing $\bar{g}_H$ to $0.02\,\mathrm{mS/cm^2}$ resulted in waxing and waning oscillations. Further increasing $\bar{g}_H$ to $0.025\,\mathrm{mS/cm^2}$ then led to a rest state with no activity.

For our model, replacing the waxing and waning property with oscillating bursts, we found similar results but with slightly different values of $\bar{g}_H$, as illustrated in Figure 4.15. With our model, holding $\bar{g}_T$ at $2\,\mathrm{mS/cm^2}$ and setting $\bar{g}_H$ to $0.02\,\mathrm{mS/cm^2}$ still resulted in some bursting activity. For the TC cell to reach a rest state, $\bar{g}_H$ had to be increased to around 0.22 to $0.025\,\mathrm{mS/cm^2}$. In terms of the delta oscillations, we also observed this pattern with our TC cell when $\bar{g}_H$ was very small (e.g., 1e-6$\mathrm{mS/cm^2}$).

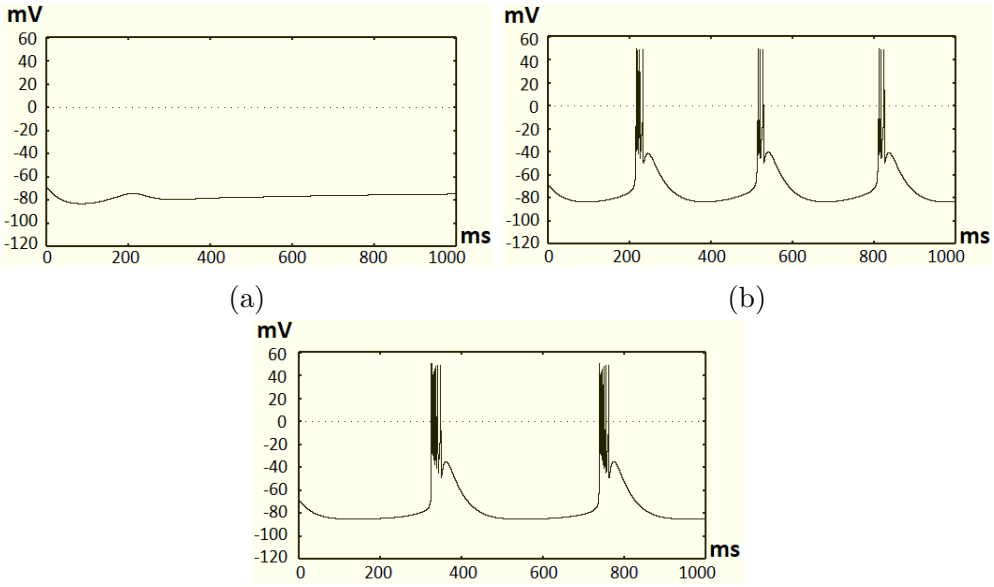

Figure 4.15: Intrinsic bursting properties of TC cells (mV vs ms). I_T conductance ($\bar{g}_T$) was held constant at $2\,\mathrm{mS/cm^2}$, while I_H conductance ($\bar{g}_H$) was varied. (a): $\bar{g}_H = 0.025\,\mathrm{mS/cm^2}$, leading to a rest state. (b): $\bar{g}_H = 0.015\,\mathrm{mS/cm^2}$, leading to oscillatory bursts. (c): $\bar{g}_H$ = 1e-6mS/cm^2, leading to delta oscillations.

The potassium leak current (I_{KL}) was also found to have a strong impact on the cell's ability to produce spontaneous bursting. Originally, these previous tests were conducted with an incorrect I_{KL} conductance value of $0.000\,137\,93\,\mathrm{mS/cm^2}$, rather than $0.013\,793\,\mathrm{mS/cm^2}$, illustrated in Figure 4.16. With this much lower value, the cell was not able to display spontaneous bursting, however, the responses to the depolarizing and hyperpolarizing currents were similar. This result makes sense, as the main role of I_{KL} is to lower the resting potential of the cell. With a smaller I_{KL} conductance, the membrane potential does not become low enough for the I_T current to be activated, and therefore no oscillating bursting occurs.

The other noted difference with our model is that while a typical in vitro guinea pig TC neuron holds a resting membrane potential of $-63\,\mathrm{mV}$ [59], our model appears to reach a lower resting potential closer to $-80\,\mathrm{mV}$. This may also be due to the difference in our I_H equations.

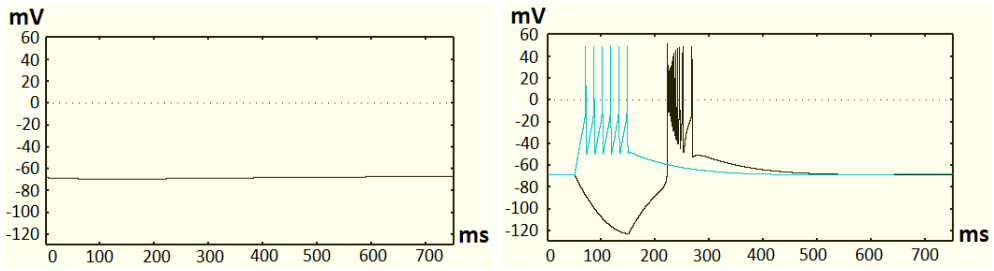

(a) (b)

Figure 4.16: Consequence of incorrect g_{KL} on TC cell (mV vs ms). $g_{KL} = 0.000\,137\,93\,\text{mS/cm}^2$ instead of $g_{KL} = 0.013\,793\,\text{mS/cm}^2$ (a): With no input. (b): With $3\,\mu\text{A/cm}^2$ input (blue trace), and $-1\,\mu\text{A/cm}^2$ input (black trace).

Effect of Each Current

We then analyzed the effects of each current on the model, by again only considering certain currents in the model at a time. For each combination of currents considered, we tested the response of the model in the same way as the RE cell, with 100 ms currents of $3\,\mu\text{A/cm}^2$ and $-1\,\mu\text{A/cm}^2$, applied between 50 ms and 150 ms. Table 4.2 summarizes the results of these tests for each combination of currents considered. The following paragraphs detail the results of these tests, and Figures 4.17 through 4.20 illustrate the results. Again, the results for the full TC model are presented in Table 4.2, however the details and illustrations for these results are given under the *Injected Current* heading, in Section 4.3.2.

For the model with only the passive currents, I_L and I_{KL} (Figure 4.17), the cell responded as expected. Without external stimuli, the cell reached a resting potential of around $-87\,\text{mV}$, and with the depolarizing and hyperpolarizing inputs the membrane potential increased and decreased respectively. When I_{Na} and I_K were added (Figure 4.18), the cell's response at rest and to the hyperpolarizing input were similar to the passive model. Similar to the RE model, the cell produced a train of spikes in response to the depolarizing input, again implying the necessity of the I_{Na} and I_K currents in order to generate action potentials.

With the addition of the I_H current (Figure 4.19), the cell had a resting membrane potential that gradually rose to about $-75\,\text{mV}$ over time. The response to the negative input was that there was a depolarizing sag, where the cell did not hyperpolarize as much as when I_H was not included, and that the cell also returned to the $-75\,\text{mV}$ equilibrium faster than with the positive input. For the model with the I_T current instead of the I_H

Table 4.2: Summary of the Effects of Each Current on the TC Membrane Potential

Figure	**Currents**	**Positive Input**	**Negative Input**
Fig. 4.17	I_L, I_{KL}	Passive rise, then rest	Passive fall, then rest
Fig. 4.18	I_L, I_{KL}, I_{Na}, I_K	Spiking, then rest	Passive fall, then rest
Fig. 4.19	I_L, I_{KL}, I_{Na}, I_K, I_H	Spiking, then rest	Passive fall with depolarizing sag, then rest
Fig. 4.20	I_L, I_{KL}, I_{Na}, I_K, I_T	Spiking, then oscillating bursts	Passive fall, then oscillating bursts
Fig. 4.12	I_L, I_{KL}, I_{Na}, I_K, I_H, I_T	Spiking, then oscillating bursts	Passive fall with depolarizing sag, then a rebound burst and oscillating bursts

current (Figure 4.20), oscillatory bursting occurred without any external stimuli. With the negative input, the cell hyperpolarized and then returned to equilibrium where it started its oscillatory bursts, and with the positive input the cell reacted with a train of spikes, and then eventually returned to resting potential and displayed the same bursting pattern after the input was removed.

These results coincide with the results from McCormick and Huguenard in 1992, where they note a depolarizing sag that occurs after hyperpolarization, as a result of the I_H current [59], as can be seen in Figure 4.19. Our results also coincide with the work done by McCormick and Pape in 1990 [60] and by Soltesz et al. in 1991 [76], which showed that the I_H and I_T currents in TC cells control most of the electrophysiological properties.

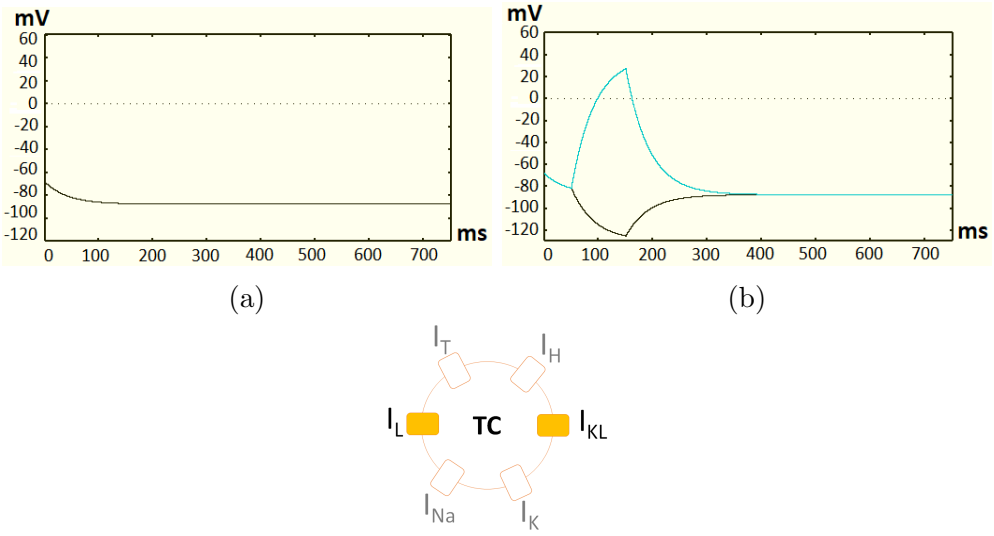

Figure 4.17: Individual TC cell, only I_L and I_{KL} included (mV vs ms). (a): With no input. (b): With $3\,\mu A/cm^2$ input (blue trace) and $-1\,\mu A/cm^2$ input (black trace).

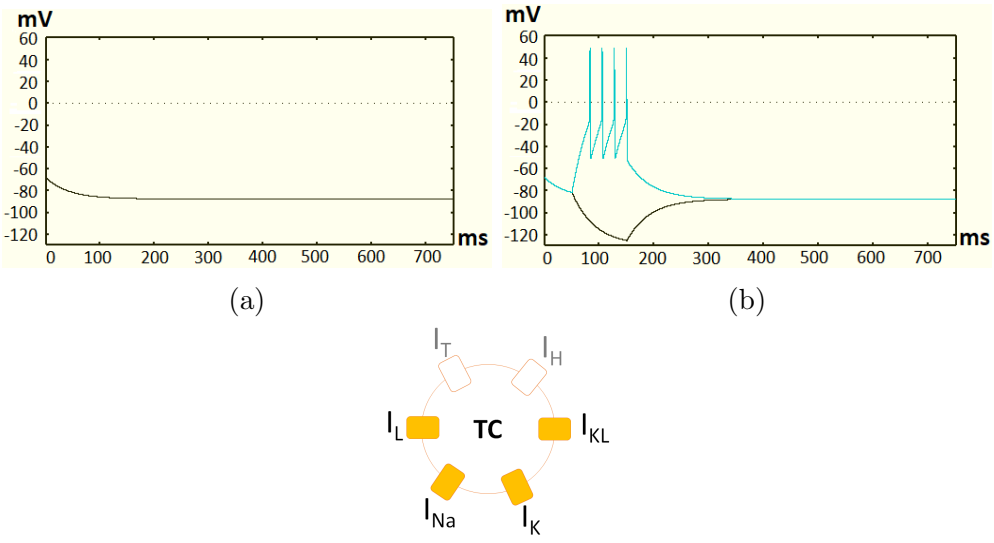

Figure 4.18: Individual TC cell, only I_L, I_{KL}, I_{Na} and I_K included (mV vs ms). (a): With no input. (b): With $3\,\mu A/cm^2$ input (blue trace) and $-1\,\mu A/cm^2$ input (black trace).

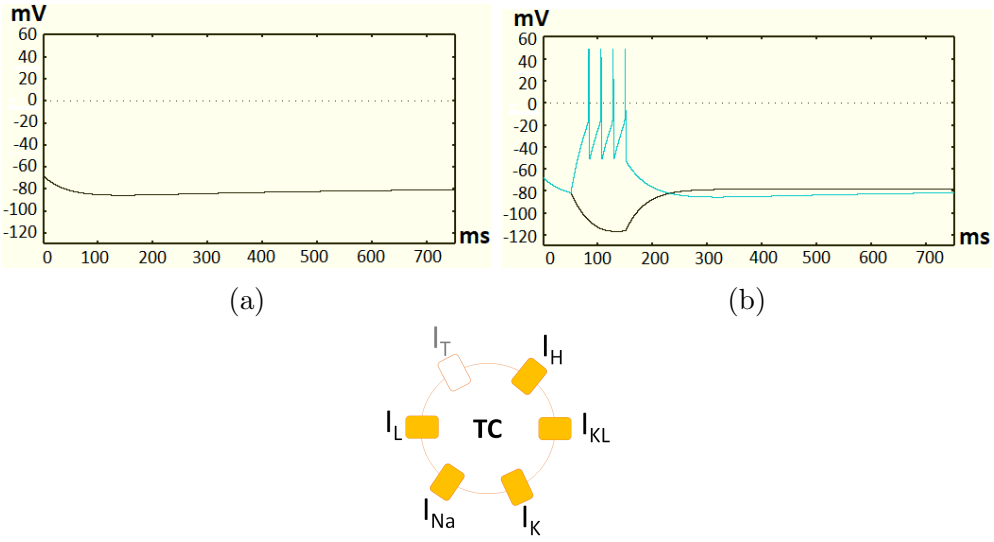

Figure 4.19: Individual TC cell, only I_L, I_{KL}, I_K, I_{Na} and I_H (mV vs ms). (a): With no input. (b): With $3\,\mu A/cm^2$ input (blue trace) and $-1\,\mu A/cm^2$ input (black trace).

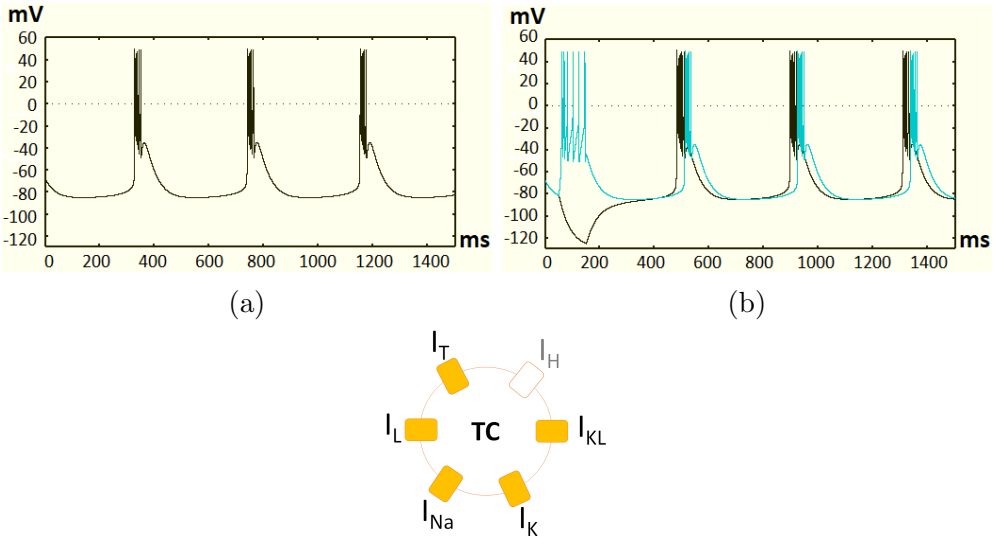

Figure 4.20: Individual TC cell, with only I_L, I_{KL}, I_K, I_{Na} and I_T (mV vs ms). (a): With no input. (b): With $3\,\mu A/cm^2$ input (blue trace) and $-1\,\mu A/cm^2$ input (black trace).

4.4 Separate Network Models

With both our RE and TC models matching the main characteristics of the studied experimental cells, the next step was to set up networks of the RE cells in order to test their network properties. Destexhe et al. analyzed different sized RE networks in their 1994 paper [22], and here we follow their analysis with various two-cell and five-cell network models. For both sized networks, we considered different arrangements for the $GABA_A$ synapses between the cells. This included considering when there was a $GABA_A$ synapse connecting each cell to itself in order to mimic self-inhibition. In our networks, we labelled the RE cells as RE0, RE1, RE2, RE3 and RE4, for convenience.

In their 1996 paper [21], Destexhe et al. did not consider networks of TC cells, and so we did not consider these networks here. This makes sense, as in the full RE-TC network there are no synapses between the TC cells.

4.4.1 RE Cell (2 Cells)

To follow the analysis made by Destexhe et al. in 1994 [22], we first set up two networks of two RE cells connected via $GABA_A$ synapses. Unlike the 1994 model, we included gap junctions between the cells. The first model considers the cells connected to each other without an additional $GABA_A$ synapse to itself, and the second considers the extra self-inhibition for each cell. Here, we included the $I_{K[Ca]}$ and I_{CAN} currents, as Destexhe et al. noted them to be necessary to account for the intrinsic properties of an RE cell network [22].

For the two-cell networks, Destexhe et al. note in their online model [22] that a random current pulse was inserted into each neuron in both networks. Specifically, the inputs had a fixed duration of 200 ms, a random amplitude between 0 and -0.5 (presumably $\mu A/cm^2$), and a random time point of application. The values for the amplitude and the time point of application were generated by a computerized random generator from uniform distributions over the respective ranges. The total $GABA_A$ conductance ($\bar{g}_{GABA_A}$) for one cell in the network was set to 1 µS, and so we used 100 mS/cm^2, as the surface area of our cell is assumed to be 1000 μm^2 ($\frac{1\mu S}{1000\mu m^2} = \frac{100mS}{cm^2}$).

For the network without self-inhibition, the cells displayed alternating multiple bursts, as shown in Figure 4.21, similar to the results of Destexhe et al. in 1994 [22]. These results make sense, as while one cell is bursting it is inhibiting the other cell via the $GABA_A$ synapse, and so once the bursting in the first cell stops, the second cell starts to burst.

This was also noted by Destexhe et al. [22]. For the network with self-inhibition, when only one pulse was input into the network, ($-1\,\mu A/cm^2$ into RE0 between 50 - 150 ms), only a single spike was produced by each cell before both reached and then stayed at resting potential (not pictured). We then input a random pulse into both cells (Figure 4.22), and as a result there was more spiking activity, however there was still no oscillatory bursts. We tried a variety of inputs into the network, each varying in strength, polarization and time point of application, however we could not get the model to produce oscillating activity. We are unsure of why this is the case, however it could be a result of the difference in our $GABA_A$ synapse model. Perhaps modelling the synapse in the same way as Destexhe et al., where the spiking time is tracked, might produce the desired oscillating behaviour in the network.

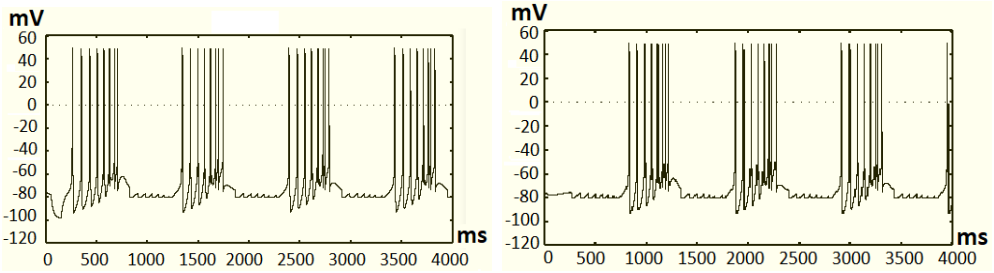

(a) RE Cell 0 (b) RE Cell 1

Figure 4.21: Two connected RE cells *without* self-inhibition (mV vs ms). In both cells $\bar{g}_{GABA_A} = 100\,mS/cm^2$ and $V_0 = -74\,mV$. $-1\,\mu A/cm^2$ input applied to RE0 between 50-150 ms, and no input applied to RE1.

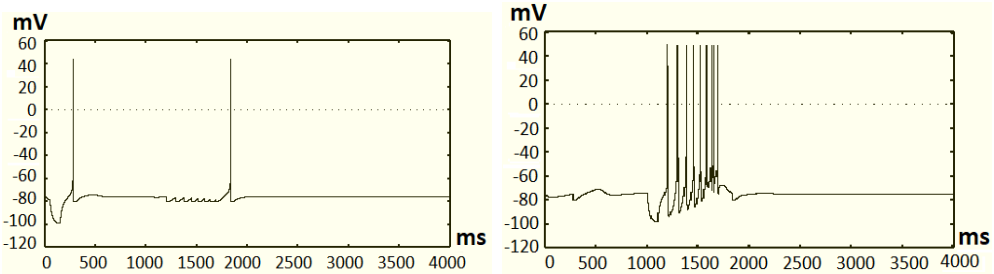

(a) RE Cell 0 (b) RE Cell 1

Figure 4.22: Two connected RE cells *with* self-inhibition (mV vs ms). In both cells $\bar{g}_{GABA_A} = 50\,mS/cm^2$ and $V_0 = -74\,mV$. $-1\,\mu A/cm^2$ input applied to RE0 between 50-150 ms, and $-1\,\mu A/cm^2$ input applied to RE 1 between 1000-1100 ms

4.4.2 RE Cell (5 Cells)

Next, we attempted to recreate the 5-cell network presented by Destexhe et al. in their 1994 paper [22]. As performed by Destexhe et al., we considered four different arrangements for the connections between a ring of five cells, which included: only neighbouring connections; neighbouring connections plus self-inhibition; connections to all other cells excluding itself; and connections to all other cells including itself. For each of these set ups, we tested the response of the network when first injected with a current of $-1\,\mu A/cm^2$ into RE0, between 50 and 150 ms, and then when each cell was injected with a random current pulse of 100 ms and each had a different initial voltage. The total $GABA_A$ conductance ($\bar{g}_{GABA_A}$) for one cell was set to $100\,\mu S/cm^2$, and so we used an equal division of that value depending on how many connections were in the network. Figures 4.23 through 4.30 illustrate these results.

For the network of only connected neighbours, we can see from Figure 4.23 that when RE0 first bursts, it inhibits its neighbours, RE1 and RE4, which both start to burst once RE0 has stopped bursting. As such, RE0, as well as RE1 and RE4 appear to alternate with their bursting. RE2 and RE3 have only a single spike, which makes sense since they are inhibiting each other while they're both bursting, resulting in fewer spikes. In Figure 4.24, with the multiple inputs to the network, the network shows more of an equal spiking pattern between the cells, due to the extra stimulation.

With the self-inhibition included in this network and only one input (Figure 4.25), the cells respond with a single burst rather than a train of spikes and have much less activity, which coincides with the extra inhibition on each cell. With the multiple inputs (Figure 4.26), there is more spiking activity, due to the extra inputs, however there is no clear pattern of oscillations between the cells, as Destexhe et al. presented in their paper [22]. This again could be due to the difference in how we modelled our $GABA_A$ synapses.

When each cell was connected to every other cell except itself, we see very little spiking activity when there is only one input to the network (Figure 4.27), and slightly more activity with multiple inputs (Figure 4.28). Our results do not perfectly match those by Destexhe et al. in 1994 [22], as there is no pattern of oscillations, however we still see the rebound activity from the cells as one bursts, and in some spots less spiking activity due to the extra inhibition from all the cells. This could again be due to our differences with our $GABA_A$ synapses. For the fully connected network (Figures 4.29 and 4.30), we see results similar to the previous case, but with less spiking activity. As there is another factor of inhibition put on each cell, it would make sense to expect fewer spikes. Again, this could be due to the differences in our modelling.

Although our model does not present the exact results of the model produced by Destexhe et al. [22], we have shown that it does include many of the intrinsic properties that are found in RE cell networks. This includes oscillatory bursts in a two-cell network, and rebound bursting due to inhibition. We were not able to resolve why our RE network did not produce the results of Destexhe et al.'s model, however this characteristic was not relevant in our main RE-TC network and so we did not pursue it further.

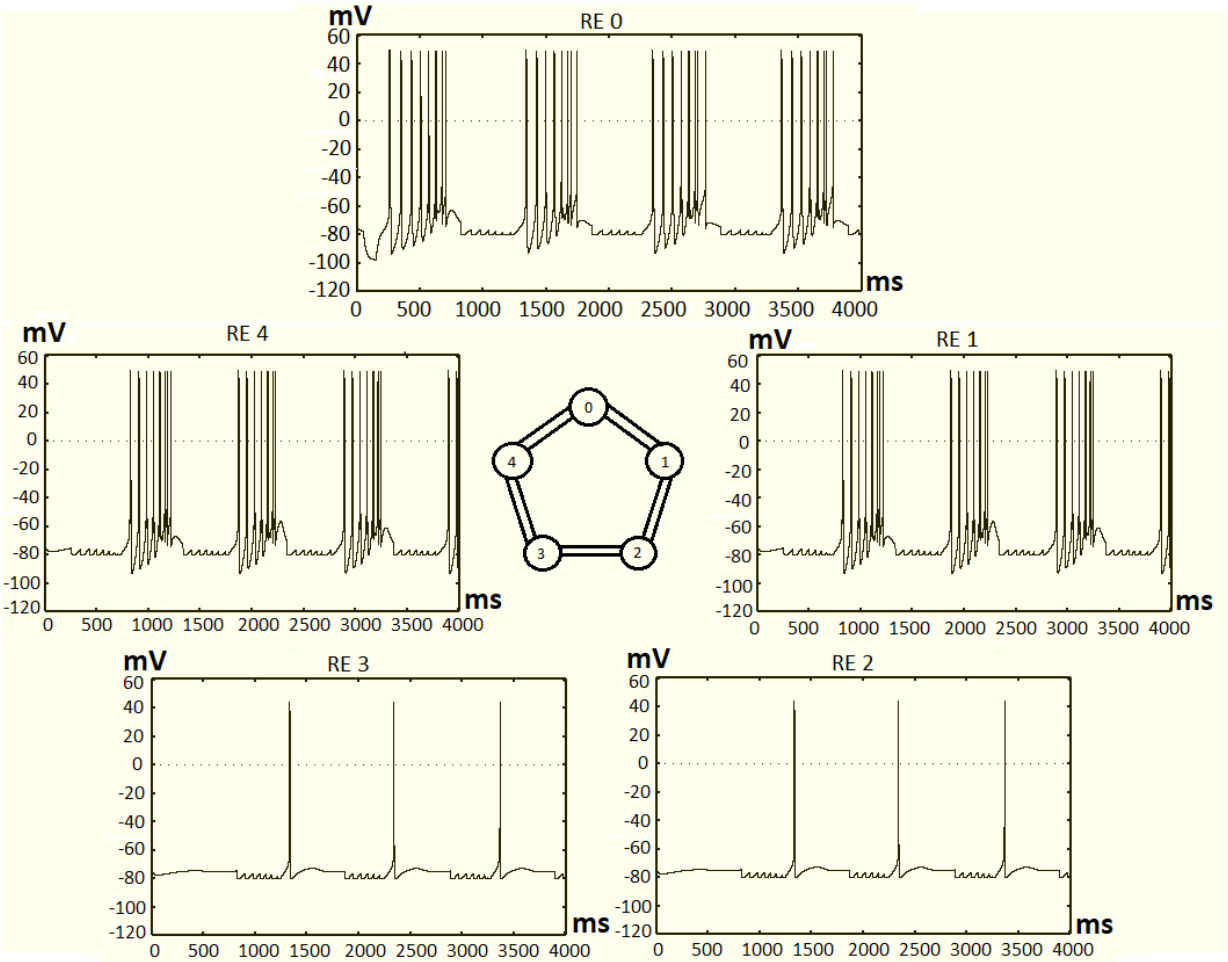

Figure 4.23: Five RE cells, connected via neighbours only (*1 input*) (mV vs ms). In all cells $\bar{g}_{GABA_A} = 50\,\mathrm{mS/cm^2}$ and $V_0 = -74\,\mathrm{mV}$. One input applied to the network; $-1\,\mu\mathrm{A/cm^2}$ to RE0 between 50-150 ms.

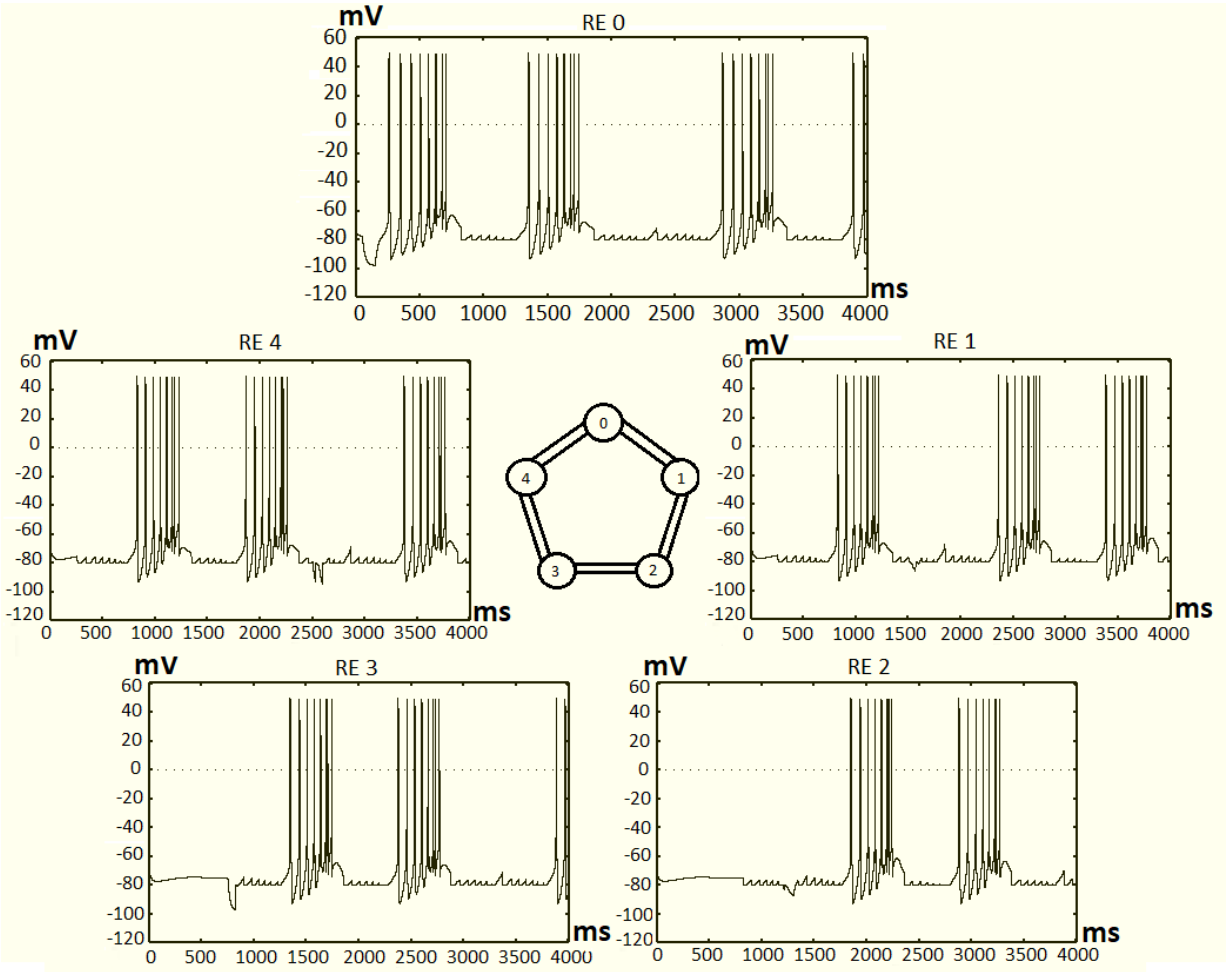

Figure 4.24: Five RE cells, connected via neighbours only (*5 inputs*) (mV vs ms). In all cells $\bar{g}_{GABA_A} = 50\,\mathrm{mS/cm^2}$. *Inputs* ($\mu\mathrm{A/cm^2}$): RE0 = -1 (50-150 ms), RE1 = -0.5 (1500-1600 ms), RE2 = -0.5 (1200-1300 ms), RE3 = -1 (750-850 ms), RE4 = -1 (2500-2600 ms). *Initial Conditions* (mV): RE0 = -74, RE1 = -68, RE2 = -71, RE3 = -70, RE4 = -69.

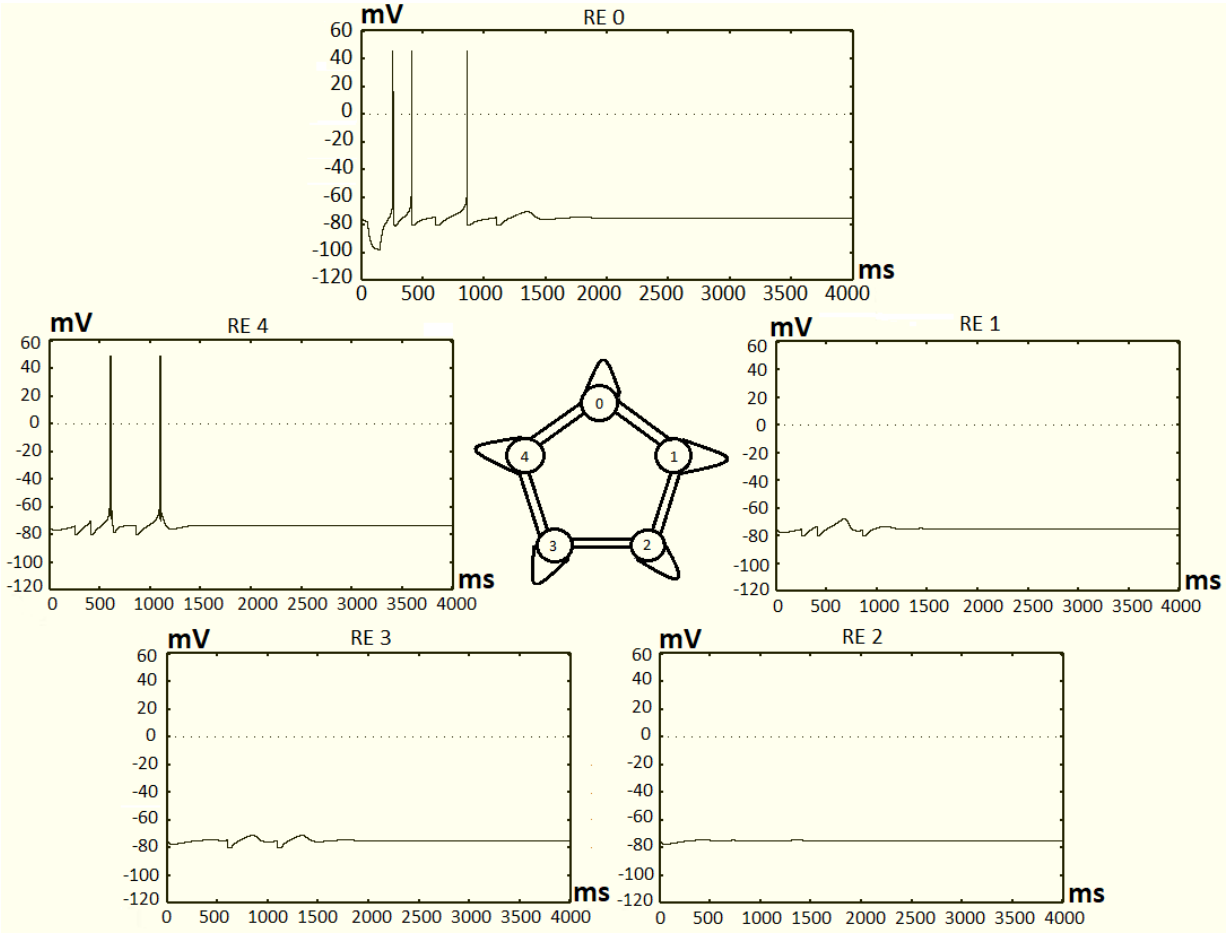

Figure 4.25: Five RE cells, connected via neighbours and *with* self connections (*1 input*) (mV vs ms). In all cells $\bar{g}_{GABA_A} = 33\,\mathrm{mS/cm^2}$ and $V_0 = -74\,\mathrm{mV}$. One input into RE0 of $-1\,\mu\mathrm{A/cm^2}$, between 50-150 ms.

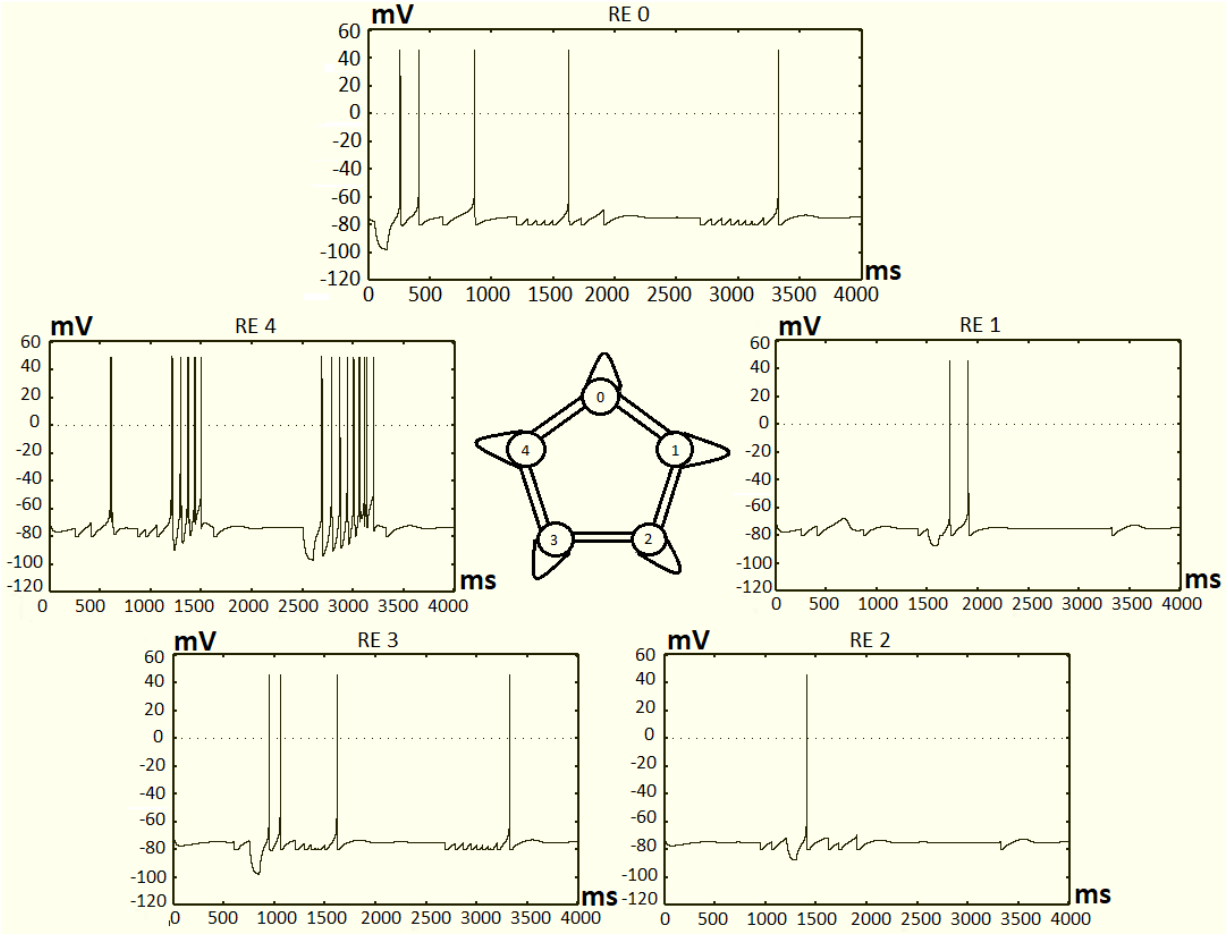

Figure 4.26: Five RE cells, connected via neighbours and *with* self connections (*5 inputs*) (mV vs ms). In all cells $\bar{g}_{GABA_A} = 33\,\mathrm{mS/cm^2}$. *Inputs* ($\mu\mathrm{A/cm^2}$): RE0 = -1 (50-150 ms), RE1 = -0.5 (1500-1600 ms), RE2 = -0.5 (1200-1300 ms), RE3 = -1 (750-850 ms), RE4 = -1 (2500-2600 ms). *Initial Conditions* (mV): RE0 = -74, RE1 = -68, RE2 = -71, RE3 = -70, RE4 = -69.

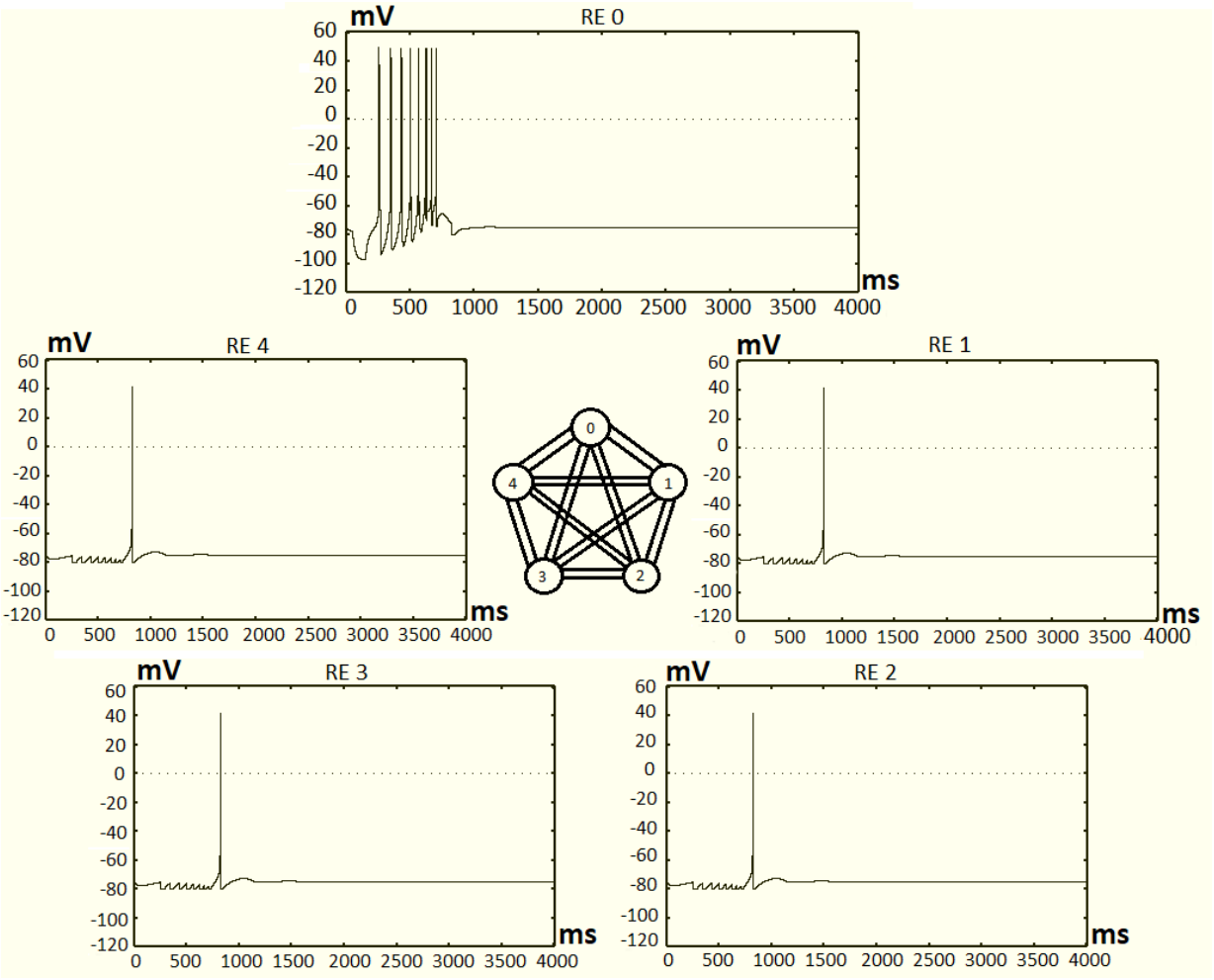

Figure 4.27: Five RE cells all connected *without* self connections (*1 input*) (mV vs ms). In all cells $\bar{g}_{GABA_A} = 25\,\mathrm{mS/cm^2}$ and $V_0 = -74\,\mathrm{mV}$. One input into RE0 of $-1\,\mu\mathrm{A/cm^2}$ between 50-150 ms.

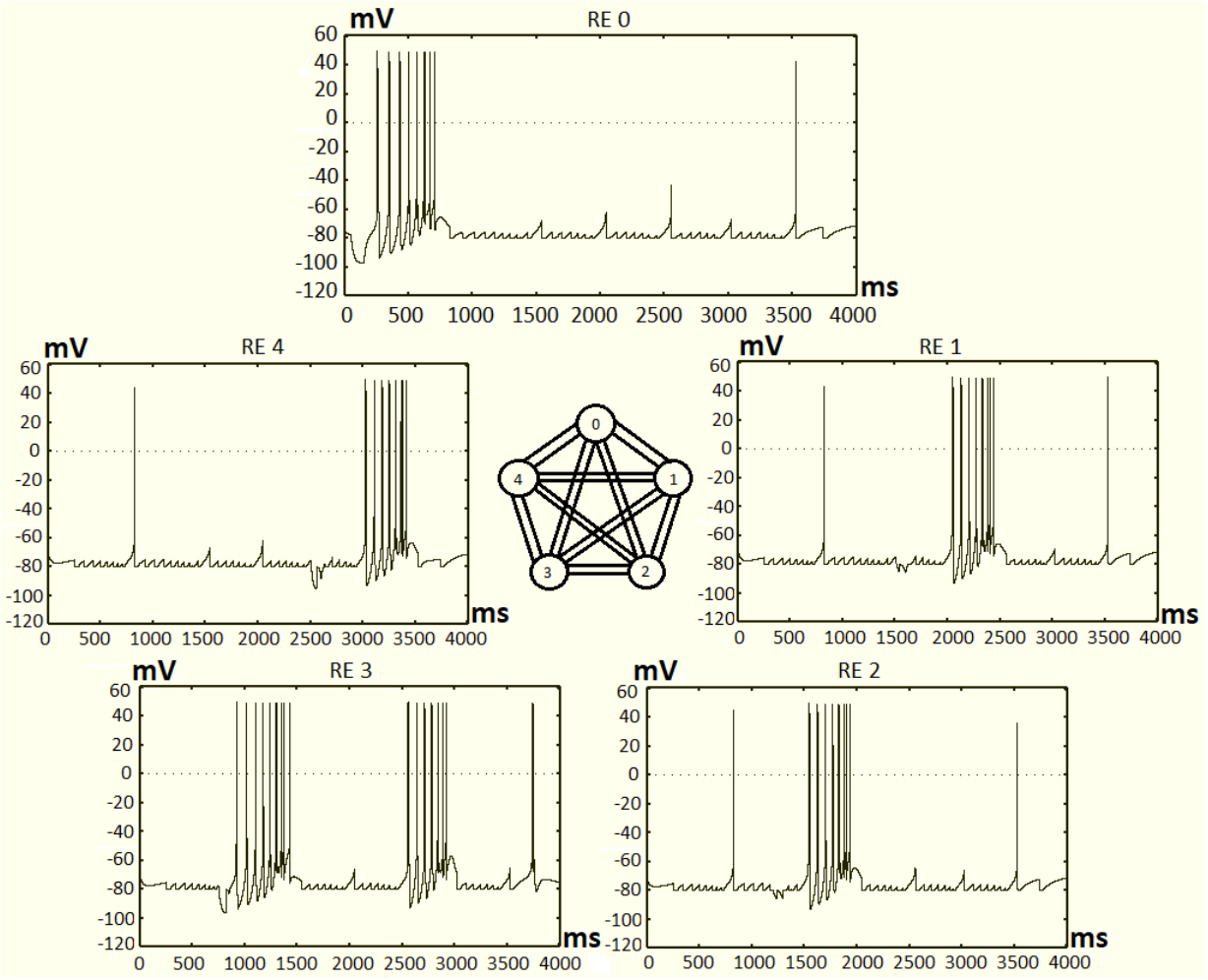

Figure 4.28: Five RE cells all connected *without* self connections (*5 inputs*) (mV vs ms). In all cells $\bar{g}_{GABA_A} = 25\,\mathrm{mS/cm^2}$. *Inputs* ($\mu\mathrm{A/cm^2}$): RE0 = -1 (50-150 ms), RE1 = -0.5 (1500-1600 ms), RE2 = -0.5 (1200-1300 ms), RE3 = -1 (750-850 ms), RE4 = -1 (2500-2600 ms). *Initial Conditions* (mV): RE0 = -74, RE1 = -68, RE2 = -71, RE3 = -70, RE4 = -69.

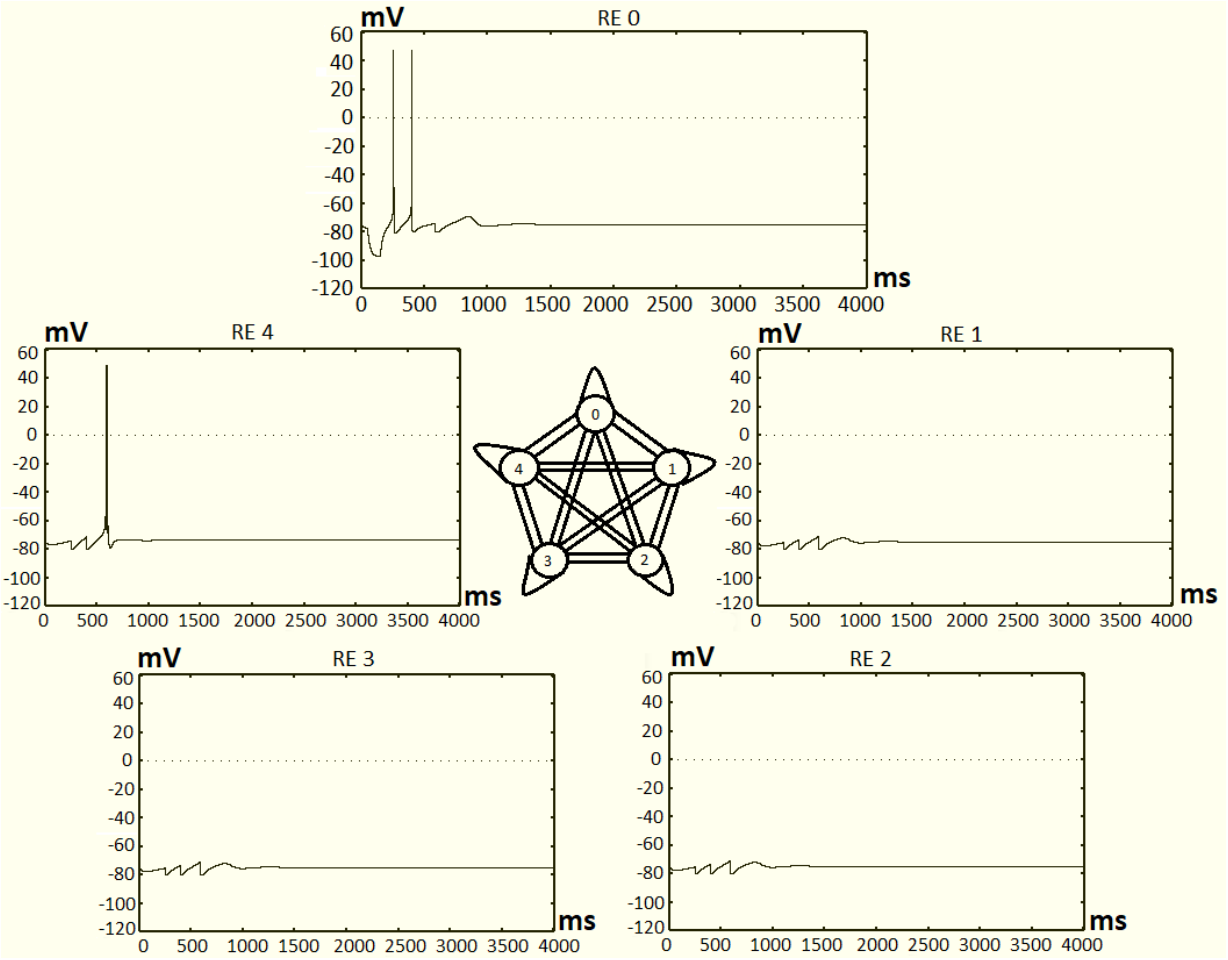

Figure 4.29: Five RE cells, all connected *with* self connections (*1 input*) (mV vs ms). In all cells $\bar{g}_{GABA_A} = 20\,\mathrm{mS/cm^2}$ and all $V_0 = -74\,\mathrm{mV}$. One input into RE0 of $-1\,\mu\mathrm{A/cm^2}$ between 50-150 ms.

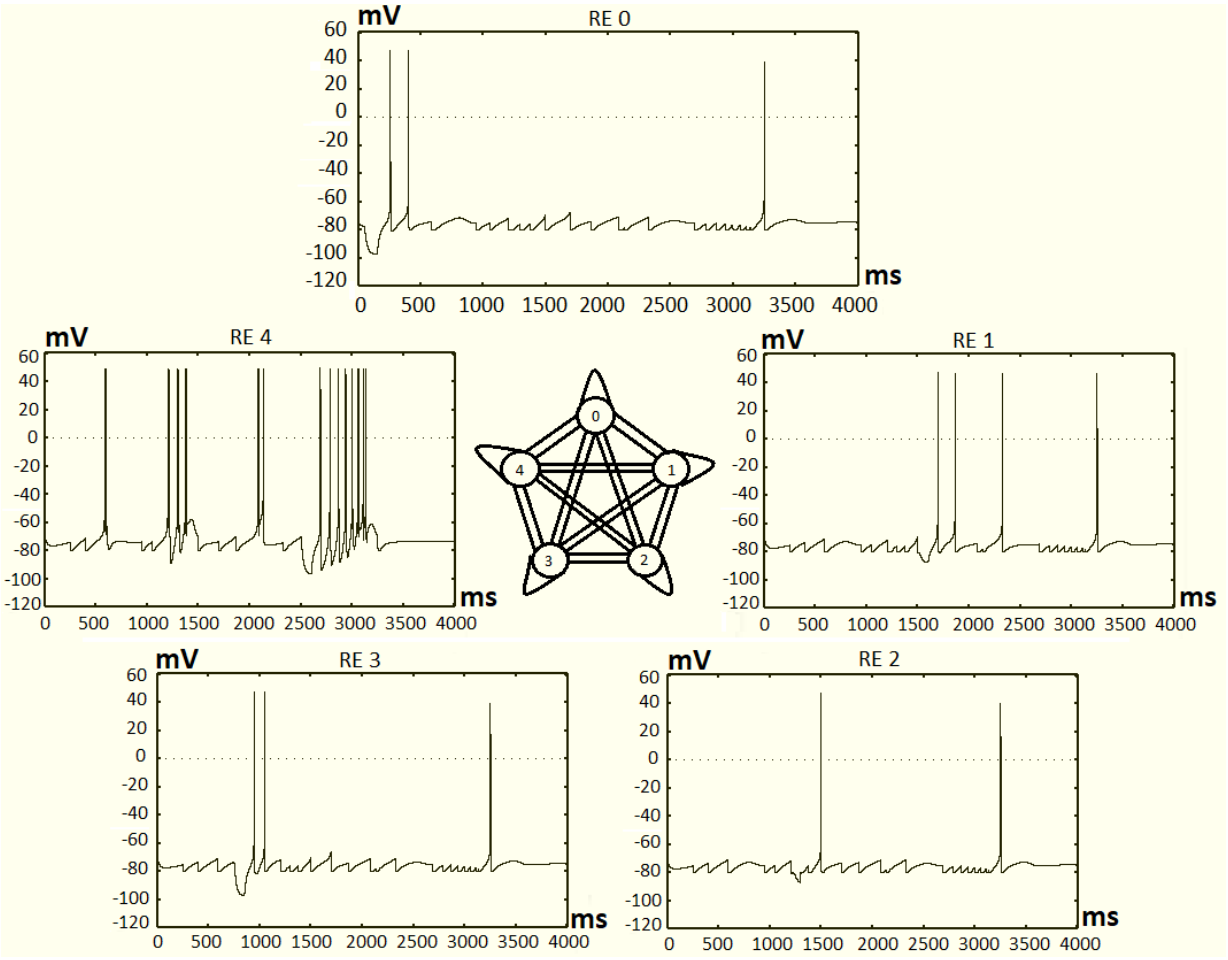

Figure 4.30: Five RE cells, all connected *with* self connections (*5 inputs*) (mV vs ms). In all cells $\bar{g}_{GABA_A} = 20\,\mathrm{mS/cm^2}$. *Inputs* ($\mu\mathrm{A/cm^2}$): RE0 = -1 (50-150 ms), RE1 = -0.5 (1500-1600 ms), RE2 = -0.5 (1200-1300 ms), RE3 = -1 (750-850 ms), RE4 = -1 (2500-2600 ms). *Initial Conditions* (mV): RE0 = -74, RE1 = -68, RE2 = -71, RE3 = -70, RE4 = -69.

4.5 RE-TC Network (4 Cells)

As we are interested in studying the thalamocortical network in relation to childhood absence epilepsy, the next step was to create and set up a network of RE and TC cells.

We were interested in creating a network that could produce mostly alternating bursting between the TC cells, representing normal brain activity, but then switch to synchronous bursting, representing the SWD patterns observed on an EEG during absence seizures. To determine if our network held these properties, as well as the intrinsic properties of a real thalamocortical network, we set up and tested our RE-TC network in the same way as Destexhe et al. in 1996 [21]. Their model, although not directly related to SWDs, produced alternating bursts between the TC cells, which collectively burst at the same frequency as the RE cells. As such, we attempted to replicate their model by creating a four-cell model and implementing the same parameters in order to produce this activity. When this was observed, we injected the network with different pulses and observed the effects of incorporating the $I_{K[Ca]}$ and I_{CAN} currents back into the model.

In terms of why the thalamocortical network initiates this oscillatory behaviour, Destexhe et al. proposed an explanation based on experimental results by Steriade et al. in 1993 [79] and Kim et al. in 1995 [49]. They suggested that these oscillations occur as a result of the reciprocal interactions between the RE and TC cells. Specifically, the bursting in TC cells evokes an AMPA-mediated excitatory response in RE cells as the I_T current is activated, which then evokes a GABA-mediated inhibitory response in the TC cells as the I_T current is deinactivated, creating a cycle of bursting between the two cell types [21]. They also proposed that the hyperpolarization-activated current, I_H, plays a role in the generation and termination of these oscillations [21].

Model Set Up

As mentioned, we set up a four-cell network in the same way as Destexhe et al. in 1996 [21], consisting of two RE cells and two TC cells, illustrated in Figure 4.31. The RE cells are connected to each other via a $GABA_A$ synapse, and receive input from each TC cell via an AMPA synapse. The TC cells are not connected to each other, but receive input from each RE cell via both a $GABA_A$ and $GABA_B$ synapse. Destexhe et al. noted that with a smaller network of only one RE and one TC cell, each burst from the RE cell was followed by a TC burst. However, they note that during spindle oscillations a TC cell should produce a rebound burst after two or three RE bursts. Due to this, and trying to match other intrinsic properties of the thalamocortical network, such as the blocking of GABA synapse conductances not affecting the network's oscillations, Destexhe et al. chose

to work with a four-cell model [21]. For our model, we labelled our RE cells as *RE0* and *RE1*, and our TC cells as *TC0* and *TC1*, for convenience.

For this setup, Desetexhe et al. used the set of parameters listed in Table 4.3 to produce the desired alternating bursting pattern between the TC cells, as displayed in Figure 7 of their 1996 paper [21]. It is assumed that the two TC cells have an initial membrane potential of $-68\,\text{mV}$ and the RE cells have $-74\,\text{mV}$.

However, these exact values did not give us the desired results. In order to achieve the alternating bursting between the TC cells, we found that apart from the synaptic conductances, the two TC cells needed to have the same set of intrinsic parameter values, specifically $\bar{g}_H$ and $\bar{g}_T$. The parameter values and initial conditions that we used for the two TC cells are given in Table 4.4. As a side note, because we included the two surface area conversion factors in our model for the synapses, we could implement the same numerical values given in the paper for the GABA_A, GABA_B and AMPA synapse conductances. For g_{KL}, we converted these as shown below.

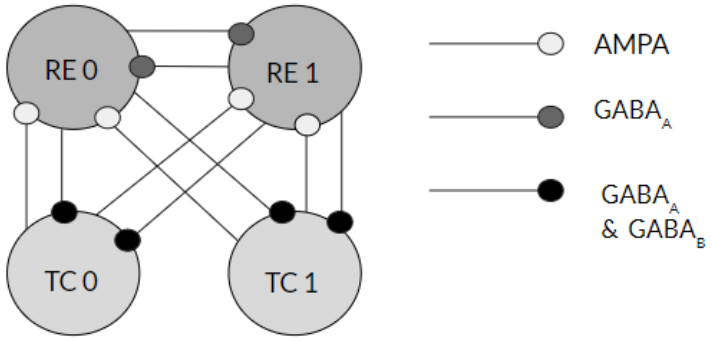

Figure 4.31: RE-TC 4-cell network set up

Table 4.3: Original Parameter Values

	Param	**Value**	**Param**	**Value**
To REs	$\bar{g}_{AMPA}$	$0.2\,\mu\text{S}$	$\bar{g}_{GABA_A}$	$0.2\,\mu\text{S}$
To TCs	$\bar{g}_{GABA_A}$	$0.02\,\mu\text{S}$	$\bar{g}_{GABA_B}$	$0.04\,\mu\text{S}$
TC0	$\bar{g}_H$	$0.025\ \frac{mS}{cm^2}$	g_{KL}	$5\,\text{nS}\ (0.017241375\frac{mS}{cm^2})$
TC1	$\bar{g}_H$	$0.015\ \frac{mS}{cm^2}$	g_{KL}	$3\,\text{nS}\ (0.010344825\frac{mS}{cm^2})$

Table 4.4: Our Altered Parameter Values

	Param	Value	Param	Value	Param	Value
To REs	$\bar{g}_{AMPA}$	$0.2\,\mu S$	$\bar{g}_{GABA_A}$	$0.2\,\mu S$		
To TCs	$\bar{g}_{GABA_A}$	$0.02\,\mu S$	$\bar{g}_{GABA_B}$	$0.04\,\mu S$		
TC0	$\bar{g}_H$	$0.010\ \frac{mS}{cm^2}$	g_{KL}	$4\,nS\ (0.013793\frac{mS}{cm^2})$	IC	$-70\,mV$
TC1	$\bar{g}_H$	$0.010\ \frac{mS}{cm^2}$	g_{KL}	$4\,nS\ (0.013793\frac{mS}{cm^2})$	IC	$-67\,mV$

To expand on this, we varied our model's parameter values and found that when the two TC cells had differing sets of parameter values like the 1996 model, alternate bursting between the TC cells could not be observed (Figure 4.32 (a)). Instead, one TC cell showed continuous bursting at the same frequency as the RE cells, while the other TC cell was inhibited for the entire duration. This was true for multiple combinations of differing $\bar{g}_H$ and g_{KL} parameter values, and regardless of the initial conditions used for the TC cells.

Figure 4.32 (b) shows the results of the model when incorporating the parameter values from Table 4.4. Here, the desired behaviour is achieved, as the TC cells burst opposite each other and collectively burst at the same frequency as the RE cells. Figure 4.32 (c) shows the network when incorporating the parameter values from Table 4.4, but with different initial conditions for the cells' membrane potentials. Here, TC0 is set to $-70\,mV$ and TC1 is set to $-68\,mV$.

Additionally, there is a difference in the shapes of the bursts between our model and the 1996 model. The small inhibited reactions that occur in between alternating bursts in the TC cells, for example, at approximately 1500 ms for TC0 in Figure 4.32 (b), are much larger than the reactions between the alternating bursts in Destexhe et al.'s 1996 paper (See Figure 7, [21]). In Destexhe's model, these *inhibited spikes* are more like small depolarizations, rather than sub-threshold spikes, as observed in our model. However, this could possibly be due to our different I_H model, as the I_H and I_T currents are believed to be responsible for the main bursting properties in TC cells. The main bursts in both our RE and TC cells do appear to have mostly the same shape as those in the 1996 model, and the slight variations could be due to the difference in modelling.

Across each type of bursting pattern in Figure 4.32; alternating, inhibited and synchronous, the frequency of the bursts appears to be consistent, with a response from a TC cell occurring in conjunction with each response of the RE cells, every 500 ms or so. This does not fit the property that Destexhe et al. found with their 1996 model, where the TC cells would respond every two to three bursts from the RE cells, however our model does

display the main intrinsic bursting properties.

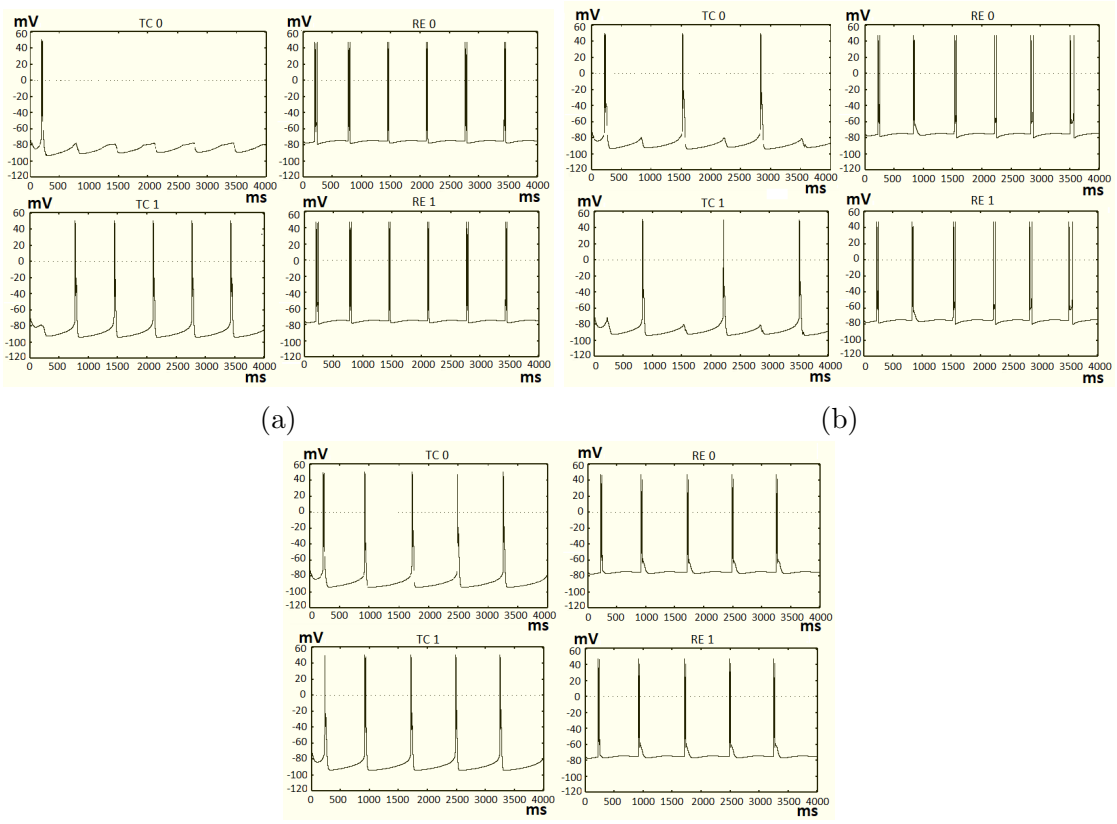

Figure 4.32: Response of 4-cell RE-TC model (reduced) to different parameter values (mV vs ms). (a): Using Table 4.3 parameter values. (b): Using Table 4.4 parameter values. (c): Using Table 4.4 parameter values, with TC0 and TC1 ICs set to $-70\,\text{mV}$ and $-68\,\text{mV}$ (respectively) instead of $-70\,\text{mV}$ and $-67\,\text{mV}$.

Comparing Networks with the Reduced and Full RE Model

To observe the effects of incorporating the $I_{K[Ca]}$ and I_{CAN} currents back into the model, we tested the four-cell network in the same way as above. Implementing the parameter values from Table 4.3 again led to one TC cell constantly bursting while the other was constantly inhibited (Figure 4.33 (a)). Using the parameter values from Table 4.4 also led to one TC cell constantly spiking while the other was constantly inhibited (Figure 4.33 (b)). Using Table 4.4 parameters and changing the TC ICs to $-70\,\text{mV}$ and $-68\,\text{mV}$ as

before, again led to synchronous bursting (Figure 4.33 (c)). These results are very similar to the reduced model (without $I_{K[Ca]}$ and I_{CAN}), except that alternating bursting did not occur.

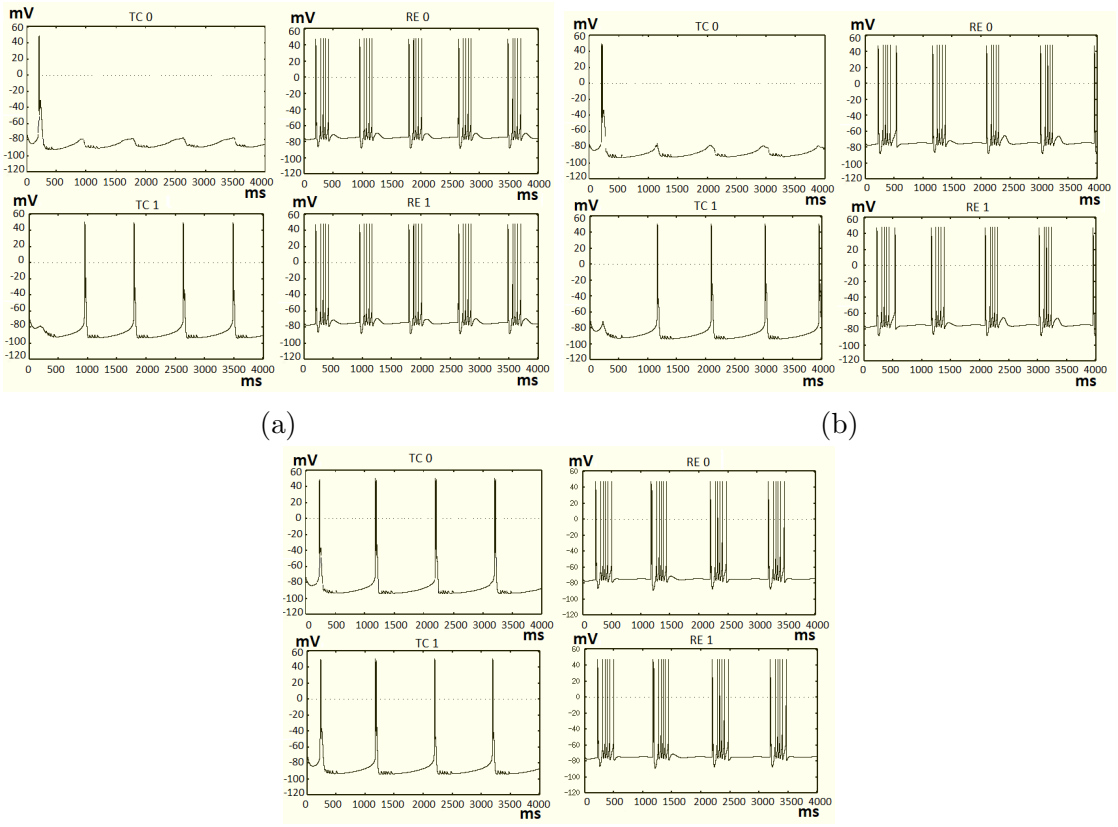

Figure 4.33: Response of 4-cell RE-TC model (full) to different parameter values (mV vs ms). (a): Using Table 4.3 parameter values. (b): Using Table 4.4 parameter values. (c): Using Table 4.4 parameter values, with TC0 and TC1 ICs set to $-70\,\text{mV}$ and $-68\,\text{mV}$ (respectively) instead of $-70\,\text{mV}$ and $-67\,\text{mV}$.

With this model, there was also a difference in the shape of the bursts by the RE cells, when compared to the network with the reduced RE model. Figure 4.34 gives a side-by-side comparison of an RE and TC cell from Figure 4.32 (c) and Figure 4.33 (c), as well as a zoom of a single burst from both the RE and TC cells in each of these network simulations. From this comparison, we can see that unlike the single burst from the reduced RE network, the full RE network produces a burst followed by a train of spikes. These extra spikes lead to

extra inhibited responses in the TC cells, whereas in the reduced RE network there was only a single response from the TC cells. As the $I_{K[Ca]}$ and I_{CAN} are responsible for AHPs and ADPs in RE cells [22], this extra after-bursting activity is understandable.

It is also noted that for the network with the reduced RE model, the bursting frequency was greater than for the network with the full RE model. Specifically, per 4000 ms there were 5-6 bursts by each of the RE and TC cells in the reduced RE network, whereas the full RE network had 4 bursts by each of the cells. This makes sense as there is more spiking activity occurring after each burst in the RE cells of the full RE network.

To further compare the full and reduced models, with and without $I_{K[Ca]}$ and I_{CAN} respectively, we observed the response of each model when implementing various pairs of ICs for the TC cells, and various current inputs into one TC cell between 50ms to 150ms. Specifically, the pairs of TC ICs considered were: -68,-68; -67,-71; -67,-70; -66,-70; and -68,-66 (mV). The various input strengths were: -1, -0.5, 0, 0.5, and 1 ($\mu A/cm^2$). We set g_{KL} to $0.013\,793\,mS/cm^2$ and $\bar{g}_H$ to $0.01\,mS/cm^2$ in both TC cells, and used the same synapse parameters from Tables 4.3 and 4.4. Table 4.5 organizes the results.

Table 4.5: Comparing the Reduced and Full Models

	Reduced Model	**Full Model**
No Input	Alternating bursting (with specific ICs), otherwise synchronous bursting.	One cell bursts while other is inhibited (with specific ICs), otherwise synchronous bursting.
Negative Input	Synchronous bursting.	Synchronous bursting.
Positive Input	Alternating bursting (with specific ICs), otherwise one cell bursts while other is inhibited.	One cell bursts while other is inhibited.

Based on these tests, the main difference in bursting activity between the two cells appears to be that the alternating bursting in the reduced model is replaced by the inhibition of one TC cell in the full model. Regardless, we continued to use the reduced model to coincide with the model and results produced by Destexhe et al. in 1996 [21].

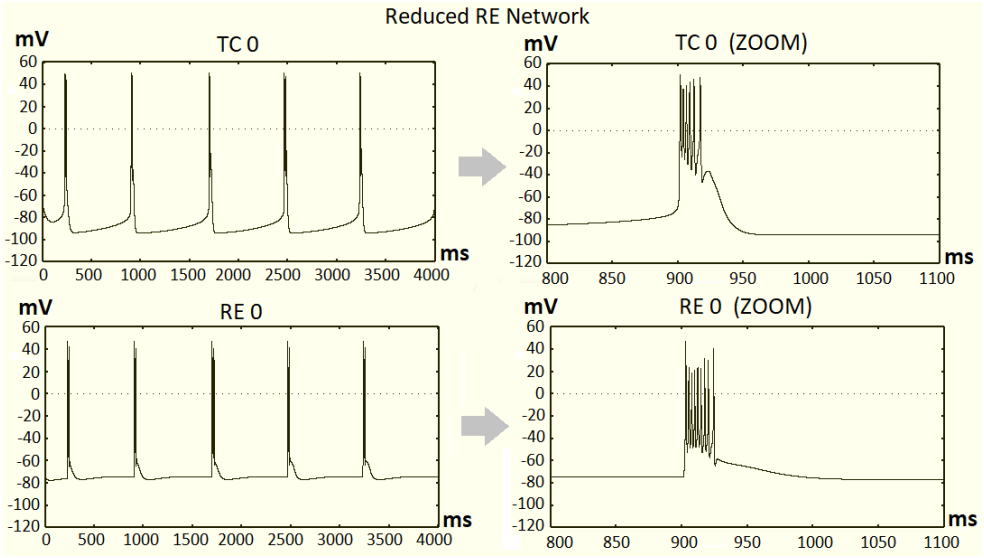

(a)

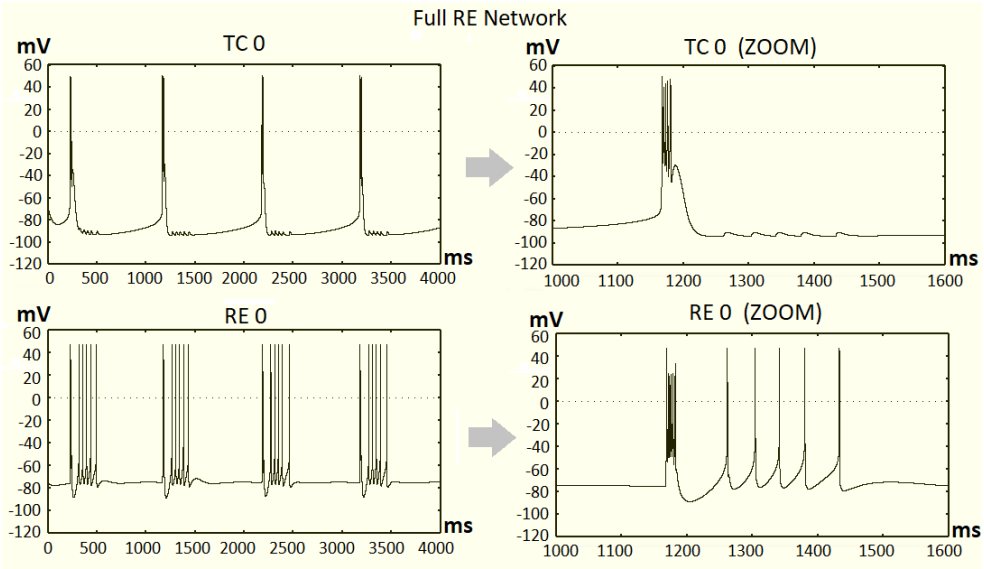

(b)

Figure 4.34: Comparison of RE bursting in the network with the reduced RE model, and the network with the full RE model (mV vs ms). (a): Two cells from Figure 4.32 (c) (reduced RE model). (b): Two cells from Figure 4.33 (c) (full RE model).

Effects of Initial Conditions on the Network

One thing we noticed with our RE-TC network is that the occurrence of either alternating or synchronous bursting between the TC cells is largely dependent on the initial conditions (ICs) that the membrane potential is set to in each TC cell. For example, as shown in Figure 4.32 (a) and (c), changing only the initial conditions from $-70\,\text{mV}$ and $-67\,\text{mV}$ to $-70\,\text{mV}$ and $-68\,\text{mV}$ led to synchronous bursting as opposed to alternating bursting.

To better understand this relationship between the type of bursting and the ICs of the TC cells, we tested the network for each combination of TC ICs between $-60\,\text{mV}$ and $-70\,\text{mV}$, as these are typical resting membrane potentials of TC cells. From the results shown in Figure 4.35, where A represents alternating bursting and S represents synchronous bursting, it appears that when the ICs are similar to each other synchronous bursting occurs between the TC cells, whereas with very different ICs alternating bursting happens. For example, the IC pair of $-66\,\text{mV}$ and $-65\,\text{mV}$ lead to synchronous bursting, while $-60\,\text{mV}$ and $-70\,\text{mV}$ lead to alternating bursting.

This is an interesting result, as it implies the synchronous bursting pattern in our model is reliant on the present membrane potential in TC cells. This makes sense, as during synchronous bursting the cells are producing the same behaviour, i.e., giving the same responses at the same time. So, with ICs that are more similar, the cells are more likely to produce this synchronous bursting.

To test this idea further, we examined the model in the following way. For various pairs of ICs that were known to lead to either alternating or synchronous bursting, we injected current pulses of various strengths into TC0 after 3000 ms, in order to see whether the network could switch behaviour. A portion of the results are shown in Table 4.6.

The general trend appeared to be that if the cell started with synchronous bursting, then after the input at 3000 ms, the behaviour switched to one TC cell being inhibited. If the network started with alternating bursting between the TC cells, then typically it would remain with this pattern, with a few exceptions occurring with a $1\,\mu\text{A/cm}^2$ input where it would switch to TC1 being inhibited. It is also noted that the burst frequency observed during each of these simulations were similar, with two to three bursts occurring per 1000 ms. This implies that temporary inputs to change the membrane potential of the model's cells can cause one of the TC cells to stop bursting, however it doesn't affect the network's ability to switch between alternating and synchronous bursting.

Overall, observing this trend with the initial conditions, and especially the results from Figure 4.35, would allow us to compare the effects of possible CAE factors on our network behaviour. Specifically, we can use these results to see if different factors, such as the

CACNA1H mutation, might increase or decrease the prevalence of synchronous bursting in the network. This, along with other tests, will be discussed in the next chapter.

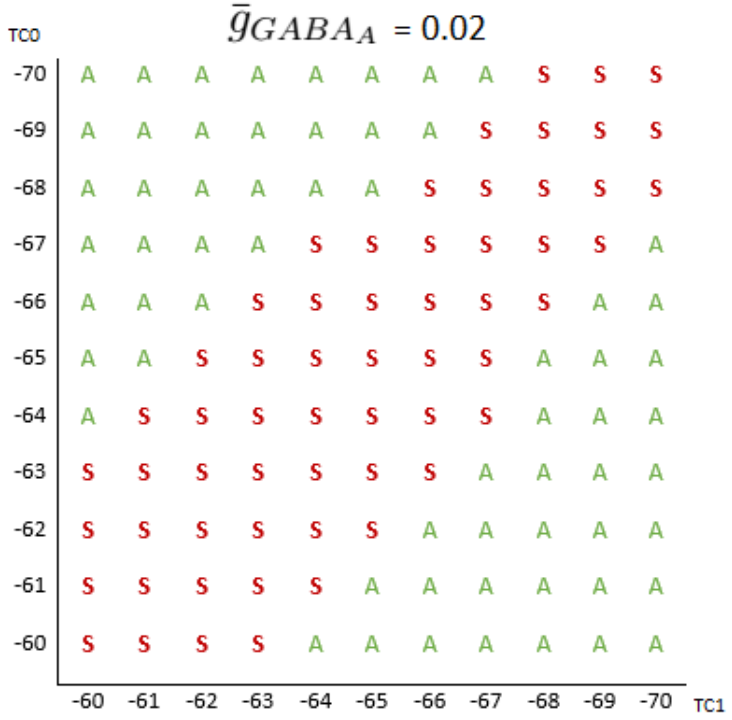

Figure 4.35: Response of RE-TC model to variations in TC initial conditions. *A* represents alternating bursting and *S* represents synchronous bursting between the TC cells.

Table 4.6: Effects of Various Temporary Inputs (3000 ms to 3100 ms) on the Occurrence of Alternating or Synchronous Bursting

TC0 & TC1 ICs	**Response Before Input**	**Response After Input**
TC0: $-1\,\mu A/cm^2$		
-68, -68	Synchronous	TC1 inhibited
-67, -70	Alternating	Alternating
-66, -70	Alternating	Alternating
-68, -66	Synchronous	TC1 inhibited
TC0: $-0.5\,\mu A/cm^2$		
-68, -68	Synchronous	TC1 inhibited
-67, -70	Alternating	Alternating
-66, -70	Alternating	Alternating
-68, -66	Synchronous	TC1 inhibited
TC0: $0.5\,\mu A/cm^2$		
-68, -68	Synchronous	TC1 inhibited
-67, -70	Alternating	Alternating
-66, -70	Alternating	Alternating
-68, -66	Synchronous	TC1 inhibited
TC0: $1\,\mu A/cm^2$		
-68, -68	Synchronous	TC1 inhibited
-67, -70	Alternating	TC1 inhibited
-66, -70	Alternating	TC1 inhibited
-68, -66	Synchronous	TC1 inhibited

Chapter 5

Model Application to Childhood Absence Epilepsy

With our RE-TC thalamic network developed, we then turned our attention to using this model to study possible causes and factors behind childhood absence epilepsy. In this section, we first consider the effects of the $GABA_A$ synaptic conductances on the occurrence of SWD spiking patterns, by altering the value of $\bar{g}_{GABA_A}$ in the synapse models going to the TC cells. We then look at the effects of the *CACNA1H* gene defect on the network, by altering the time constant of inactivation equation, $\tau_H(V)$ in our low-threshold Ca^{2+} currents (I_T) of the RE cells. We conclude with an analysis of the effects of the RE's I_T conductance on the network, by altering the g_T values in the RE cell model.

5.1 $GABA_A$

As discussed in Section 3.2, the effects of a decrease in function of the $GABA_A$ synapses are believed to hold a role in the generation of the slow wave discharges observed in absence epilepsies. Specifically, in 2018 Knox et al. showed that with decreased cortical $GABA_A$ conductances, and an increased I_T conductance, spindle oscillations could be changed to oscillations of slow wave discharges [50]. Before this, in 2011 Crunelli et al. also suggested that the transition to spike and wave discharges in the thalamus/thalamocortical network may be due to a decreased function in $GABA_A$ receptors [12]. Further, studies by Maljevic et al. in 2006 suggested that a genetic mutation in the α_1 subunit of the $GABA_A$ receptor,

found in mouse models of absence epilepsies, may lead to a decrease in $GABA_A$ conductance [58].

With this being said, we decided to test the effects of the $GABA_A$ currents going from the RE cells to the TC cells, on the behaviour of our network. For each value of the TC's $GABA_A$ conductance ($\bar{g}_{GABA_A}$ = 0.02, 0.04, 0.06 and 0.08), we tested the network in the same way as when testing the ICs in Section 4.5; by observing the response of the network for each combination of ICs between $-60\,\text{mV}$ and $-70\,\text{mV}$. In doing this, we were able to produce visual representations of how often synchronous bursting occurred in comparison to alternating bursting, and compare the prevalence of the synchronous bursting across the different values of $\bar{g}_{GABA_A}$.

Figure 5.1 shows the results of this, where A again represents alternating bursting in the network, S represents synchronous bursting, and D represents the cases where one cell is inhibited while the other is bursting. As shown in Figure 5.1, and listed in Table 5.1, the general trend appears to be that as $\bar{g}_{GABA_A}$ is decreased from 0.08 through to 0.02, the prevalence of synchronous bursting increases, with the exception being at $\bar{g}_{GABA_A}$ = 0.06. For this specific value, Figure 5.1 shows that for IC combinations closer to -70mV, alternating bursting is more prevalent than with $\bar{g}_{GABA_A} = 0.08$, however for combinations around $-65\,\text{mV}$ and lower, the original trend still holds. As it is the synchronous bursting in the network that corresponds to SWDs on an EEG, our results imply that the $GABA_A$ synapses may have an effect on the generation of childhood absence epilepsy, coinciding with the results discussed above. Specifically, that with a lower $GABA_A$ conductance in a network, SWDs may be more prevalent.

As mentioned earlier, the $GABA_A$ synapses are inhibitory, with the RE cells in the network inhibiting the TC cells. A decrease in the synapse conductance and a resulting decrease in function implies a possible reduced ability to inhibit the TC cells. With less inhibition, the TC cells could spike more freely, resulting in synchronous bursting where both TC cells spike at the same frequency as the RE cells, as opposed to every second spike being inhibited in the alternating bursting. As such, our results here make sense.

Table 5.1: Percentage of Synchronous Bursting Cases w.r.t. $\bar{g}_{GABA_A}$. *Each percentage is based on the 121-simulation tests from Figure 5.1.*

$\bar{g}_{GABA_A}$ (µS)			
0.02	**0.04**	**0.06**	**0.08**
48.8%	37.2%	25.6%	30.6%

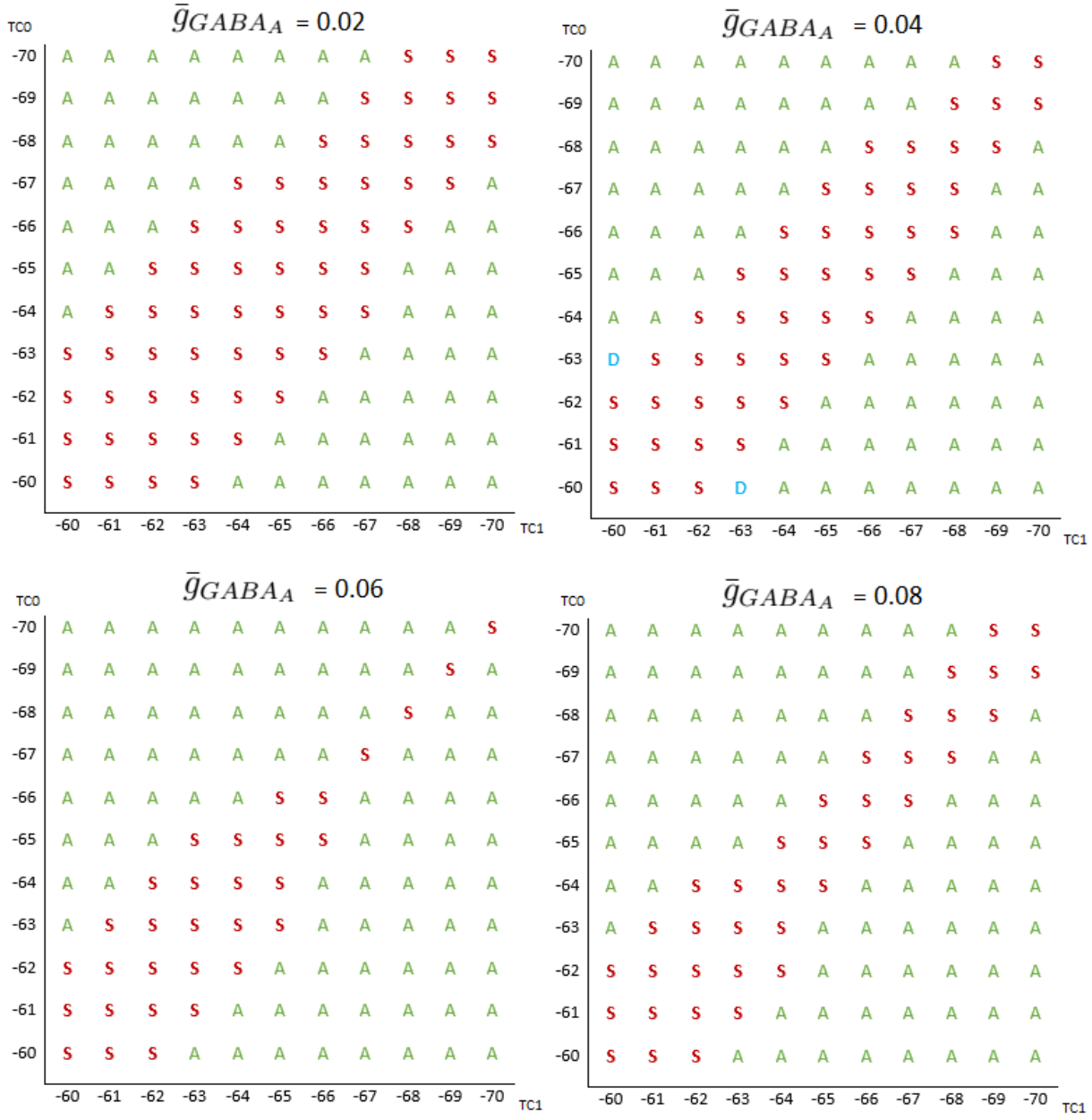

Figure 5.1: Response of RE-TC model to variations in $\bar{g}_{GABA_A}$ values and TC initial conditions. *A* represents alternating bursting and *S* represents synchronous bursting between the TC cells. *D* represents one TC cell bursting while the other TC cell is inhibited.

5.2 *CACNA1H* Mutation

Next, we looked at the effects of a gene mutation that is believed to be one of the multiple genetic factors involved in childhood absence epilepsy. Specifically, we expanded on results from Powell et al. in 2009 [70], which studied the relationship between a mutation in the T-type Ca^{2+} channel gene, *CACNA1H* (or $Ca_v3.2$), and the occurrence of absence seizures in GAERS. For us, in order to test the effects of this genetic defect on our network model, we derived an appropriate alteration of an inactivation time constant parameter in our network that would mimic the effects of the *CACNA1H* mutation in GAERS, and implemented it in both an individual RE cell as well as our RE-TC network.

To justify why they targeted the *CACNA1H* gene in their 2009 paper, Powell et al. reference a number of studies that have implied the importance of T-type Ca^{2+} channels in absence epilepsies. Specifically, they point to work by Tsakiridou et al. in 1995 [84], and Talley et al. in 2000 [81], which showed that in the thalamic reticular nucleus of GAERS, there is an increase in T-type Ca^{2+} channel function, as well as in the expression of mRNA for the $Ca_v3.2$ gene. Also, they reference work by Chen et al. in 2003 [8], Liang et al. in 2006 [55] and 2007 [56], and Heron et al. in 2007 [37], which showed that mutations in the *CACNA1H* gene were found in patients with juvenile absence epilepsy as well as childhood absence epilepsy.

In terms of the *CACNA1H* mutation itself, Powell et al. describe it as a homozygous, missense mutation in GAERS, occurring in exon 24 of the *CACNA1H* gene [70]. Without going into too much detail, this means that a change in a single nucleotide base, in this case from guanine (G) to cytosine (C) [70], occurs at a specific coding location on both copies of the gene, changing the compositional structure of the gene. From their experimental studies on GAERS, Powell et al. found a number of results implicating a connection between absence seizures and this mutation. Specifically, they found that the number of rats experiencing seizures was greater for the group of rats with the mutation (*gcm*) than for the group without the mutation (*control*), and that the *gcm* rats spent more time in seizure activity than the *control* rats. Further, they found that the *gcm* rats had a much shorter time period between seizures than the *control* rats, and that the number of seizures occurring was greater for the *gcm* rats than for the *control* rats [70].

To model this mutation in our network, we used another part of Powell et al.'s study which used *in vitro* testing to observe the effects of the mutation on the $Ca_v3.2$ channels in human embryonic kidney cells. These tests found that the channels with the mutation held a much faster recovery from inactivation rate than the channels without the mutation. The specific values given by Powell et al. were 745.0 ± 32.2 for the *control* channels, compared

with 436.8 ± 37.6 for the *gcm* channels, with the units assumed to be in ms. [70].

Although this is limited data, we used this difference of 42% to alter our inactivation time constant equation, $\tau_H(V)$, in the low-threshold Ca^{2+} currents (I_T) of the RE cells, to mimic this increased rate. In our model, the inactivation and recovery from inactivation are both represented by the variable, h (see Equations 4.3 and 4.5). As such, the appropriate time constant to modify was the $\tau_H(V)$ equation (Equation 4.9). We used the computed value of τ_H(V) at -110 mV as a comparison point, and came up with an altered τ_H equation that would result in values 58% of the original equation. This was achieved by replacing the 0.27 coefficient in the original equation (Equation 5.1), with 0.1335 in the new equation (Equation 5.2). We also created a further-altered τ_H equation to give values 33% of the original, and this was achieved with a coefficient of 0.049, as shown in Equation 5.3. Figure 5.2 illustrates the curves for the three τ_H equations. In our model, we set the altered coefficient as a parameter, gg, in order to simplify comparing the three equations.

$$\tau_h(V) = 22.7 + \frac{0.27}{\exp[\frac{V+48}{4}] + \exp[\frac{-(V+407)}{50}]} \tag{5.1}$$

$$\tau_h(V) = 22.7 + \frac{0.1335}{\exp[\frac{V+48}{4}] + \exp[\frac{-(V+407)}{50}]} \tag{5.2}$$

$$\tau_h(V) = 22.7 + \frac{0.049}{\exp[\frac{V+48}{4}] + \exp[\frac{-(V+407)}{50}]} \tag{5.3}$$

We first tested the effects of these altered τ_H equations on the individual RE cell by implementing a short current pulse of $-1\,\mu A/cm^2$ and $1\,\mu A/cm^2$ into the reduced model between 50 and 150 ms, for each of the three altered τ_H equations. The results of comparing the original τ_H equation (gg=0.27) and the 58% τ_H equation (gg=0.1335) are shown in Figure 5.3. When implementing the 58% τ_H equation, the model reacted slightly quicker to the stimuli than with the original τ_H equation. With the negative input, the model also returned to rest quicker than it did with the original τ_H equation. For the 33% τ_H equation, the results were almost identical, and so they are not shown.

We then tested the full model, with the $I_{K[Ca]}$ and I_{CAN} currents, in the same way, with the results shown in Figure 5.4. The main difference here was that with the negative input, the RE cell took almost twice as long to cease bursting with the 58% τ_H equation than with the original. However, in both the reduced and full models, the cells responded quicker to the inputs when the *CACNA1H* mutation was implemented.

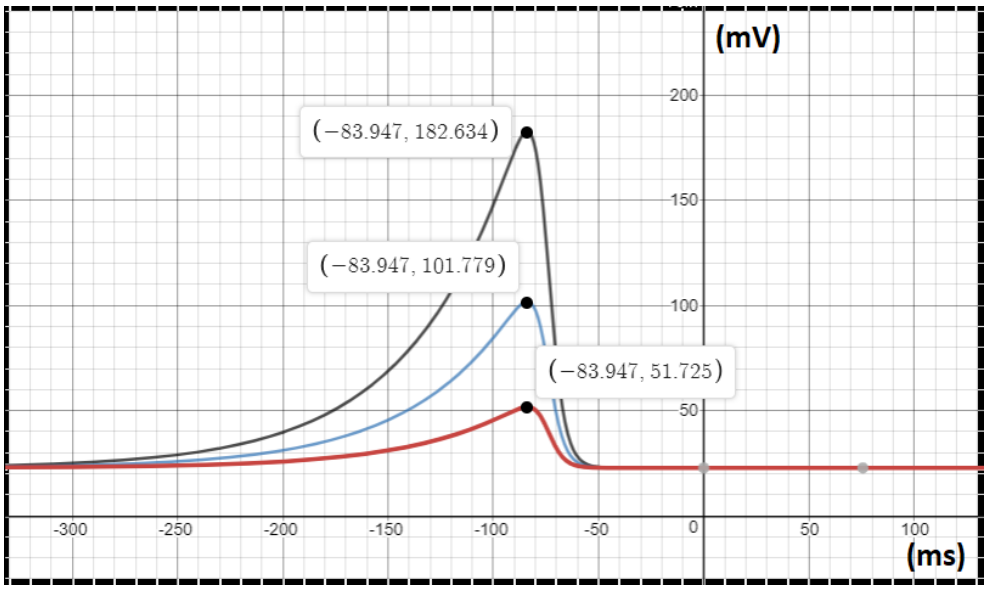

Figure 5.2: Inactivation time constant equations (τ_H) for I_T in RE cell. Black: original equation (gg = 0.27), Blue: 58% equation (gg = 0.1335). Red: 33% equation (gg = 0.049) (*graph created using Desmos.com.*)

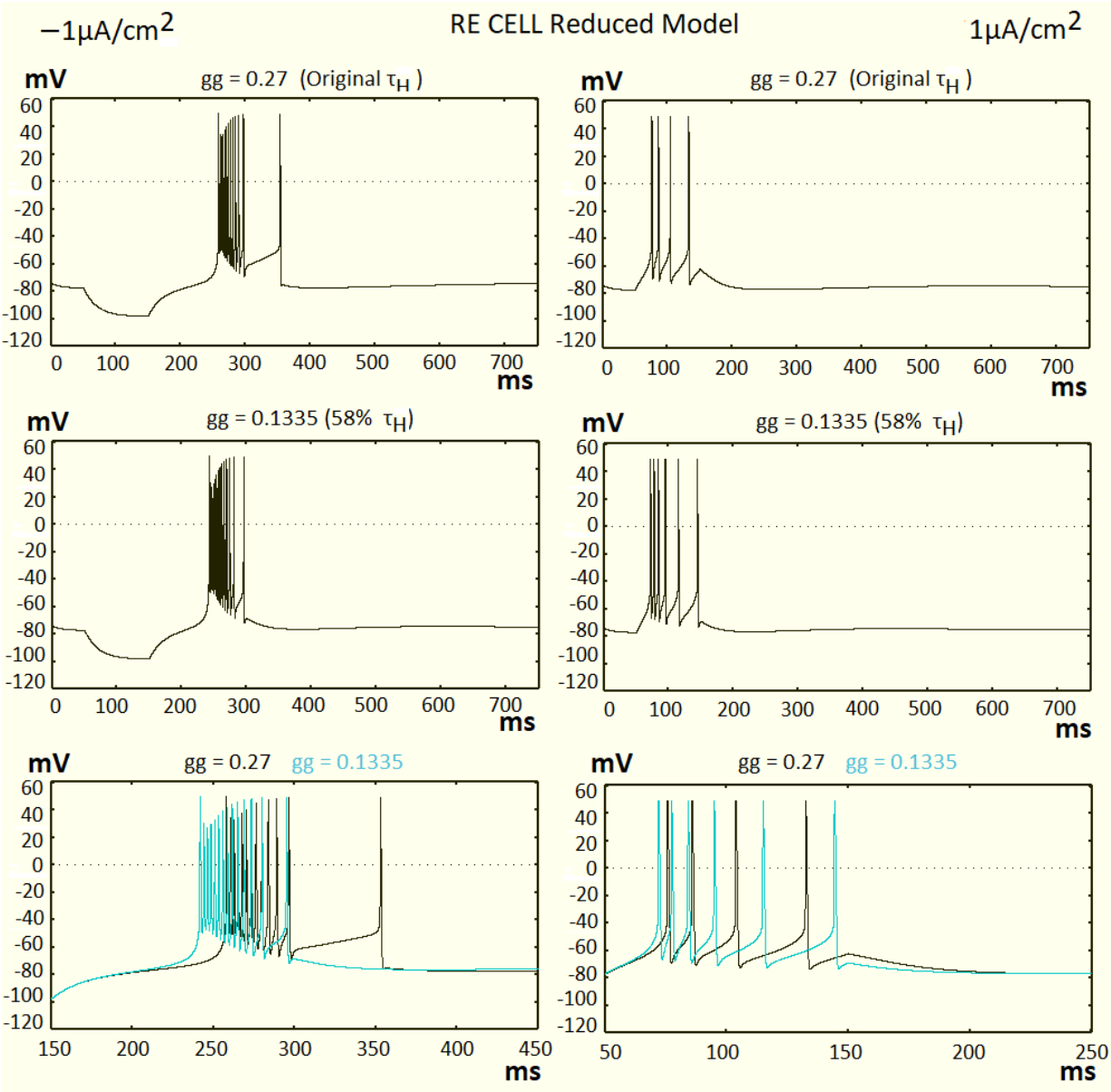

Figure 5.3: Response of individual RE cell (reduced) to varying the τ_H equation of I_T (mV vs ms).

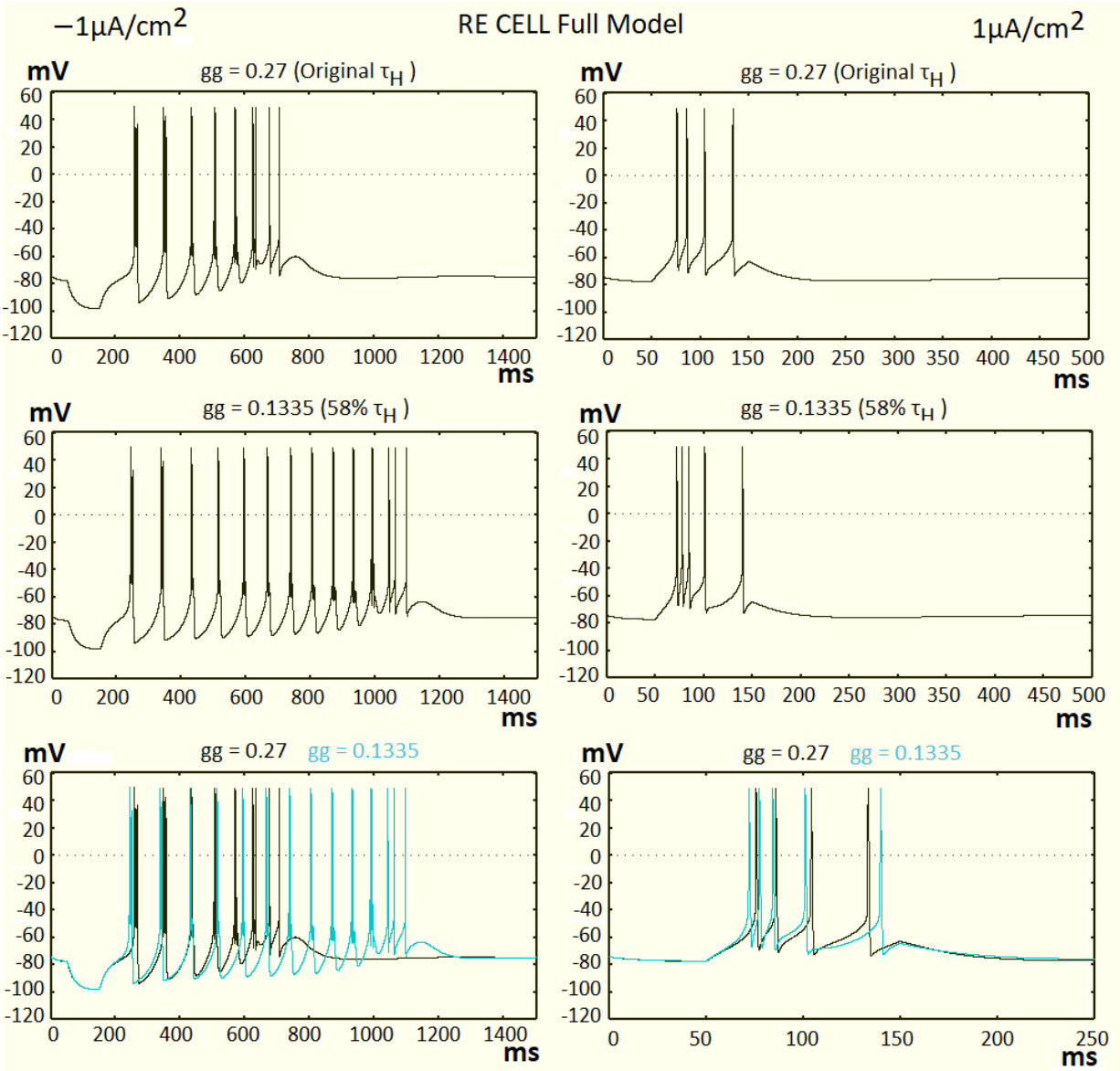

Figure 5.4: Response of individual RE cell (full) to varying the τ_H equation of I_T (mV vs ms).

To observe the effects of the increased inactivation recovery rate on our RE-TC network, we tested our model in the same way as with the $GABA_A$ conductance, in Section 5.1. For each value of the TC's $GABA_A$ conductance ($\bar{g}_{GABA_A} = 0.02$, 0.04, 0.06 and 0.08), we implemented each of our τ_H equations ($gg = 0.27$, 0.1335 and 0.049), and observed the response of the network for each combination of the TC cells' IC's between $-60\,\text{mV}$ and $-70\,\text{mV}$. This resulted in 12 graphs that allowed us to visually observe the patterns of synchronous and alternating bursting prevalence in the model with respect to the values of $\bar{g}_{GABA_A}$ and the τ_H equations. Figures 5.5 and 5.6 displays these 12 graphs for comparison, and Table 5.2 lists the number of synchronous bursting cases for each combination.

From these results, it appears that apart from $\bar{g}_{GABA_A} = 0.04$, the net change as τ_H is decreased from 0.27 to 0.049, is that the occurrence of synchronous bursting either increases slightly or stays the same. Figures 5.5 and 5.6 show that although the net change stayed the same for some values of $\bar{g}_{GABA_A}$, there was some switching between alternating and synchronous bursting for some pairs of IC's. Although these results are not significant enough to conclude that a reduced τ_H equation in the I_T currents increases the occurrence of SWDs, it does imply that it has some effect on it. It is possible that with a larger effect on the individual RE cells, such as from implementing a more intricate method to represent the *CACNA1H* mutation, a larger effect on the network might be seen.

Table 5.2: Percentage of Synchronous Bursting Cases w.r.t. $\bar{g}_{GABA_A}$ and τ_H. *Each percentage is based on the 121-simulation tests from Figures 5.5 and 5.6.*

		gg ($\tau_H(V)$)		
		0.27 (Original)	**0.1335 (58%)**	**0.049 (33%)**
$\bar{g}_{GABA_A}$ (µS)	**0.02**	48.8%	47.1%	48.8%
	0.04	37.2%	37.2%	35.5%
	0.06	25.6%	27.3%	28.9%
	0.08	30.6%	30.6%	30.6%

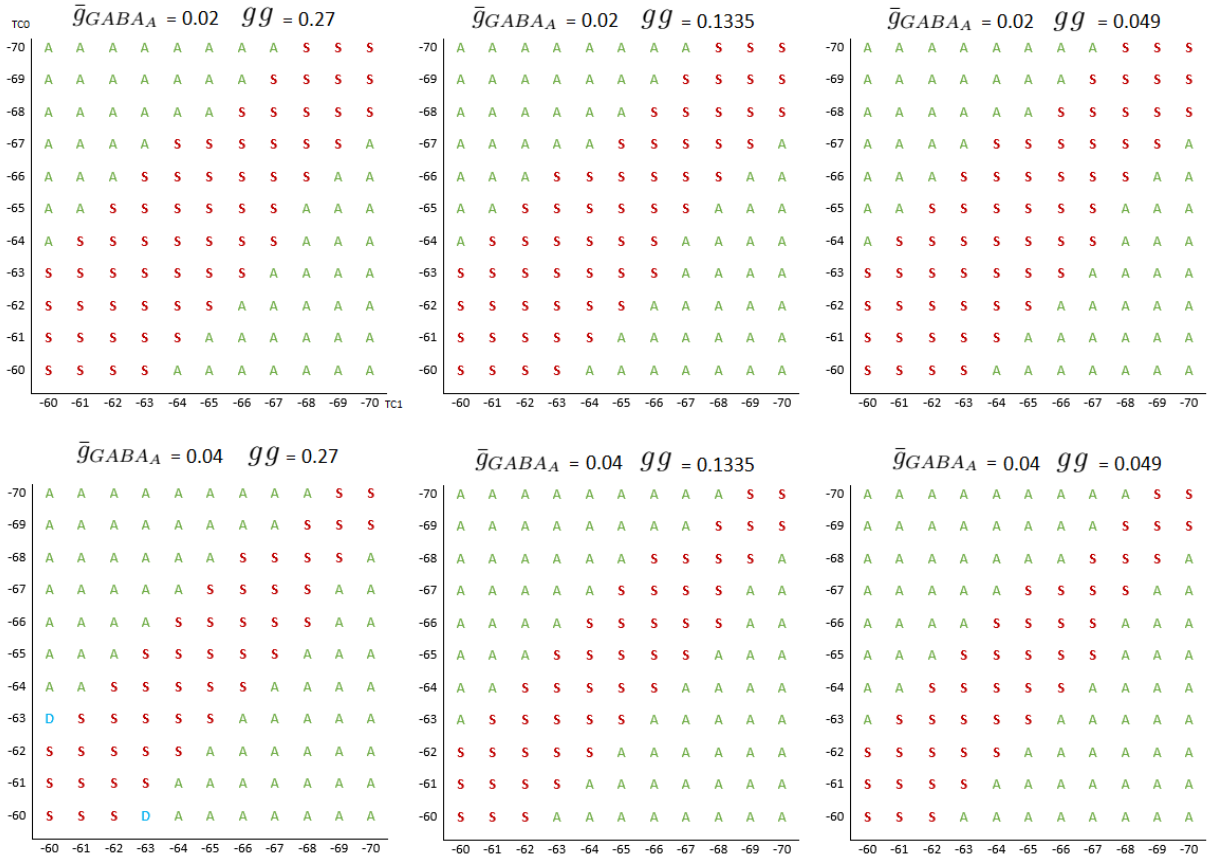

Figure 5.5: Response of RE-TC model to variations in $\tau_H(V)$ and TC initial conditions for $\bar{g}_{GABA_A} = 0.02, 0.04$. A represents alternating bursting and S represents synchronous bursting between the TC cells. D represents one TC cell bursting while the other TC cell is inhibited.

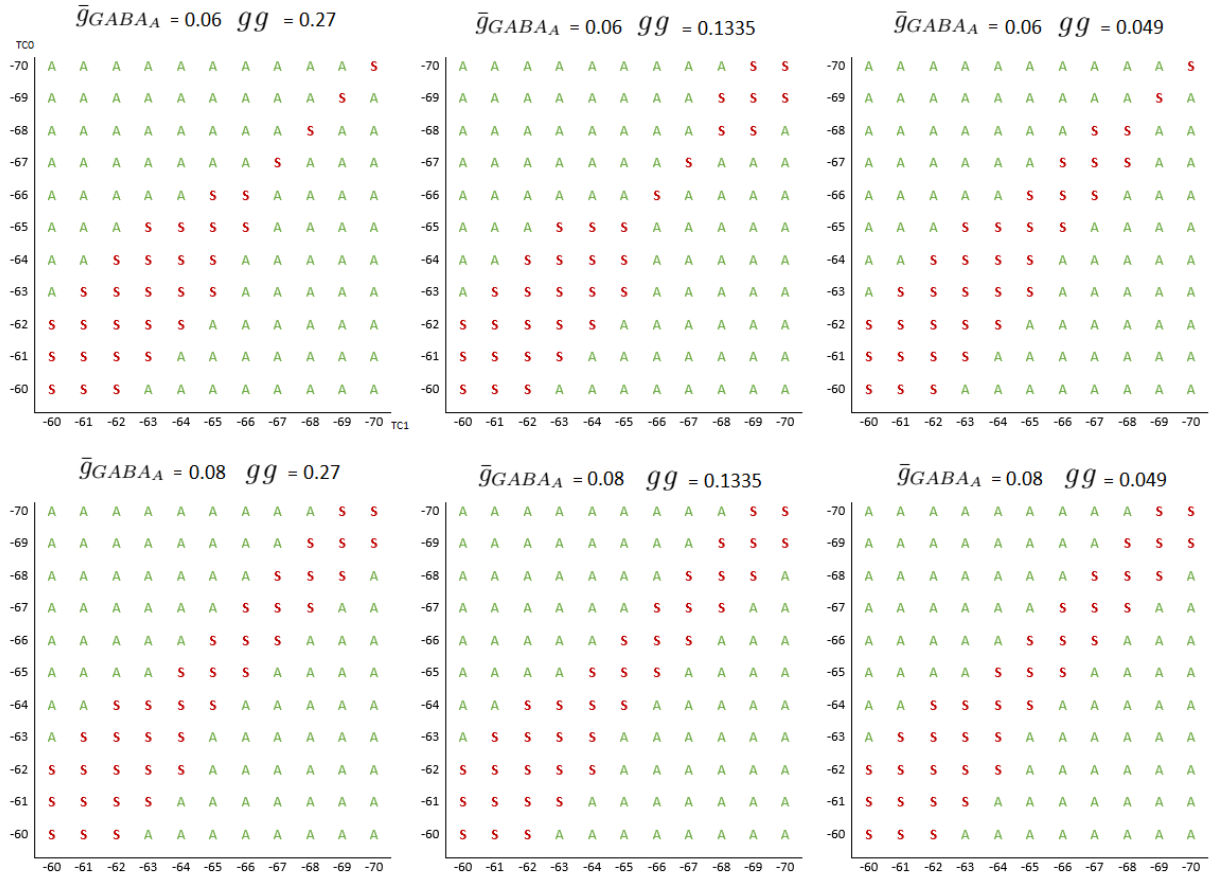

Figure 5.6: Response of RE-TC model to variations in $\tau_H(V)$ and TC initial conditions for $\bar{g}_{GABA_A} = 0.06, 0.08$. A represents alternating bursting and S represents synchronous bursting between the TC cells.

To better understand the effects of the altered τ_H equations on the network, we compared the bursting of a RE cell and a TC cell in each of the networks, with the original, 58% and 33% τ_H equations. We also plotted and compared the $GABA_A$ current (from RE to TC) vs time for each of the τ_H equations, as this current depends on the activity of the RE cells. We used the results from Figures 5.5 and 5.6 to choose specific parameters and ICs so that alternating bursting would occur with the original τ_H equation, and synchronous bursting would occur with the altered τ_H equation.

Figure 5.7 shows the comparisons between the original τ_H equation and the 58% τ_H equation. For the network with the original τ_H, the burst frequency in the RE cell was 13 bursts per 8000 ms, whereas with the 58% τ_H the RE burst frequency was 11 bursts per 8000 ms. An effect was also seen in the comparison of the $GABA_A$ currents, where the current displayed a slightly larger amplitude with the 58% τ_H than with the original τ_H.

For the comparison with the 33% τ_H equation (Figure 5.8), the burst frequency of the RE cells also decreased with the altered τ_H. With the original τ_H, there were again 13 bursts per 8000 ms, and with the 33% τ_H there were 11 bursts per 8000 ms. In comparing the $GABA_A$ current, the 33% τ_H model displayed only a slightly higher amplitude in current than the model with the original τ_H.

Although only a small change in cell behaviour was observed, these results do show an increase in $GABA_A$ synaptic activity when the altered τ_H equations are implemented. This, paired with our other results, again implies that the increased inactivation recovery rate from the *CACNA1H* mutation has some direct effect on the occurrence of synchronous bursting and thus slow wave discharges in the network. As the data we based our τ_H alteration on was limited, our results give a general idea of the effects of the increased inactivation recovery rate on the occurrence of the SWDs associated with childhood absence epilepsy.

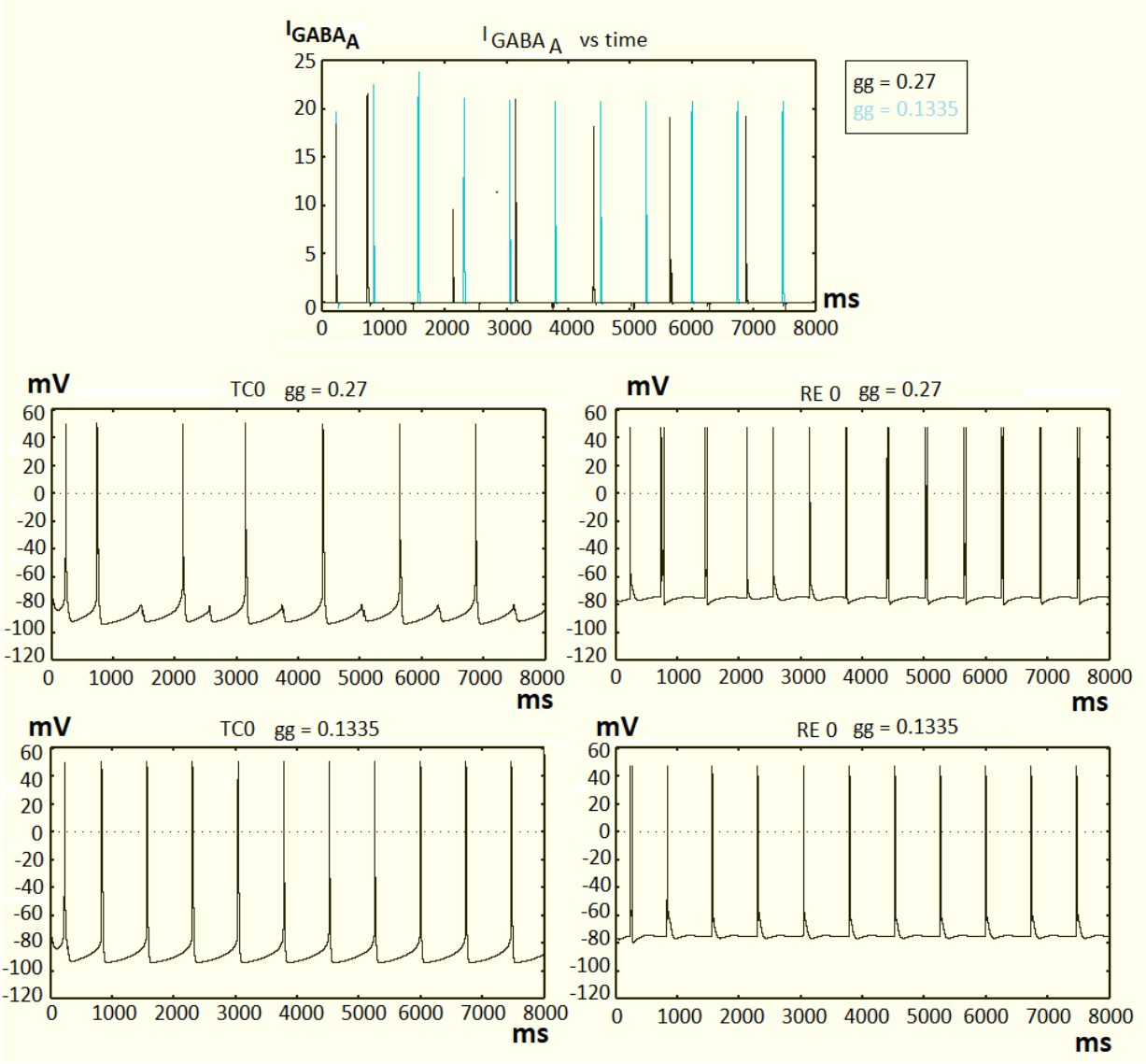

Figure 5.7: Comparing I_{GABA_A} and RE-TC bursting, for the 58% $\tau_H(V)$ ($gg = 0.1335$) (mV vs ms). *Top*: I_{GABA_A} vs Time. *Four images*: RE and TC cell bursting (mV vs ms). *Other Parameters*: $\bar{g}_{GABA_B} = 0.04$, $\bar{g}_{GABA_A} = 0.06$. *Initial Conditions*: TC0 $= -69\,\text{mV}$, TC1 $= -68\,\text{mV}$.

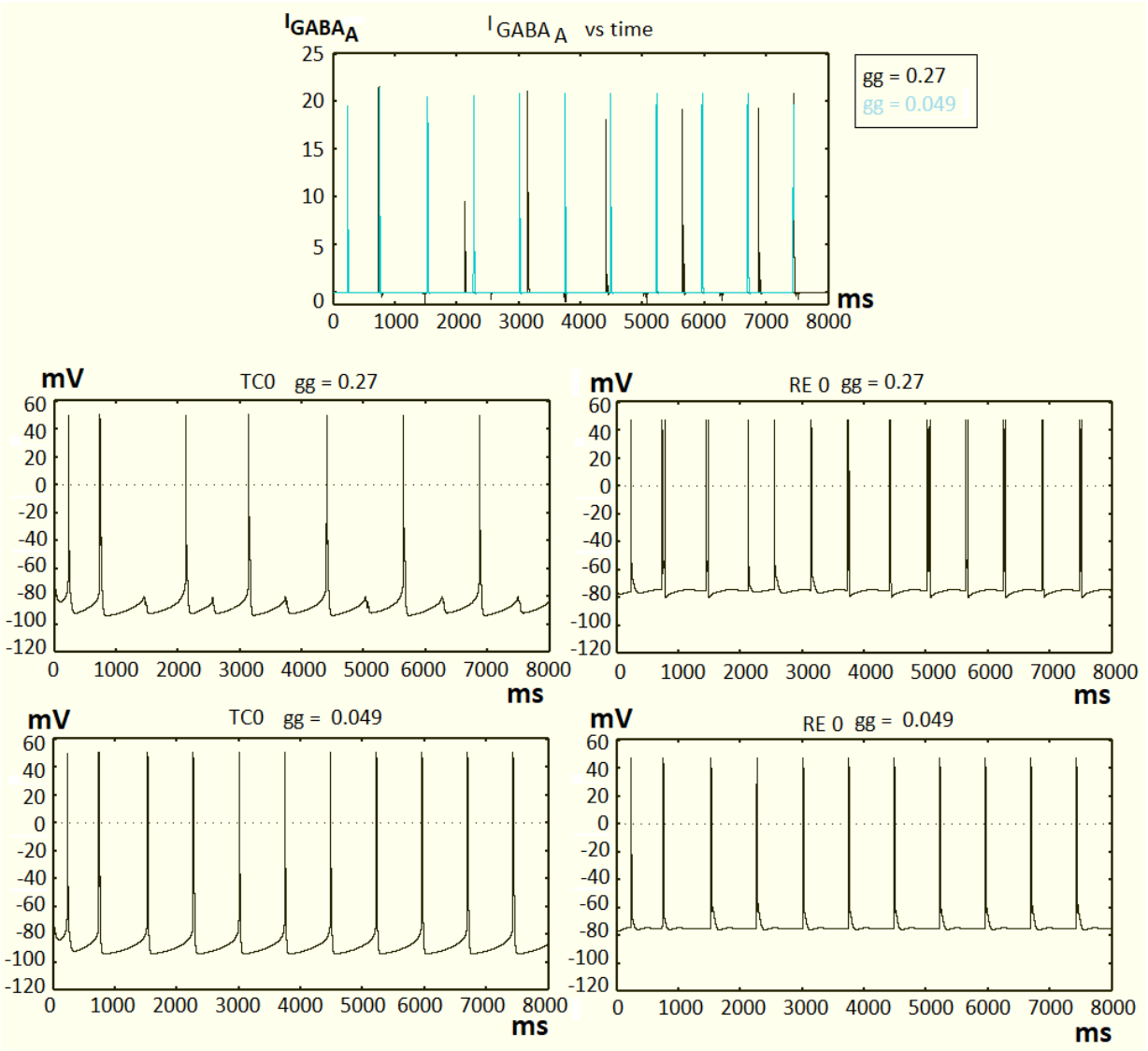

Figure 5.8: Comparing I_{GABA_A} and RE-TC bursting, for the 33% $\tau_H(V)$ ($gg = 0.049$) (mV vs ms). *Top*: I_{GABA_A} vs Time. *Four images*: RE and TC cell bursting (mV vs ms). *Other Parameters*: $\bar{g}_{GABA_B} = 0.04$, $\bar{g}_{GABA_A} = 0.06$. *Initial Conditions*: TC0 = -68 mV, TC1 = -67 mV.

5.3 T-Type Ca^{2+} Channel Conductance

In Section 5.2, we looked at the effects of altering the inactivation time constant equation in the I_T currents of the RE cells. However, we were also interested in studying the general effects of the T-type Ca^{2+} channels on the network. Previous studies have suggested that the T-type Ca^{2+} channels in the thalamocortical network may play a role in the generation of childhood absence epilepsy. As mentioned, in 2005 Vitko et al. studied the effects of the T-type channel gating on thalamic firing [85], and studies by Knox et al. in 2018 looked at the effects of $GABA_A$ synapse and T-type Ca^{2+} channel conductances on thalamocortical network activity. As such, we use our RE-TC network model to study the effects of the I_T conductance on the network behaviour.

In the same way as before, we tested the effects of the I_T current by changing the conductance in the RE cells ($\bar{g}_{Car}$), and observing the response of the network at different levels of $\bar{g}_{GABA_A}$, and for each combination of TC ICs between $-70\,\text{mV}$ and $-60\,\text{mV}$. We considered values of $0.1\,\mu\text{S/cm}^2$, $1.75\,\mu\text{S/cm}^2$ (original), and $2\,\mu\text{S/cm}^2$, for the I_T conductance. We chose not to consider values greater than than $2\,\mu\text{S/cm}^2$ for $\bar{g}_{Car}$, as these values led to the TC cells producing a single spike, before becoming inhibited for the remainder of the simulation. We chose $0.1\,\mu\text{S/cm}^2$ as it was felt that this value was small enough to test the effects of a very minimal I_T conductance. Figures 5.9 and 5.10 display the 12 resulting graphs for these tests, and Table 5.3 lists the number of synchronous bursting cases for each combination of parameter values.

For each value of $\bar{g}_{Car}$, it appeared that as $\bar{g}_{GABA_A}$ was increased from 0.02 through to 0.08, the occurrence of synchronous bursting decreased, with the exception being at $\bar{g}_{GABA_A}$=0.06 with $\bar{g}_{car} = 1.75$. We can also see that for $\bar{g}_{GABA_A}$ values of 0.04 and 0.06, as $\bar{g}_{Car}$ is increased from 0.1 to 2, the occurrence of synchronous bursting increases, and the opposite is true for the more extreme $\bar{g}_{GABA_A}$ values of 0.02 and 0.08. With exceptions, the general trend of our results here does agree with the results from Knox et al. in 2017 [50]. Specifically, that increased I_T and decreased cortical $GABA_A$ functions can lead to SWDs. Although our results here are not significant, they do imply the T-type Ca^{2+} channels could play a role in generating SWDs, especially when considered with other factors.

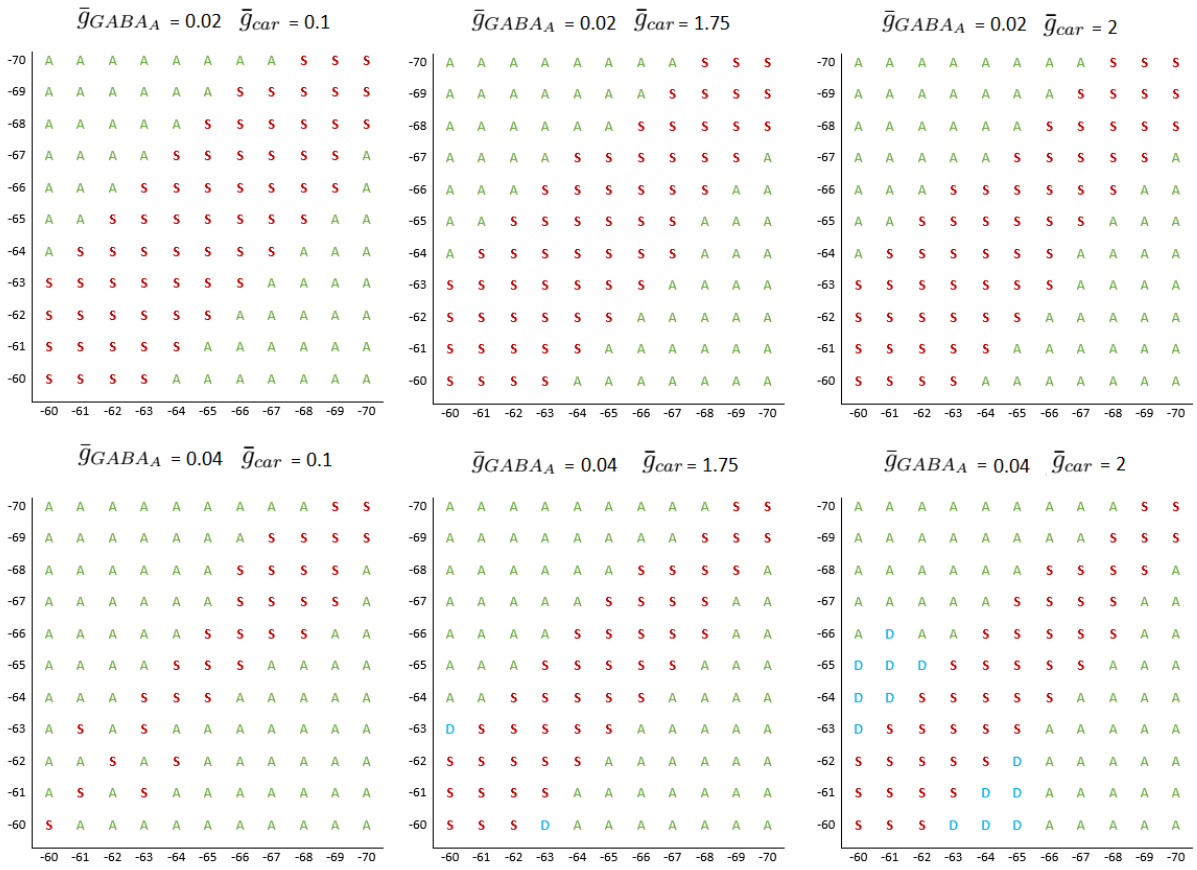

Figure 5.9: Response of RE-TC model to variations in I_T conductance and TC initial conditions for $\bar{g}_{GABA_A} = 0.02, 0.04$. A represents alternating bursting and S represents synchronous bursting between the TC cells. D represents one TC cell bursting while the other TC cell is inhibited.

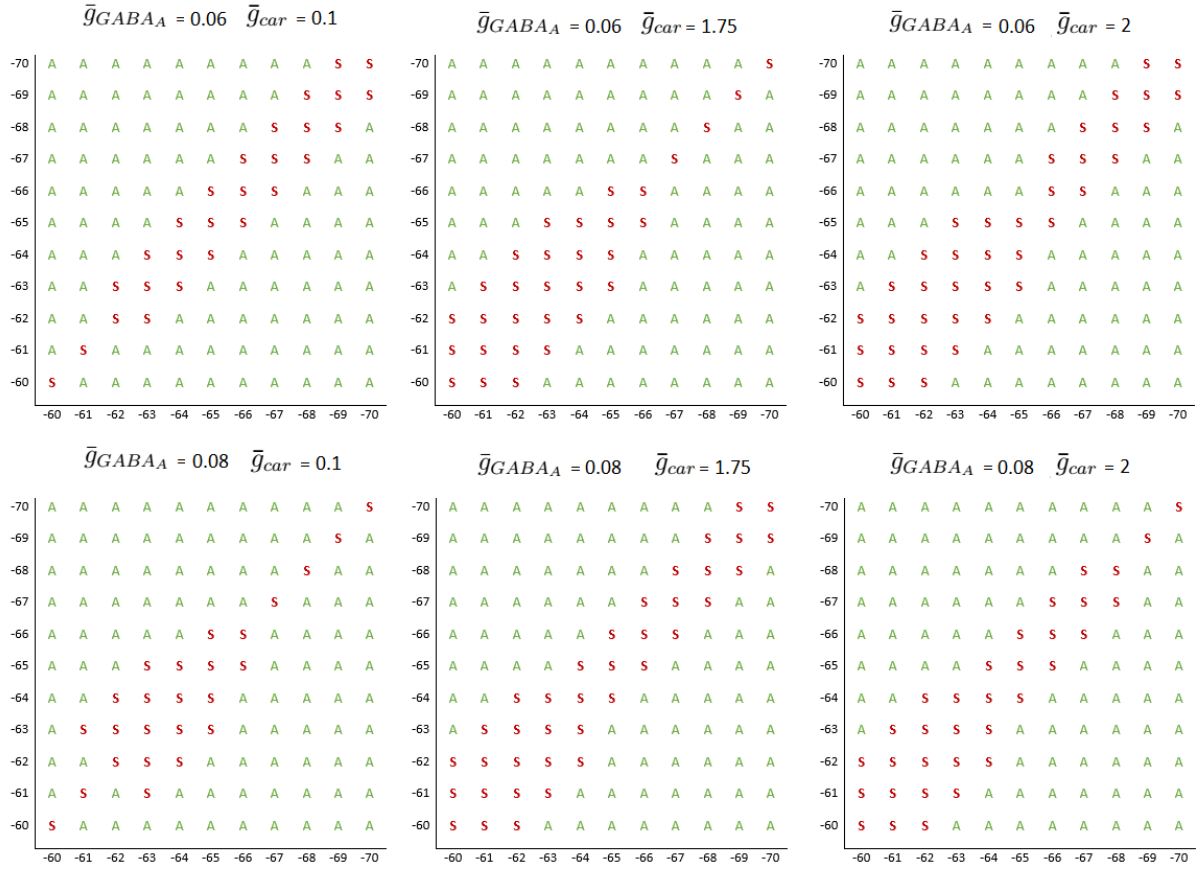

Figure 5.10: Response of RE-TC model to variations in I_T conductance and TC initial conditions for $\bar{g}_{GABA_A} = 0.06, 0.08$. A represents alternating bursting and S represents synchronous bursting between the TC cells.

Table 5.3: Percentage of Synchronous Bursting Cases w.r.t. $\bar{g}_{GABA_A}$ and $\bar{g}_{Car}$. *Each percentage is based on the 121-simulation tests from Figures 5.9 and 5.10.*

		$\bar{g}_{Car}$ (µS/cm^2)		
		0.1	**1.75**	**2**
$\bar{g}_{GABA_A}$ (µS)	**0.02**	52.1%	48.8%	47.1%
	0.04	25.6%	37.2%	37.2%
	0.06	22.3%	25.6%	31.4%
	0.08	20.7%	30.6%	27.3%

Overall, each of the three factors we studied so far in this section have produced some SWD-generating effects on our RE-TC network model. Our results here further support the findings in previous studies that showed a link between each the $GABA_A$ synapses, the *CACNA1H* mutation and the T-type Ca^{2+} channels, and childhood absence epilepsy. Our results also further support the idea that multiple factors together are responsible for the disorder. In the next section, we increase the size of our network to eight cells in order to determine whether our results hold for larger networks.

5.4 8-Cell Network

Before considering a larger network model, we first summarize the results of our four-cell model. We found that with different pairs of initial conditions for the two TC cells, the response of the network varied between alternating and synchronous bursting. Expanding on this property, we also found that changing the $GABA_A$ conductance between the RE and TC cells from 0.02 through to 0.08 resulted in a general decrease in the prevalence of synchronous bursting in the network. Further, we saw that altering the inactivation recovery rate in the I_T currents of the RE cells, as well as changing the I_T conductance in the RE cells, also influenced whether the network produced alternating or synchronous bursting. With this, our next step was to develop an eight-cell network in order to determine whether our previous results were valid for larger network models. Here, we also observed what effects more diverse combinations of TC ICs had on the model.

As mentioned, we created our eight-cell model in the same way as our four-cell model. Specifically, each RE cell was connected to every other RE cell via $GABA_A$ synapses, each RE cell received input from each of the TC cells via AMPA synapses, and each TC cell received input from each RE cell via $GABA_A$ and $GABA_B$ synapses. The cells' parameters

were kept the same, holding the I_T conductance and the τ_H equation at their original values, with $\bar{g}_{Car} = 1.75$ and $gg = 0.27$. The synaptic conductances were an exception, which were altered according to the number of corresponding connections in the network; $\bar{g}_{AMPA} = 0.1$, $\bar{g}_{GABA_A} = 0.067$ (to RE cells), $\bar{g}_{GABA_B} = 0.02$, and $\bar{g}_{GABA_A} = 0.01$, 0.02, 0.03 and 0.04 (to TC cells).

Comparing Results from the 4- and 8-Cell Models

To determine whether our results from our four-cell model hold for larger networks, we tested our network in the following way. For the subset of TC ICs that observed the most changes between synchronous and alternating bursting when changing $\bar{g}_{GABA_A}$, we observed the response of our eight-cell network at these pairs of ICs for each value of $\bar{g}_{GABA_A}$. We separated our four TC cells into two pairs, and assigned one IC value to each pair. We considered $\bar{g}_{GABA} = 0.01$, 0.02, 0.03, 0.04, as these values correspond to the original change in $\mathrm{GABA_A}$ conductance with the four-cell model. The specific ICs considered were $-64\,\mathrm{mV}$ through to $-68\,\mathrm{mV}$.

Figure 5.11 shows a comparison of the subset of ICs for both the eight-cell and four-cell networks at each of the corresponding $\bar{g}_{GABA_A}$ values. As shown, there is no difference in response of the network between the two models. We also tested this subset of ICs for changes in the τ_H equation, as before, and also found no difference between the eight- and four-cell models (not pictured). With no difference at all, it is implied that our previous results will hold for larger networks.

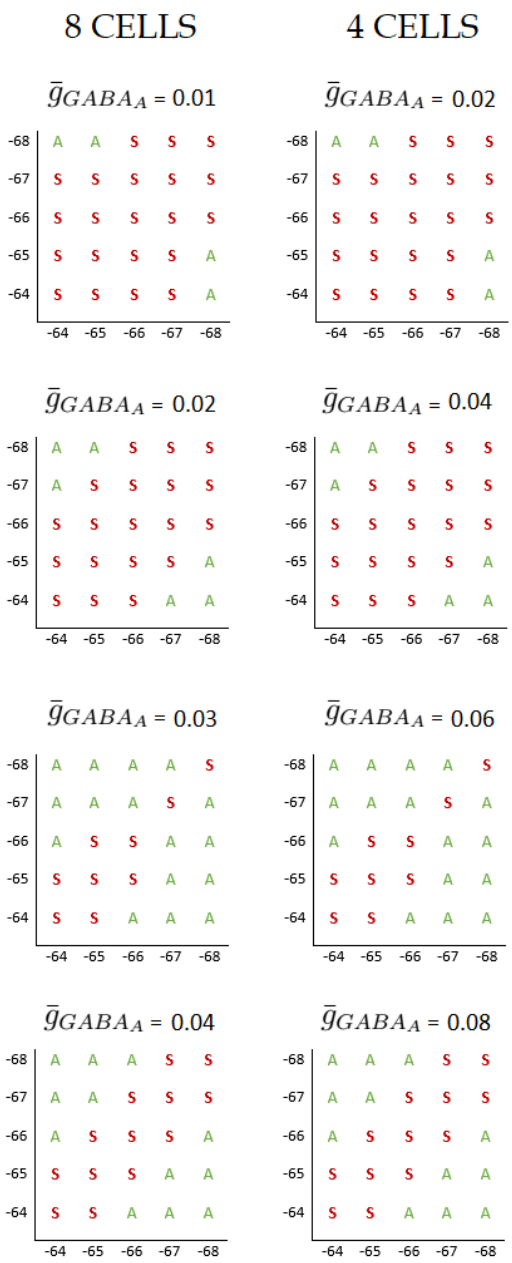

Figure 5.11: Response of 8-cell vs 4-cell RE-TC model to variations in $\bar{g}_{GABA_A}$ and TC cell initial conditions. A represents alternating bursting and S represents synchronous bursting between the TC cells. *Note that there is no difference between the two.*

Effects of Differing TC IC Combinations

Having only used combinations of two ICs for the TC cells in our four-cell model, here we considered the effects of implementing different combinations of ICs for the TC cells. We considered only the sensitive subset of TC ICs ($-64\,\text{mV}$ to $-68\,\text{mV}$), and started by considering the five combinations where all four ICs were different. From there, we then looked at the cases where three ICs were the same with only one IC different, and then considered only a couple of cases where two TC ICs were the same and the other two different. It is also noted that since each TC cell is connected in the same manner as every other TC cell, the assignment of which IC to which cell is not important. Here, we considered it synchronous bursting if all four TC cells spiked together, and alternating bursting if two subsets of cells spiked opposite of each other. Figures 5.12 to 5.14 illustrate the results, with S representing synchronous bursting and A representing alternating bursting. The numbers in the parentheses represent which cells were bursting opposite each other, i.e., (0 - 123) indicates TC0 was bursting opposite TC1, TC2 and TC3. It is also noted that the bursting frequency was the same in each of the cases, as was the amplitude of the spikes, with six to seven bursts per 4000 ms and an amplitude of approximately 45 mV.

ALL DIFFERENT

[TC0 TC2; TC1 TC3]

	-64 -66 -65 -67	-64 -66 -65 -68	-64 -67 -65 -68	-64 -67 -66 -68	-65 -67 -66 -68
0.01	S	A (0 - 123)	A (0 - 123)	S	A (0 - 123)
0.02	A (0 - 123)	A (01 - 23)	A (01 - 23)	A (0 - 123)	A (0 - 123)
0.03	A (0 - 123)	A (01 - 23)	A (01 - 23)	A (0 - 123)	A (0 - 123)
0.04	A (0 - 123)	A (01 - 23)	A (01 - 23)	A (0 - 123)	A (0 - 123)

Figure 5.12: Response of 8-cell RE-TC model to variations in TC initial conditions (*all different*). A represents alternating bursting and S represents synchronous bursting between the TC cells.

As shown in Figure 5.12, when all four TC ICs were different, the network was more likely to produce alternating bursting. This coincides with our previous results from the four-cell model, where for pairs of similar or identical ICs, synchronous bursting occurred, and for pairs that were very different, alternating bursting resulted. It is also noted that in some cases there was one cell that spiked opposite of the other three, and in other cases two cells spiked opposite of the other two. The reason for this is unclear, as there is not a distinct pattern as to which sets of ICs or $\bar{g}_{GABA_A}$ values cause the 1-3 bursting and the 2-2 bursting in this case.

For the simulations with three identical ICs and one different (Figure 5.13), we see the same trend in the results. When the difference between the two IC values is large, at least 2 to 3 mV, alternating bursting occurs, whereas synchronous bursting occurs otherwise. It is also noted that unlike the previous simulations with all different IC's, in each situation where alternating bursting occurred, it was the cell with the different IC that spiked opposite of the other three.

As for the cases with only two different (Figure 5.14), the same trend appears. For the most part, when the three values of IC's are close to each other, the network responds with synchronous bursting, and when there is a large difference between at least two of the IC values, alternating bursting occurs. It also appears that for the lower values of $\bar{g}_{GABA_A}$ (0.01 and 0.02) it is more likely that synchronous bursting will occur, and for larger values (0.03 and 0.04) the network tends to respond with alternating bursting, even for the same combination of IC's.

Overall, the general trend appears to be that the cell, or set of cells, that differs the most in value from the others, bursts opposite of the other cells. However, this pattern does not hold over every simulation. Also, in some cases, with higher values of $\bar{g}_{GABA_A}$, there are more alternating bursting cases than synchronous bursting cases.

With all of this considered, it appears that the results from our eight-cell model coincide with those from our four-cell model. Specifically, our tests regarding the effects of $\bar{g}_{GABA_A}$ and τ_H on the network, comparing the network behaviour for the same subset of TC ICs, showed the exact same results. With our tests of differing ICs and $\bar{g}_{GABA_A}$, we saw that for some combinations of ICs, with a larger $\bar{g}_{GABA_A}$, less synchronous bursting occurred, which was a general trend observed in Section 5.1. As such, it is implied that our four-cell model can be expanded in size, and the effects on the network should not change.

3 THE SAME

TC0 TC2
TC1 TC3

	-64 -64 -64 -65	-64 -64 -64 -66	-64 -64 -64 -67	-64 -64 -64 -68
0.01	S	S	S	A (012 - 3)
0.02	S	S	A (012 - 3)	A (012 - 3)
0.03	S	S	A (012 - 3)	A (012 - 3)
0.04	S	S	A (012 - 3)	A (012 - 3)

	-65 -65 -65 -64	-65 -65 -65 -66	-65 -65 -65 -67	-65 -65 -65 -68
0.01	S	S	S	S
0.02	S	S	S	A (012 - 3)
0.03	A (012 - 3)	S	S	A (012 - 3)
0.04	S	S	S	A (012 - 3)

	-66 -66 -66 -64	-66 -66 -66 -65	-66 -66 -66 -67	-66 -66 -66 -68
0.01	S	S	S	S
0.02	S	S	S	S
0.03	A (012 - 3)	A (012 - 3)	S	S
0.04	A (012 - 3)	S	S	S

	-67 -67 -67 -64	-67 -67 -67 -65	-67 -67 -67 -66	-67 -67 -67 -68
0.01	A (012 - 3)	S	S	S
0.02	A (012 - 3)	A (012 - 3)	S	S
0.03	A (012 - 3)	A (012 - 3)	A (012 - 3)	S
0.04	A (012 - 3)	A (012 - 3)	S	S

	-68 -68 -68 -64	-68 -68 -68 -65	-68 -68 -68 -66	-68 -68 -68 -67
0.01	A (012 - 3)	A (012 - 3)	S	S
0.02	A (012 - 3)	A (012 - 3)	A (012 - 3)	S
0.03	A (012 - 3)	A (012 - 3)	A (012 - 3)	A (012 - 3)
0.04	A (012 - 3)	A (012 - 3)	A (012 - 3)	S

Figure 5.13: Response of 8-cell RE-TC model to variations in TC initial conditions (*3 same*). *A* represents alternating bursting and *S* represents synchronous bursting between the TC cells.

2 THE SAME

TC0 TC2
TC1 TC3

	-64 -65 -64 -66	-64 -67 -64 -68	-66 -67 -66 -65	-66 -64 -66 -68
0.01	S	A (01 - 23)	S	A (013 - 2)
0.02	S	A (01 - 23)	S	A (013 - 2)
0.03	S	A (01 - 23)	S	A (013 - 2)
0.04	S	A (01 - 23)	S	A (013 - 2)

	-67 -68 -67 -66	-67 -65 -67 -64	-68 -65 -68 -66	-68 -67 -68 -66
0.01	S	A (012 - 3)	A (013 - 2)	S
0.02	S	A (012 - 3)	A (013 - 2)	S
0.03	A (012 - 3)	A (01 - 23)	A (01 - 23)	A (012 - 3)
0.04	S	A (01 - 23)	A (01 - 23)	A (012 - 3)

Figure 5.14: Response of 8-cell RE-TC model to variations in TC initial conditions (*2 same*). *A* represents alternating bursting and *S* represents synchronous bursting between the TC cells.

Chapter 6

Conclusions

We started the development of our RE-TC network model by creating a RE cell model based on the model presented by Destexhe et al. in 1994 [22]. Our RE model displayed typical RE cell behaviour, including the ability to create a rebound burst in response to hyperpolarizing input. We then created networks of two and five RE cells, and saw that our RE cells were able to inhibit one another, as well as respond to inhibition. Our results here were not exactly the same as those by Destexhe et al., however this could be due to the difference in how our $GABA_A$ synapses were modelled. We developed the model for the TC cell based on Destexhe et al.'s model from 1996 [21]. Due to the absence of calcium-dependence in our I_H current, our model was not able to produce waxing and waning oscillations, however it did display spontaneous oscillations, a rest state, delta oscillations and the ability to produce rebound bursts from hyperpolarizations.

After combining our two models to produce the RE-TC network, we were able to determine a set of parameters that could produce both alternating bursting as well as synchronous bursting between the TC cells in the network. We were interested in this, as alternating bursting represented 'healthy', non-seizure activity in the network, whereas synchronous bursting was representative of absence seizure and SWD activity. Once this was achieved, we tested the $GABA_A$ synapse conductance, the *CACNA1H* mutation and the I_T conductance on the network, to observe how these factors affected the ability of the network to switch between alternating and synchronous activity.

With the initial conditions, we found that when the TC ICs were similar in value, synchronous bursting occurred, whereas with initial conditions that were farther apart, alternating bursting occurred. This result made sense, as similar parameter values should lead to similar activity in the cells, which in this case would be bursting in synchrony. We

tested the effects of the $GABA_A$ (from RE to TC) synapse on the network, by altering the value of the conductance, and found that as the conductance was increased, the prevalence of synchronous bursting in the network decreased. This result also made sense, as with increased function of the $GABA_A$ currents, the RE cells could inhibit the TC cells more, leading to a decrease in TC bursting activity.

We also implemented the *CACNA1H* mutation in the network, by altering the inactivation time constant equation in the I_T current of the RE cells, and found that this mutation had only a small effect on the network. Specifically, only when $\bar{g}_{GABA}$ was 0.06 (µS) did we see any significant changes in the prevalence of synchronous bursting in the network. One explanation for this is in the way we implemented the mutation. We altered our τ_H equation in a simplistic way, by altering the coefficient of the equation based on two values that were presented in one study. Perhaps if we considered the results from multiple studies, and consolidated them into a more intricate method of implementing the mutation, our network might have produced more significant results.

We tested the effects of the T-type Ca^{2+} channel by altering the value of the I_T conductance. Here, we found more variation in the prevalence of synchronous bursting across the levels of factors being considered, than we did with the *CACNA1H* mutation. For some values of $\bar{g}_{GABA}$, as the I_T conductance was increased, the prevalence of synchronous bursting increased, and for each value of I_T conductance, as $\bar{g}_{GABA}$ was decreased, the synchronous bursting mostly decreased as well. As other studies (Knox et al., 2018 [50]) showed a definitive trend between SWD activity and the interactions of I_T conductance and $GABA_A$ conductance, the lack of this trend in our results may be due to the simplicity of our model. Specifically, in Knox et al.'s study, neurons from the cortex and thalamus were considered in their model, however we only considered neurons from the thalamus. Perhaps if we included cortical neurons, allowing for extra excitatory and inhibitory activity between the neurons we currently have, a more conclusive result might have been observed. Expanding on this idea, it is possible that many of our results here, regarding the $GABA_A$ conductance, the I_T conductance and especially the *CACNA1H* mutation, could have been more definitive with the inclusion of the cortical neurons in our model.

Since we did not observe any significant changes in synchronous/SWD patterns when testing our thalamic model of the thalamocortical network, we conclude that the thalamus may not be solely responsible for SWD activity. Further, as we did not observe the ability of our network to switch to synchronous bursting from alternating bursting within the same simulation, this implies that the thalamus part of the thalamocortical network may not be responsible for the initiation of SWDs. Both of these results coincide with previous studies that have suggested that both the thalamus and the cortex are involved the propagation of SWDs. Not only this, but that a region of the thalamocortical network other than the

thalamus (perhaps the somatosensory cortex) may be the source of SWD initiation [61].

Overall, our results here imply the same general conclusion as many other studies that have addressed the causes of childhood absence epilepsy. That is, that the disorder is not likely to be caused by one particular gene or factor, but by multiple factors together [13]. As we saw, the prevalence of synchronous bursting, or SWD activity, in our network relied on the interactions of multiple factors, and not just one in particular. Although our results indicated the possibility of the *CACNA1H* gene, the $GABA_A$ synapses and the T-type Ca^{2+} channels, as part of the cause of CAE, further studies are still needed in order to determine the specific set of genes and causes responsible for the disorder.

6.1 Future Directions

As mentioned, further research is required in order to determine the causes of childhood absence epilepsy. Expanding on our model and results presented here, one approach that could be taken would be to implement the *CACNA1H* mutation in a more detailed manner. As discussed, examining the results from multiple studies of this gene might allow for a more intricate method of implementation, which could give more significant and determinant results.

In a similar way, one could implement the *NIPA2* mutation, discussed in Section 3.2, into the network. This mutation is involved with magnesium transport, and so is believed to possibly affect NMDA receptors in the thalamocortical network. This approach would require more work, however, as currently our network does not include NMDA synapses. However, with a less simplistic model of the thalamocortical network, the implementation of this genetic mutation might provide some useful results.

In saying this, implementing more cell types into our network to create a full, or partially-full, model of the thalamocortical network, would be useful for obtaining more accurate results when testing certain factors and genetic defects in relation to CAE. At a minimum, cell types from the cortex, such as cortical pyramidal and cortical inhibitory neurons, would allow for a general idea of how the thalamocortical network behaves as a whole in response to testing certain factors. Ideally, a better representative model of the thalamocortical network would allow for the specific set of genes responsible for CAE to be determined, however much work would still be required in order to achieve this.

References

[1] S. Ackerman. *Major Structures and Functions of the Brain*. National Academies Press, Washington, DC, 1992.

[2] G. Avanzini, M. de Curtis, F. Panzica, and R. Spreafico. Intrinsic properties of nucleus reticularis thalami neurones of the rat studied *in vitro*. *The Journal of Physiology*, 416:111–122, 1989.

[3] T. Bal and D. McCormick. What stops synchronized thalamocortical oscillations? *Neuron*, 17(2):297–308, 1996.

[4] M. Bébarová. Advances in patch clamp technique: Towards higher quality and quantity. *General Physiology and Biophysics*, 31:131–140, 2012.

[5] C. Binnie and P. Prior. Electroencephalography. *Journal of Neurology, Neurosurgery, and Psychiatry*, 57:1308–1319, 1994.

[6] E. Botzolakis, J. Zhao, K. Gurba, R. Macdonald, and P. Hedera. The effect of HSP-causing mutations in *SPG3A* and *NIPA1* on the assembly, trafficking, and interaction between atlastin-1 and NIPA1. *Molecular and Cellular Neuroscience*, 46(1):122–135, 2011.

[7] S. Cain and T. Snutch. T-type calcium channels in burst-firing, network synchrony, and epilepsy. *Biochimica et Biophysica Acta*, 1828(7):1572–1578, 2013.

[8] Y. Chen, J. Lu, H. Pan, Y. Zhang, H. Wu, K. Xu, et al. Association between genetic variation of *CACNA1H* and childhood absence epilepsy. *Annals of Neurology*, 54(2):239–243, 2003.

[9] D. Contreras, A. Destexhe, T. Sejnowski, and M. Steriade. Spatiotemporal patterns of spindle oscillations in cortex and thalamus. *Journal of Neuroscience*, 17(3):1179–1196, 1997.

[10] D. Contreras, R. Curro Dossi, and M. Steriade. Electrophysiological properties of cat reticular neurones *in vivo*. *The Journal of Physiology*, 470(1):273–294, 1993.

[11] J. Crank and P. Nicolson. A practical method for numerical evaluation of solutions of partial differential equations of the heat-conduction type. *Mathematical Proceedings of the Cambridge Philosophical Society*, 43(1):50–67, 1947.

[12] V. Crunelli, D. Cope, and J. Terry. Transition to absence seizures and the role of $GABA_A$ receptors. *Epilepsy Research*, 97(3):283–289, 2011.

[13] V. Crunelli and N. Leresche. Childhood absence epilepsy: Genes, channels, neurons and networks. *Nature Reviews Neuroscience*, 3(5):371–382, 2002.

[14] K. Dabrowski, D. Castaño, and J. Tartar. Basic neuron model electrical equivalent circuit: An undergraduate laboratory exercise. *Journal of Undergraduate Neuroscience Education*, 12(1):A49–52, 2013.

[15] A. Depaulis and S. Charpier. Pathophysiology of absence epilepsy: Insights from genetic models. *Neuroscience Letters*, 667(2018):53–65, 2017.

[16] A. Depaulis, O. David, and S. Charpier. The genetic absence epilepsy rat from Strasbourg as a model to decipher the neuronal and network mechanisms of generalized idiopathic epilepsies. *Journal of Neuroscience Methods*, 260:159–174, 2016.

[17] M. Deschênes, M. Paradis, J.P. Roy, and M. Steriade. Electrophysiology of neurons of lateral thalamic nuclei in cat: Resting properties and burst discharges. *Journal of Neurophysiology*, 51(6):1196–1219, 1984.

[18] A. Destexhe. Spike-and-wave oscillations based on the properties of $GABA_B$ receptors. *The Journal of Neuroscience*, 18(21):9099–9111, 1998.

[19] A. Destexhe. Network models of absence seizures. In C. Faingold and H. Blumenfeld, editors, *Neuronal Networks in Brain Function, CNS Disorders, and Therapeutics*, chapter 2, pages 11–35. Elsevier, 2014.

[20] A. Destexhe, A. Babloyantz, and T.J. Sejnowski. Ionic mechanisms for intrinsic slow oscillations in thalamic relay neurons. *Biophysical Journal*, 65(4):1538–1552, 1993.

[21] A. Destexhe, T. Bal, D. McCormick, and T.J. Sejnowski. Ionic mechanisms underlying synchronized oscillations and propagating waves in a model of ferret thalamic slices. *Journal of Neurophysiology*, 76(3):2049–2070, 1996. ModelDB Accession Number: 3343.

[22] A. Destexhe, D. Contreras, T.J. Sejnowski, and M. Steriade. A model of spindle rhythmicity in the isolated thalamic reticular nucleus. *Journal of Neurophysiology*, 72(2):803–818, 1994. ModelDB Accession Number: 3670.

[23] A. Destexhe, D. Contreras, and M. Steriade. LTS cells in cerebral cortex and their role in generating spike-and-wave oscillations. *Neurocomputing*, 38:555–563, 2001.

[24] A. Destexhe, D. Contreras, M. Steriade, and T.J. Sejnowski. *In vivo*, *in vitro*, and computational analysis of dendritic calcium currents in thalamic reticular neurons. *The Journal of Neuroscience*, 16(1):169–185, 1996.

[25] A. Destexhe, Z. Mainen, and T. Sejnowski. An efficient method for computing synaptic conductances based on a kinetic model of receptor binding. *Neural Computation*, 6(1):14–18, 1994.

[26] A. Destexhe, Z. Mainen, and T.J. Sejnowski. Synthesis of models for excitable membranes, synaptic transmission and neuromodulation using a common kinetic formalism. *Journal of Computational Neuroscience*, 1(3):195–230, 1994.

[27] A. Destexhe, D. McCormick, and T.J. Sejnowski. A model for 8-10 Hz spindling in interconnected thalamic relay and reticularis neurons. *Biophysical Journal*, 65(6):2473–2477, 1993.

[28] A. Destexhe, M. Neubig, D. Ulrich, and J. Huguenard. Dendritic low-threshold calcium currents in thalamic relay cells. *The Journal of Neuroscience*, 18(10):3574–3588, 1998.

[29] A. Destexhe and T.J. Sejnowski. G protein activation kinetics and spillover of gamma-aminobutyric acid may account for differences between inhibitory responses in the hippocampus and thalamus. *Proceedings of the National Academy of Sciences of the United States of America*, 92(21):9515–9519, 1995.

[30] A. Destexhe and T.J. Sejnowski. Interactions between membrane conductances underlying thalamocortical slow-wave oscillations. *Physiological Reviews*, 83(4):1401–1453, 2003.

[31] B. Ermentrout. XPPAUT. scholarpedia, 2(1):1399., revision 136177., 2007. DOI:10.4249/scholarpedia.1399.

[32] B. Ermentrout. XPP-AUT: X-windows phaseplane plus auto, 2016. www.math.pitt.edu/ bard/xpp/xpp.html. Accessed: 2019-02-23.

[33] B. Ermentrout and D. Terman. *Mathematical Foundations of Neuroscience*. Springer, New York, 2010.

[34] R. Fisher, W. van Emde Boas, W. Blume, C. Elger, P. Genton, et al. Epileptic seizures and epilepsy: Definitions proposed by the International League Against Epilepsy (ILAE) and the International Bureau for Epilepsy (IBE). *Epilepsia*, 46(4):470–472, 2005.

[35] M. Goldenberg. Overview of drugs used for epilepsy and seizures. *Pharmacy and Therapeutics*, 35(7):392–415, 2010.

[36] S. Herculano-Houzel. The human brain in numbers: A linearly scaled-up primate brain. *Frontiers in Human Neuroscience*, 3(31):1–11, 2009.

[37] S. Heron, H. Khosravani, D. Varela, C. Bladen, T. Williams, M. Newman, et al. Extended spectrum of idiopathic generalized epilepsies associated with *CACNA1H* functional variants. *Annals of Neurology*, 62(6):560–568, 2007.

[38] M. Hines. NEURON – a program for simulation of nerve equations. In F. Eeckman, editor, *Neural Systems: Analysis and Modeling*, pages 127–136. Springer US, Boston, MA, 1993.

[39] A. Hodgkin, A. Huxley, and B. Katz. Measurement of current-voltage relations in the membrane of the giant axon of *Loligo*. *Journal of Physiology*, 116(4):424–448, 1952.

[40] J. Huguenard. Low-threshold calcium currents in central nervous system neurons. *Annual Review of Physiology*, 58:329–348, 1996.

[41] J. Huguenard. Mechanisms of excitability in the thalamocortical circuit. *Eplipsia*, 51(Suppl. 5):25, 2010.

[42] J. Huguenard and D. McCormick. Simulation of the currents involved in rhythmic oscillations in thalamic relay neurons. *Journal of Neurophysiology*, 68(4):1373–1383, 1992.

[43] J. Huguenard and D. Prince. A novel T-type current underlies prolonged Ca^{2+}-dependent burst firing in GABAergic neurons of rat thalamic reticular nucleus. *The Journal of Neuroscience*, 12(10):3804–3817, 1992.

[44] P. Iannetti, A. Spalice, P. De Luca, S. Boemi, A. Festa, and C. Maini. Ictal single photon emission computed tomography in absence seizures: Apparent implication of different neuronal mechanisms. *Journal of Child Neurology*, 16(5):339–344, 2001.

[45] H. Jahnsen and R. Llinás. Electrophysiological properties of guinea-pig thalamic neurones: An *in vitro* study. *The Journal of Physiology*, 349:205–226, 1984.

[46] Y. Jiang, Y. Zhang, P. Zhang, T. Sang, F. Zhang, T. Ji, et al. *NIPA1* located in 15q11.2 is mutated in patients with childhood absence epilepsy. *Human Genetics*, 131(7):1217–1224, 2012.

[47] A. Jouvenceau, L. Eunson, A. Spauschus, V. Ramesh, S. Zuberi, et al. Human epilepsy associated with dysfunction of the brain P/Q-type calcium channel. *The Lancet*, 358(9284):801–807, 2001.

[48] A. Karpova, A. Bikbaev, A. Coenen, and G. van Luijtelaar. Morphometric golgi study of cortical locations in WAG/Rij rats: The cortical focus theory. *Neuroscience Research*, 51(2):119–128, 2005.

[49] U. Kim, T. Bal, and D. McCormick. Spindle waves are propagating synchronized oscillations in the ferret LGNd *in vitro*. *Journal of Neurophysiology*, 74(3):1301–1323, 1995.

[50] A. Knox, T. Glauser, J. Tenney, W. Lytton, and K. Holland. Modeling pathogenesis and treatment response in childhood absence epilepsy. *Epilepsia*, 59(1):135–145, 2018.

[51] M. Kohn, M. Hines, J. Kootsey, and M. Freezor. A block organized model builder. *Mathematical and Computer Modelling*, 19(6-8):75–97, 1989.

[52] C. Landisman, M. Long, M. Beierlein, M. Deans, D. Paul, and B. Connors. Electrical synapses in the thalamic reticular nucleus. *Journal of Neuroscience*, 22(3):1002–1009, 2002.

[53] B. Lannes, G. Micheletti, M. Vergnes, C. Marescaux, A. Depaulis, and J.M. Warter. Relationship between spike-wave discharges and vigilance levels in rats with spontaneous petit mal-like epilepsy. *Neuroscience Letters*, 94:187–191, 1988.

[54] S. Lee, S. Patrick, K. Richardson, and B. Connors. Two functionally distinct networks of gap junction-coupled inhibitory neurons in the thalamic reticular nucleus. *Journal of Neuroscience*, 34(39):13170–13182, 2014.

[55] J. Liang, Y. Zhang, J. Wang, H. Pan, H. Wu, K. Xu, et al. New variants in the *CACNA1H* gene identified in childhood absence epilepsy. *Neuroscience Letters*, 406(1–2):27–32, 2006.

[56] J. Liang, Y. Zhang, J. Wang, H. Pan, H. Wu, K. Xu, et al. Common polymorphisms in the *CACNA1H* gene associated with childhood absence epilepsy in Chinese Han population. *Annals of Human Genetics*, 71(3):325–335, 2007.

[57] H. Lodish, A. Berk, S.L. Zipursky, P. Matsudaira, D. Baltimore, and J. Darnell. *Molecular Cell Biology. 4th Edition.* W. H. Freeman, New York, 2000.

[58] S. Maljevic, K. Krampfl, J. Cobilanschi, N. Tilgen, S. Beyer, Y. Weber, et al. A mutation in the $GABA_A$ receptor α_1-subunit is associated with absence epilepsy. *Annals of Neurology*, 59(6):983–987, 2006.

[59] D. McCormick and J. Huguenard. A model of the electrophysiological properties of thalamocortical relay neurons. *Journal of Neurophysiology*, 68(4):1384–1400, 1992.

[60] D. McCormick and H. Pape. Properties of a hyperpolarization-activated cation current and its role in rhythmic oscillation in thalamic relay neurones. *Journal of Physiology*, 431:291–318, 1990.

[61] H. Meeren, J. Pijn, E. Van Luijtelaar, A. Coenen, and F. Lopes da Silva. Cortical focus drives widespread corticothalamic networks during spontaneous absence seizures in rats. *Journal of Neuroscience*, 22(4):1480–1495, 2002.

[62] R. Morison and D. Bassett. Electrical activity of the thalamus and basal ganglia in decorticate cats. *Journal of Neurophysiology*, 8(5):309–314, 1945.

[63] C. Mulle, A. Madariaga, and M. Deschênes. Morphology and electrophysiological properties of reticularis thalami neurons in cat: *in vivo* study of a thalamic pacemaker. *The Journal of Neuroscience*, 6(8):2134–2145, 1986.

[64] T. Narahashi, J. Moore, and W.R. Scott. Tetrodotoxin blockage of sodium conductance increase in lobster giant axons. *Journal of General Physiology*, 47(5):965–974, 1964.

[65] T. Otis, Y. De Koninck, and I. Mody. Characterization of synaptically elicited $GABA_B$ responses using patch-clamp recordings in rat hippocampal slices. *Journal of Physiology*, 463:391–407, 1993.

[66] T. Otis and I. Mody. Modulation of decay kinetics and frequency of $GABA_A$ receptor-mediated spontaneous inhibitory postsynaptic currents in hippocampal neurons. *Neuroscience*, 49(1):13–32, 1992.

[67] P. Pearce, D. Friedman, J. Lafrancois, S. Iyengar, A. Fenton, et al. Spike-wave discharges in adult Sprague-Dawley rats and their implications for animal models of temporal lobe epilepsy. *Epilepsy Behavior*, 32:121–131, 2014.

[68] P. Polack, I. Guillemain, E. Hu, C. Deransart, A. Depaulis, and S. Charpier. Deep layer somatosensory cortical neurons initiate spike-and-wave discharges in a genetic model of absence seizures. *Journal of Neuroscience*, 27(24):6590–6599, 2007.

[69] P. Polack, S. Mahon, M. Chavez, and S. Charpier. Inactivation of the somatosensory cortex prevents paroxysmal oscillations in cortical and related thalamic neurons in a genetic model of absence epilepsy. *Cerebral Cortex*, 19(9):2078–2091, 2009.

[70] K. Powell, S. Cain, C. Ng, S. Sirdesai, L. David, M. Kyi, et al. A $Ca_v3.2$ T-type calcium channel point mutation has splice-variant-specific effects on function and segregates with seizure expression in a polygenic rat model of absence epilepsy. *The Journal of Neuroscience*, 29(2):371–380, 2009.

[71] M. Prevett, J. Duncan, T. Jones, D. Fish, and D. Brooks. Demonstration of thalamic activation during typical absence seizures using $H_2{}^{15}O$ and PET. *Neurology*, 45(7):1396–1402, 1995.

[72] D. Purves, G. Augustine, D. Fitzpatrick, L. Katz, A. LaMantia, et al. *Neuroscience 2^{nd} Edition*. Sinauer Associates, Sunderland, MA, 2001.

[73] C. Schwiening. A brief historical perspective: Hodgkin and Huxley. *Journal of Physiology*, 590(11):2571–2575, 2012.

[74] B. Sinclair and H. Unwala. Absence epilepsy in childhood: Electroencephalography (EEG) does not predict outcome. *Journal of Child Neurology*, 22(7):799–802, 2007.

[75] J. Sobotta. An anatomical illustration from Sobotta's Human Anatomy, 1908. In *Atlas and Text-book of Human Anatomy Volume III Vascular System, Lymphatic system, Nervous system and Sense Organs*. W. B. Saunders company, Philadelphia, 1914.

[76] I. Soltesz, S. Lightowler, N. Leresche, D. Jassik-Gerschenfeld, C. Pollard, and V. Crunelli. Two inward currents and the transformation of low-frequency oscillations of rat and cat thalamocortical cells. *The Journal of Physiology*, 441:175–197, 1991.

[77] L. Squire, D. Berg, F. Bloom, S. du Lac, A. Ghosh, and N. Spitzer. *Fundamental Neuroscience Fourth Edition*. Academic Press, Waltham, MA, 2012.

[78] M. Steriade, L. Domich, G. Oakson, and M. Deschênes. The deafferented reticular thalamic nucleus generates spindle rhythmicity. *Journal of Neurophysiology*, 57(1):260–273, 1987.

[79] M. Steriade, D. McCormick, and T.J. Sejnowski. Thalamocortical oscillations in the sleeping and aroused brain. *Science*, 262(5134):679–685, 1993.

[80] P. Striano and V. Belcastro. Treatment of myoclonic seizures. *Expert Review of Neurotherapeutics*, 12(12):1411–1418, 2012.

[81] E. Talley, G. Solórzano, A. Depaulis, E. Perez-Reyes, and D. Bayliss. Low-voltage-activated calcium channel subunit expression in a genetic model of absence epilepsy in the rat. *Molecular Brain Research*, 75(1):159–165, 2000.

[82] R. Traub and R. Miles. *Neuronal Networks of the Hippocampus.* Cambridge Univ. Press., Cambridge, UK, 1991.

[83] R. Traub, R. Wong, R. Miles, and H. Michelson. A model of CA3 hippocampal pyramidal neuron incorporating voltage-clamp data on intrinsic conductances. *Journal of Neurophysiology*, 66(2):635–650, 1991.

[84] E. Tsakiridou, L. Bertolllini, M. de Curtis, G. Avanzini, and H. Pape. Selective increase in T-type calcium conductance of reticular thalamic neurons in a rat model of absence epilepsy. *The Journal of Neuroscience*, 15(4):3110–3117, 1995.

[85] I. Vitko, Y. Chen, J.M. Arias, Y. Shen, X.R. Wu, and E. Perez-Reyes. Functional characterization and neuronal modeling of the effects of childhood absence epilepsy variants of *CACNA1H*, a T-type calcium channel. *The Journal of Neuroscience*, 25(19):4844–4855, 2005. ModelDB Accession Number: 53965.

[86] R. Wallace, C. Marini, S. Petrou, L. Harkin, D. Bowser, R. Panchal, and et. al. Mutant $GABA_A$ receptor γ2-subunit in childhood absence epilepsy and febrile seizures. *Nature Genetics*, 28(1):49–52, 2001.

[87] M. Williams, T. Altwegg-Boussac, M. Chavez, S. Lecas, S. Mahon, and S. Charpier. Integrative properties and transfer function of cortical neurons initiating absence seizures in a rat genetic model. *The Journal of Physiology*, 594(22):6733–6751, 2016.

[88] W. Woldman and J. Terry. Multilevel computational modelling in epilepsy: Classical studies and recent advances. In B. Bhattacharya and F. Chowdhury, editors, *Validating Neuro-Computational Models of Neurological and Psychiatric Disorders*, pages 161–188. Springer International Publishing, Switzerland, 2015.

[89] Z. Xiang, A. Greenwood, and T. Brown. Measurement and analysis of hippocampal mossy-fiber synapses. *Soc. Neurosci. Abstr.*, 18:1350, 1992.

[90] H. Xie, Y. Zhang, P. Zhang, J. Wang, Y. Wu, X. Wu, et al. Functional study of *NIPA2* mutations identified from the patients with childhood absence epilepsy. *PLOS ONE*, 9(10):e109749, 2014.

[91] T. Zolnik and B. Connors. Electrical synapses and the development of inhibitory circuits in the thalamus. *The Journal of Physiology*, 594(10):2579–2592, 2016.

APPENDICES

Appendix A

RE Model for XPPAUT

```
#Initialize
init v=-74
init Cai = 0.00024

dV/dt = (1/cm)*(-Ina -Ik -Il - It - Ikca - Ican + Iapp + i*H)

#Parameters
par cm=1
par gbarna=100, gbark=10, Ena=50
par gl=0.05, El=-78
par gbarca=1.75, Eca=120
par gbarkca=10, Ek=-95, n=2, a=48, b=0.03
par gbarcan=0.25, Ecan=-20, nn=2, aa=20, bb=0.002
par d=1
par KT=0.0001, KD=0.0001
par cainf=0.00024, taur=100, k=10
#eqn for ta1 = 3^((36-22)/10)=4.6555367
par ta1=4.6555367
par j=-55

number F=96485.332

#Intracellular Calcium Dynamics
```

```
dCai/dt=(-k*It)/(2*F*d)+(-KT*Cai)/(Cai+KD)+(cainf-Cai)/taur

#Fast Na+ and K+ currents: Ina and Ik
Ina=gbarna*(mn^3)*(hn)*(V-Ena)
Ik=gbark*(nk^4)*(V-Ek)

am(V)=0.32*(13-(V-j))/(exp((13-(V-j))/4)-1)
bm(V)=0.28*((V-j)-40)/(exp(((V-j)-40)/5)-1)
ah(V)=0.128*(exp((17-(V-j))/18))
bh(V)=4/(exp((40-(V-j))/5)+1)
an(V)=0.032*(15-(V-j))/(exp((15-(V-j))/5)-1)
bn(V)=0.5*exp((10-(V-j))/40)

mninf(V)=am(V)/(am(V)+bm(V))
taomn(V)=1/(am(V)+bm(V))
hninf(V)=ah(V)/(ah(v)+bh(v))
taohn(V)=1/(ah(V)+bh(V))
nkinf(V)=an(V)/(an(V)+bn(V))
taonk(V)=1/(an(V)+bn(V))

dmn/dt=((am(V)*(1-mn))-(bm(V)*mn))
dnk/dt=((an(V)*(1-nk))-(bn(V)*nk))
dhn/dt=((ah(V)*(1-hn))-(bh(V)*hn))

#Leak current: Il
Il=gl*(V-El)

#Low-threshold Ca2+ current: It
It=gbarca*(mt^2)*(ht)*(V-Eca)
dmt/dt=(-1/taomt(V))*(mt-mtinf(V))
dht/dt=(-1/taoht(V))*(ht-htinf(V))

mtinf(V)=1/(1+exp(-(V+52)/7.4))
taomt(V)=0.44+(0.15/(exp((V+27)/10)+exp(-(V+102)/15)))

htinf(V)= 1/(1+exp((V+80)/5))
taoht(V)=22.7+(gg/(exp((V+48)/4)+exp(-(V+407)/50)))
par gg=0.27
```

```
#Ca-dependent K current: Ikca
Ikca=gbarkca*(mm^2)*(V-Ek)
dmm/dt=(-1/taomm(Cai))*(mm-mminf(Cai))*ta1

mminf(Cai)=(a*(Cai^n))/((a*(Cai^n))+b)
taomm(Cai)=1/((a*(Cai^n))+b)

#Ca-dependent nonspecific cation current: Ican
Ican=gbarcan*(mc^2)*(V-Ecan)
dmc/dt=(-1/taomc(Cai))*(mc-mcinf(Cai))*ta1

mcinf(Cai)=(aa*(Cai^nn))/((aa*(Cai^nn))+bb)
taomc(Cai)=1/((aa*(Cai^nn))+bb)

#Use heav() to create specific length pulse
H=(heav(t-50)-heav(t-150))
par i=0, Iapp=0

#Create aux equations to track currents
aux IIna=Ina
aux IIk=Ik
aux IIl=Il
aux IIt=It
aux IIkca=Ikca
aux IIcan=Ican

@ total=4000, bound=1000000, dt=01, xhi=4000, yhi=60, ylo=-120,
maxstor=2000000
done
```

Appendix B

TC Model for XPPAUT

```
#Initialize
init v=-68
init cai=0.00024

dV/dt=(1/cm)*(-oL*Il-ot*It-oh*Ih-okl*Ikl-ona*Ina-ok*Ik+Iapp+i*H)

#Parameters
par ol=1, ot=1, oh=1, okl=1, ona=1, ok=1
par cm=1
par d=1, taur=5, cainf=0.00024
par gl=0.01, El=-70
par gt=2, caot=2, cait=0.00024
par gh=0.01, Eh=-40
par cac=0.002, k2=0.0004, Pc=0.01, k4=0.001
par nca=4, nexp=1, ginc=2, taum=20
par gkl=0.013793, Ekl=-100
par vtraub=-25
par gna=90, Ena=50
par gk=10, Ek=-100
par i=0, Iapp=0
# equation for ta1=3^((36-24)/10)
par ta1=3.73719
```

```
number R=8.31451, F=96485.332, Temp=309.15

#Intracellular calcium dynamics
dcai/dt=(-10*It/(2*F*d))+((cainf-cai)/taur)

#Leak current: Il
Il=gl*(V-El)

#Low-threshold Ca2+ current: It
It=gt*(mtinf(V)^2)*ht*(V-Eca)
dht/dt=(ta1)*(htinf(V)-ht)/taoht(V)
Eca=(1000)*(R*Temp)/(2*F)*(log(caot/cait))

mtinf(V)=1/(1+exp(-((V+2)+57)/6.2))
htinf(V)=1/(1+exp((V+2)+81)/4)
taoht(V)=30.8+((211.4+exp(((V+2)+113.2)/5))/(1+exp(((V+2)+84)/3.2)))

#Hyperpolarization-activated cation current: Ih
Ih=gh*mh*(V-Eh)
dmh/dt=(mhinf(V)-mh)/taomh(V)

mhinf(V)=(1/(1+exp((V+75)/5.5)))
taomh(V)=1/(exp(-14.59-(0.086*V))+exp(-1.87+(0.0701*V)))

#Leak potassium current: Ikl
Ikl=gkl*(V-Ekl)

#Fast Na+ current: Ina
Ina=gna*(mn^3)*hn*(V-Ena)
dmn/dt=(mninf(V)-mn)/taomn(V)
dhn/dt=(hninf(V)-hn)/taohn(V)

mninf(V)=amn(V)/(amn(V)+bmn(V))
taomn(V)=1/(amn(V)+bmn(V))
hninf(V)=ahn(V)/(ahn(V)+bhn(V))
taohn(V)=1/(ahn(V)+bhn(V))

amn(V)=(0.32*(13-(V-vtraub)))/(exp((13-(V-vtraub))/4)-1)
```

```
bmn(V)=(0.28*((V-vtraub)-40))/(exp(((V-vtraub)-40)/5)-1)
ahn(V)=0.128*exp((17-(V-vtraub))/18)
bhn(V)=4/(exp((40-(V-vtraub))/5)+1)

#Fast K+ current: Ik
Ik=gk*(nk^4)*(V-Ek)
dnk/dt=(nkinf(V)-nk)/taonk(V)

nkinf(V)=ank(V)/(ank(V)+bnk(V))
taonk(V)=1/(ank(V)+bnk(V))

ank(V)=(0.032*(15-(V-vtraub)))/(exp((15-(V-vtraub))/5)-1)
bnk(V)=0.5*exp((10-(V-vtraub))/40)

#Use heav() to create specific length pulse
H=(heav(t-50)-heav(t-150))

#Create aux equations to track currents
aux IIl=Il
aux IIt=It
aux IIh=Ih
aux IIkl=Ikl
aux IIna=Ina
aux IIk=Ik

@ total=500,bound=1000000,dt=.01,xhi=750,yhi=60,ylo=-120
,maxstor=2000000
done
```

Appendix C

RE 5-Cell Network Model for XPPAUT

C.1 RE 5-Cell Network, Connections to All Other Cells *Without* Self-Connections

```
#Notes:
# 'special k=mmult(n,m,w,u)' will return a vector 'k' of length m, defined
as the sum of the products from 0 to n-1, of w(i+nj)*u(i). w is the table
file included below, r is a variable created in the file (in this case,
the synapse/gap variable).
# matrix/table file is an adjacency matrix representing which cells are
connected to which. use this file to change the connections in the
network.
# need to have the matrix/table file included in the same folder as this
file.

#Don't recompute the random tables every time a parameter is changed
@ autoeval=0

#Read in Matrix/Table file
table w wall-E5.tab
```

```
#Multiply synapses by weights (for gaba)
special syngab=mmult(5,5,w,r0)

#for gap
special syngap=mmult(5,5,w,V0)

#Initialize
init v[0..4]=-74
init Cai[0..4]=0.00024

#RE cells membrane potential equations
v[0..4]'=(1/cm)*(-Ina[j] -Ik[j] -Il[j] - It[j] - Ikca[j] - Ican[j] +
Iapp[j] + i[j]*H[j] - Igaba[j] - Igap[j])

#Parameters
par cm = 1
par gbarna = 100, gbark = 10, Ena = 50
par gl = 0.05, El = -78
par gbarca = 1.75
par gbarkca = 10, Ek = -95, n = 2, a = 48, b = 0.03
par gbarcan = 0.25, Ecan = -20, nn = 2, aa = 20, bb = 0.002
par F = 96489, d = 1
par KT = 0.0001, KD = 0.0001
par k = 10
par jj = -55
par cainf = 0.00024, taur = 100
par Eca = 120
#eqn for ta1 = 3^((36-22)/10)=4.6555367
par ta1=4.6555367
par Iapp[0..4]=0

#Intracellular calcium dynamics
dCai[0..4]/dt = (-k*It[j])/(2*F*d)
+ (-KT*Cai[j])/(Cai[j]+KD) + (cainf-Cai[j])/taur

#Fast Na+ and K+ currents: Ina and Ik
Ina[0..4] = gbarna*(mn[j]^3)*(hn[j])*(V[j]-Ena)
Ik[0..4] = gbark*(nk[j]^4)*(V[j]-Ek)
```

```
am(V) = 0.32*(13-(V-jj))/(exp((13-(V-jj))/4)-1)
bm(V) = 0.28*((V-jj)-40)/(exp(((V-jj)-40)/5)-1)
ah(V) = 0.128*(exp((17-(V-jj))/18))
bh(V) = 4/(exp((40-(V-jj))/5)+1)
an(V) = 0.032*(15-(V-jj))/(exp((15-(V-jj))/5)-1)
bn(V) = 0.5*exp((10-(V-jj))/40)

dmn[0..4]/dt = ((am(V[j])*(1-mn[j])) - (bm(V[j])*mn[j]))
dnk[0..4]/dt = ((an(V[j])*(1-nk[j])) - (bn(V[j])*nk[j]))
dhn[0..4]/dt = ((ah(V[j])*(1-hn[j])) - (bh(V[j])*hn[j]))

#Leak current: Il
Il[0..4] = gl*(V[j]-El)

#Low-threshold Ca current: It
It[0..4] = gbarca*(mt[j]^2)*(ht[j])*(V[j]-Eca)
dmt[0..4]/dt = (-1/taomt(V[j]))*(mt[j] - mtinf(V[j]))
dht[0..4]/dt = (-1/taoht(V[j]))*(ht[j] - htinf(V[j]))

mtinf(V) = 1/(1+exp(-(V+52)/7.4))
taomt(V) = 0.44 + (0.15/(exp((V+27)/10) + exp(-(V+102)/15)))

htinf(V) = 1/(1+exp((V+80)/5))
taoht(V) = 22.7 + (0.27/(exp((V+48)/4) + exp(-(V+407)/50)))

#Ca-dependent K current: Ikca
Ikca[0..4] = gbarkca*(mm[j]^2)*(V[j]-Ek)
dmm[0..4]/dt = (-1/taomm(Cai[j]))*(mm[j] - mminf(Cai[j]))*ta1

mminf(Cai) = (a*(Cai^n))/((a*(Cai^n))+b)
taomm(Cai) = 1/((a*(Cai^n))+b)

#Ca-dependent nonspecific cation current: Ican
Ican[0..4]=gbarcan*(mc[j]^2)*(V[j]-Ecan)
dmc[0..4]/dt=(-1/taomc(Cai[j]))*(mc[j] - mcinf(Cai[j]))*ta1

mcinf(Cai) = (aa*(Cai^nn))/((aa*(Cai^nn))+bb)
```

```
taomc(Cai) = 1/((aa*(Cai^nn))+bb)

#Use heav() to create specific length pulse
H0=(heav(t-h0s)-heav(t-h0f))
H1=(heav(t-h1s)-heav(t-h1f))
H2=(heav(t-h2s)-heav(t-h2f))
H3=(heav(t-h3s)-heav(t-h3f))
H4=(heav(t-h4s)-heav(t-h4f))

par i[0..4] = 0
par h0s=50, h0f=150
par h1s=50, h1f=150
par h2s=50, h2f=150
par h3s=50, h3f=150
par h4s=50, h4f=150

###Gaba
#use r in the special/mmult function
Igaba[0..4] = (syngab([j]))*gbargaba*(V[j]-Egaba)
dr[0..4]/dt = (alpha*((Cmax)/(1+exp(-(V[j]-VT)/Kp)))*(1-r[j]))
- (beta*r[j])

par Egaba = -80, gbargaba = 1, alpha = 0.53, beta = 0.184
par Cmax = 1, VT = 2, Kp = 5

#Gap
Igap[0..4]=4*gbargap*V[j]-gbargap*syngap([j])

par gbargap = 0.0005

###create aux equations to track currents
aux IIna[0..4] = Ina[j]
aux IIk[0..4] = Ik[j]
aux IIl[0..4] = Il[j]
aux IIt[0..4] = It[j]
aux IIkca[0..4] = Ikca[j]
aux IIcan[0..4] = Ican[j]
aux IIgaba0 = Igaba0
```

```
aux IIgap1 = Igap1

@ total=4000,bound=100000,dt=.01,xhi=4000,yhi=60,ylo=-120,
maxstor=200000
done
```

C.2 Corresponding Table File for Synaptic Conductances

```
#Note: To include self-connections, change all matrix/table elements to
"1". This file is run with a ".tab" extension.

#Adjacency Matrix/Table
24
 0
24
 0
 1
 1
 1
 1
 1
 0
 1
 1
 1
 1
 1
 0
 1
 1
 1
 1
 1
 0
 1
```

1
1
1
1
0

Appendix D

RE-TC Network Model for XPPAUT

```
###TC CELL###

#Initialize
init Vt0=-68
init Vt1=-68
init cait[0..1]=0.00024

dVt0/dt=(1/cm)*(-Ilt0-Itt0-Iht0-Iklt0-Inat0-Ikt0
-Igabat00-Igabat01-Igabab00-Igabab01+Iappt0+it0*Ht0)

dVt1/dt=(1/cm)*(-Ilt1-Itt1-Iht1-Iklt1-Inat1-Ikt1
-Igabat10-Igabat11-Igabab10-Igabab11+Iappt1+it1*Ht1)

#TC Parameters
par cm=1
par d=1, taurt=5, cainft=0.00024
par glt=0.01, Elt=-70
par gtt=2, caott=2, caitt=0.00024
par ght0=0.01, ght1=0.01, Eht=-40
par cac=0.002, k2=0.0004, Pc=0.01, k4=0.001
par nca=4, nexp=1, ginc=2, taum=20
par gklt0=0.013793, gklt1=0.013793, Eklt=-100
par vtraub=-25
```

```
par gnat=90, Enat=50
par gkt=10, Ekt=-100
par it[0..1]=0
par Iappt[0..1]=0
#formula for ta1t ta1t=3^((36-24)/10)
par ta1t=3.73719

number R=8.31451, F=96485.332, Temp=309.15

#Intracellular calcium dynamics
dcait[0..1]/dt=(-10*Itt[j]/(2*F*d))+((cainft-cait[j])/taurt)

#Leak current: Il
Ilt[0..1]=glt*(Vt[j]-Elt)

#Low-threshold Ca2+ current: It
Itt[0..1]=gtt*(mtinft(Vt[j])^2)*htt[j]*(Vt[j]-Ecat)
dhtt[0..1]/dt=(ta1t)*(htinft(Vt[j])-htt[j])/taohtt(Vt[j])
Ecat=(1000)*(R*Temp)/(2*F)*(log(caott/caitt))

mtinft(V)=1/(1+exp(-((V+2)+57)/6.2))
htinft(V)=1/(1+exp((V+2)+81)/4)
taohtt(V)=30.8+((211.4+exp(((V+2)+113.2)/5))/(1+exp(((V+2)+84)/3.2)))

#Hyperpolarization-activated cation current: Ih
Iht[0..1]=ght[j]*mht[j]*(Vt[j]-Eht)

dmht[0..1]/dt=(mhinf(Vt[j])-mht[j])/taomh(Vt[j])
mhinf(V)=(1/(1+exp((V+75)/5.5)))
taomh(V)=1/(exp(-14.59-(0.086*V))+exp(-1.87+(0.0701*V)))

#Leak potassium current: Ikl
Iklt[0..1]=gklt[j]*(Vt[j]-Eklt)

#Fast Na+ current: Na
Inat[0..1]=gnat*(mnt[j]^3)*hnt[j]*(Vt[j]-Enat)
dmnt[0..1]/dt=(mninft(Vt[j])-mnt[j])/taomnt(Vt[j])
dhnt[0..1]/dt=(hninft(Vt[j])-hnt[j])/taohnt(Vt[j])
```

```
mninft(Vt)=amnt(Vt)/(amnt(Vt)+bmnt(Vt))
taomnt(Vt)=1/(amnt(Vt)+bmnt(Vt))
hninft(Vt)=ahnt(Vt)/(ahnt(Vt)+bhnt(Vt))
taohnt(Vt)=1/(ahnt(Vt)+bhnt(Vt))

amnt(Vt)=(0.32*(13-(Vt-vtraub)))/(exp((13-(Vt-vtraub))/4)-1)
bmnt(Vt)=(0.28*((Vt-vtraub)-40))/(exp(((Vt-vtraub)-40)/5)-1)
ahnt(Vt)=0.128*exp((17-(Vt-vtraub))/18)
bhnt(Vt)=4/(exp((40-(Vt-vtraub))/5)+1)

#Fast K+ current: Ik
Ikt[0..1]=gkt*(nkt[j]^4)*(Vt[j]-Ekt)
dnkt[0..1]/dt=(nkinft(Vt[j])-nkt[j])/taonkt(Vt[j])

nkinft(Vt)=ankt(Vt)/(ankt(Vt)+bnkt(Vt))
taonkt(Vt)=1/(ankt(Vt)+bnkt(Vt))

ankt(Vt)=(0.032*(15-(Vt-vtraub)))/(exp((15-(Vt-vtraub))/5)-1)
bnkt(Vt)=0.5*exp((10-(Vt-vtraub))/40)

#Use heav() to create specific length pulse
Ht0=(heav(t-ht0s)-heav(t-ht0f))
Ht1=(heav(t-ht1s)-heav(t-ht1f))

par ht0s=50, ht0f=150
par ht1s=50, ht1f=150

# Create aux equations to track currents
aux IIlt[0..1]=Ilt[j]
aux IItt[0..1]=Itt[j]
aux IIht[0..1]=Iht[j]
aux IIklt[0..1]=Iklt[j]
aux IInat[0..1]=Inat[j]
aux IIkt[0..1]=Ikt[j]


###RE CELL###
```

```
#Initialize
init Vr0=-74
init Vr1=-74
init caiR[0..1]=0.00024

dVr0/dt=(1/cm)*(-Inar0-Ikr0-Ilr0-Itr0+Iappr0+ir0*Hr0-Igabar0
-Iampa00-Iampa01)

dVr1/dt=(1/cm)*(-Inar1-Ikr1-Ilr1-Itr1+Iappr1+ir1*Hr1-Igabar1
-Iampa10-Iampa11)

#RE Parameters
par gnar=100, gkr=10, Enar=50
par glr=0.05, Elr=-78
par gcar=1.75, Ecar=120
par gkcar=10, Ekr=-95
par n=2, a=48, b=0.03
par gcanr=0.25, Ecanr=-20
par nn=2, aa=20, bb=0.002
par KT=0.0001, KD=0.0001
par cainfr=0.00024, taurr=100, k=10
par jj = -55
par ir[0..1]=0
par Iappr[0..1]=0
#eqn for ta1r = 3^((36-22)/10)=4.6555367
par ta1r=4.6555367

#Intracellular calcium dynamics
dCair[0..1]/dt = (-k*Itr[j])/(2*F*d)+(-KT*Cair[j])/(Cair[j]+KD)
+(cainfr-Cair[j])/taurr

#Fast Na+ and K+ currents: Ina and Ik
Inar[0..1]=gnar*(mnr[j]^3)*(hnr[j])*(Vr[j]-Enar)
Ikr[0..1]=gkr*(nkr[j]^4)*(Vr[j]-Ekr)

dmnr[0..1]/dt=(mninfr(Vr[j])-mnr[j])/taomnr(Vr[j])
dhnr[0..1]/dt=(hninfr(Vr[j])-hnr[j])/taohnr(Vr[j])
```

```
dnkr[0..1]/dt=(nkinfr(Vr[j])-nkr[j])/taonkr(Vr[j])

amr(V)=0.32*(13-(V-jj))/(exp((13-(V-jj))/4)-1)
bmr(V)=0.28*((V-jj)-40)/(exp(((V-jj)-40)/5)-1)
ahr(V)=0.128*(exp((17-(V-jj))/18))
bhr(V)=4/(exp((40-(V-jj))/5)+1)
anr(V)=0.032*(15-(V-jj))/(exp((15-(V-jj))/5)-1)
bnr(V)=0.5*exp((10-(V-jj))/40)

mninfr(V) = amr(V)/(amr(V)+bmr(V))
taomnr(V) = 1/(amr(V)+bmr(V))
hninfr(V) = ahr(V)/(ahr(v)+bhr(v))
taohnr(V) = 1/(ahr(V)+bhr(V))
nkinfr(V) = anr(V)/(anr(V)+bnr(V))
taonkr(V) = 1/(anr(V)+bnr(V))

#Leak current: Il
Ilr[0..1]=glr*(Vr[j]-Elr)

#Low-threshold Ca+ current: It
Itr[0..1]=gcar*(mtr[j]^2)*(htr[j])*(Vr[j]-Ecar)
dmtr[0..1]/dt=(-1/taomtr(Vr[j]))*(mtr[j]-mtinfr(Vr[j]))
dhtr[0..1]/dt=(-1/taohtr(Vr[j]))*(htr[j]-htinfr(Vr[j]))

mtinfr(V)=1/(1+exp(-(V+52)/7.4))
taomtr(V)=0.44+(0.15/(exp((V+27)/10)+exp(-(V+102)/15)))

htinfr(V)=1/(1+exp((V+80)/5))
taohtr(V)=22.7+(gg/(exp((V+48)/4)+exp(-(V+407)/50)))
par gg=0.27

##Ca-dependent K current: Ikca
#Ikcar[0..1]=gkcar*(mmr[j]^2)*(Vr[j]-Ekr)
#dmmr[0..1]/dt=(-1/taommr(Cair[j]))*(mmr[j]-mminfr(Cair[j]))*ta1r
#mminfr(Cai)=(a*(Cai^n))/((a*(Cai^n))+b)
#taommr(Cai)=1/((a*(Cai^n))+b)

##Ca-dependent nonspecific cation current: Ican
```

```
#Icanr[0..1]=gcanr*(mcr[j]^2)*(Vr[j]-Ecanr)
#dmcr[0..1]/dt=(-1/taomcr(Cair[j]))*(mcr[j]-mcinfr(Cair[j]))*ta1r
#mcinfr(Cair)=(aa*(Cair^nn))/((aa*(Cair^nn))+bb)
#taomcr(Cair)=1/((aa*(Cair^nn))+bb)

#Use heav() to create specific length pulse
Hr0=(heav(t-hr0s)-heav(t-hr0f))
Hr1=(heav(t-hr1s)-heav(t-hr1f))

par hr0s=50, hr0f=150
par hr1s=50, hr1f=150

#Create aux equations to track currents
aux IInar[0..1]=Inar[j]
aux IIkr[0..1]=Ikr[j]
aux IIlr[0..1]=Ilr[j]
aux IItr[0..1]=Itr[j]
#aux IIkcar[0..1]=Ikcar[j]
#aux IIcanr[0..1]=Icanr[j]
aux IIgabar[0..1]=Igabar[j]
aux IIgabat00=Igabat00
aux IIgabat01=Igabat01
aux IIgabat10=Igabat10
aux IIgabat11=Igabat11


###Synapses###

#Synpatic conversion factors:
par KTC=3.448275
par KRE=6.993006

##RE CELL Synapses##

#AMPA
Iampa00=rt0*KRE*gampa*(Vr0-Eampa)
Iampa01=rt1*KRE*gampa*(Vr0-Eampa)
Iampa10=rt0*KRE*gampa*(Vr1-Eampa)
```

```
Iampa11=rt1*KRE*gampa*(Vr1-Eampa)

drt0/dt=(alphar*((Cmax)/(1+exp(-(Vt0-VTry)/Kp)))*(1-rt0))-(betar*rt0)
drt1/dt=(alphar*((Cmax)/(1+exp(-(Vt1-VTry)/Kp)))*(1-rt1))-(betar*rt1)

par Eampa=0, gampa=0.2, alphar=0.94, betar=0.18

#GABAr
Igabar0=rr1*KRE*ggabar*(Vr0-Egaba)
Igabar1=rr0*KRE*ggabar*(Vr1-Egaba)

drr0/dt=(alphat*((Cmax)/(1+exp(-(Vr0-VTry)/Kp)))*(1-rr0))-(betat*rr0)
drr1/dt=(alphat*((Cmax)/(1+exp(-(Vr1-VTry)/Kp)))*(1-rr1))-(betat*rr1)

par Egaba=-80, ggabar=0.2, alphat=10.5, betat=0.166
par Cmax=0.5, Vtry=2, Kp=5

##TC CELL Synapses##

#GabaB
Igabab00=ggabab*KTC*((g0^4)/((g0^4)+Kdd))*(Vt0-Egb)
Igabab01=ggabab*KTC*((g1^4)/((g1^4)+Kdd))*(Vt0-Egb)
Igabab10=ggabab*KTC*((g0^4)/((g0^4)+Kdd))*(Vt1-Egb)
Igabab11=ggabab*KTC*((g1^4)/((g1^4)+Kdd))*(Vt1-Egb)

dg0/dt=(K33*rb0)-(K44*g0)
drb0/dt=(K11*((Cmax)/(1+exp(-(Vr0-Vtry)/Kp)))*(1-rb0))-(K22*rb0)
dg1/dt=(K33*rb1)-(K44*g1)
drb1/dt=(K11*((Cmax)/(1+exp(-(Vr1-Vtry)/Kp)))*(1-rb1))-(K22*rb1)

par Egb=-95, ggabab=0.04
par K11=0.5, K22=0.0012, K33=0.18, K44=0.034, Kdd=100

#GabaA
Igabat00=ra1*ggabat*KTC*(Vt0-Egaba)
Igabat01=ra0*ggabat*KTC*(Vt0-Egaba)
Igabat10=ra1*ggabat*KTC*(Vt1-Egaba)
Igabat11=ra0*ggabat*KTC*(Vt1-Egaba)
```

```
dra0/dt=(alphat*((Cmax)/(1+exp(-(Vr0-VTry)/Kp)))*(1-ra0))-(betat*ra0)
dra1/dt=(alphat*((Cmax)/(1+exp(-(Vr1-VTry)/Kp)))*(1-ra1))-(betat*ra1)

par ggabat=0.02

@ total=4000,bound=1000000,dt=.01,xhi=4000,yhi=60,ylo=-120,
maxstor=2000000
done
```